universität wien

DISSERTATION / DOCTORAL THESIS

Titel der Dissertation /Title of the Doctoral Thesis

„Experiments with a pulsed Talbot Lau matter-wave interferometer“

verfasst von / submitted by

Jonas Rodewald, BSc MSc

angestrebter akademischer Grad / in partial fulfilment of the requirements for the degree of

Doktor der Naturwissenschaften (Dr. rer. nat.)

Wien, 2017 / Vienna, 2017

Studienkennzahl lt. Studienblatt / degree programme code as it appears on the student record sheet:	A 796 605 411
Dissertationsgebiet lt. Studienblatt / field of study as it appears on the student record sheet:	Physik
Betreut von / Supervisor:	Univ. Prof. Dr. Markus Arndt

Contents

Abstract

According to the quantum superposition principle, massive particles can be delocalized and propagate though space as waves of matter. To date it is not known whether this principle holds for particles of all masses or if there exists a mass limit to its validity. Matter-wave interferometry is a direct test of such delocalization of particles. In this thesis I present the optical time-domain matter-wave (OTIMA) interferometer, an experiment that was specifically designed to probe and exploit superposition states of large particles [1, 2]. The setup is of the Talbot Lau-type and utilizes three pulsed standing wave laser gratings. Such optical structures imprint a periodic pattern onto the traversing matter waves through photo depletion of the particle density at the standing wave antinodes. The particle's optical polarizability and the efficiency of photoionization or dissociation of the particles at the grating wavelength λ determine how strongly the standing waves act as phase gratings and absorptive masks with a grating period of $d = \lambda/2$. All three standing waves are generated for only a few nanoseconds by retro-reflecting 157 nm laser pulses at a single mirror surface, leading to a grating period of less than 80nm [3, 4]. The time-domain interferometer scheme offers high visibility and measurement precision while the common boundary condition for the standing waves provides robustness towards vibrational dephasing [1]. Since the optical gratings interact non-dispersively with the interfering particles, the setup enables interference experiments with large and heavy particles in a quest for novel decoherence effects or objective collapse mechanism [1, 2]. I present experimental progress in characterizing the interferometer in conjunction with various different particle beam sources and discuss systematic effects on the interference contrast [5]. Proof of principle results of interference experiments with tailor-made nanoparticles are presented and discussed in the context of high-mass matter-wave interferometry. On the applied side, the ability to resolve particle deflection by a small fraction of the grating period facilitates measurements of the interaction between interfering particles and external probe fields, such as running or standing light fields [6]. Various different schemes for spectroscopy in the OTIMA interferometer are discussed.

Zusammenfassung

Das quantenmechanische Superpositionsprinzip postuliert, daß massive Teilchen delokalisiert sein können und sich als Materiewellen im Raum ausbreiten. Dieses Verhalten konnte bisher z.B. Photonen, Neutronen, Atomen und vielen Molekülen nachgewiesen werden, und dennoch ist es bis heute ungeklärt, ob Teilchen beliebiger Masse in solche Überlagerungszustände gebracht werden können. In dieser Arbeit stelle ich ein gepulstes Lichtgitter Materiewellen (OTIMA) Interferometer vor, welches wir gebaut haben, um nach einer Massenabhängigkeit dieser Phänomene zu suchen [1, 2]. Das Experiment basiert auf dem Talbot Lau Effekt und besteht im Kern aus drei stehende Lichtwellen, die durch Retroreflektion von Lichtpulsen an einer einzelnen Spiegeloberfläche entstehen. Die Teilchen, die durch die Bäuche der Stehwellen fliegen, werden durch Photoionisation oder Photofragmentation aus dem Teilchenstrahl entfernt [3, 4]. So entsteht ein räumliches Muster in der Teilchendichte. Wie stark dabei diese Lichtpulse als absorptive Gitter und Phasengitter wirken ist durch die Photoionisations- und Photofragmentationseffizienz bzw. die optische Polarisierbarkeit der Teilchen im Gitter bestimmt. Im OTIMA Interferometer kommen zu diesem Zweck 157 nm Laser zum Einsatz, so daß die Stehwellengitter Perioden von unter 80 nm haben. Optische Gitter haben zudem den Vorteil eines variablen Öffnungsverhältnisses, welches durch die Laserpower in den Stehwellen gegeben ist: je kleiner das Öffnungsverhältnis, desto größer sind Interferenzkontrast und Messprezision. Dabei macht die Verwendung einer gemeinsamen Randbedingung für alle drei Stehwellen die Messungen robuster gegen Dephasierung durch mechanische Vibrationen der Apparatur. Durch die nicht-dispersive Wechselwirkung zwischen den Gittern und den interferierenden Teilchen wird das Experiment in Zukunft Interferenzmessungen mit immer größerern Teilchen erlauben und könnte damit die Suche nach neuartigen Dekohärenzeffekten oder objektiven Kollapsmechanismen ermöglichen [1, 2]. Im Rahmen dieser Arbeit bespreche ich die Fortschritte in der Charakterisierung des Interferometers und diskutiere systematische Effekte, welche den Interferenzkontrast beeinflussen [5]. Außerdem zeige ich Ergebnisse einer Machbarkeitsstudie, welche die Eignung maßgeschneiderter Nanoteilchen für Tests des Welle-Teilchen-Dualismus in unserem Experiment untersucht.
Das OTIMA Interferometer ist der quantenphysikalischen Grundlagenforschung gewidmet, ermöglicht aber auch spektroskopische Messungen von Teilcheneigenschaften [6]. Im letzten Teil dieser Arbeit stelle ich ein paar solch angewandter OTIMA Experimente vor.

Chapter 1

Introduction

The formulation and experimental verification of quantum theory is undeniably a story of success: until today the theory has passed every experimental test. From the laying of its ground stones at the beginning of the past century [7–10] and the skeptical founders calling the consequences of their own results *spooky* [11] or *burlesque* [12], quantum physics has come a long way. Not only are the laws of quantum mechanics nowadays applied to solve problems in just about every discipline of physics, they have also fueled incredible technological progress and enabled the development of transistors, lasers, atomic clocks, and superconductors, to name only a few. But many are still suspicious. Why is that? A possible explanation is the following: while a successful theory for microscopic realm, there is no general consent about how to stitch quantum mechanics to two other heavyweights of physics, namely the theory of general relativity and classical mechanics. General relativity, recently reinforced by the first detection of gravitational waves [13], and its notion of continuous space time, seems incompatible with the discrete nature of standard quantum mechanics, or vice versa. Also, classical mechanics, which is so familiar to us since it apparently governs everything we perceive with our bare eyes, seems fundamentally un-quantum to us. While our perception may very well be unsuited to recognize how quantum mechanics rules the dynamics of our everyday objects, one inevitably runs into paradoxical situations when strictly applying quantum laws to increasingly large systems. This can be illustrated by considering the following measurement scenario: in a model experiment, an electron is delocalized and has equal probability of propagating through two distinct locations in space. Such spatial superposition states are fully described by quantum theory and are routinely invoked e.g. to understand the working of electron microscopy. We then perform a position measurement, which is accurate enough to reveal the position of the electron. If the superposition state evolves unitarily, as postulated by standard quantum mechanics, the pointer of the position meter will become entangled with the elec-

tron and finally be in a superposition of having measured one or the other electron locations. Now the entire measurement device will be in a very non-classical state. Where does this end? Does the quantum evolution break down when a critical number of atoms is involved? Or does it not even spare the experimenter from being in superposition of observing two distinct experimental outcomes? The inability of conventional quantum mechanics to answer these questions is known as the *measurement problem*, famously carried to the extreme by Schrödinger, with the aid of a cat and a deadly time bomb [12].

Several solutions have been proposed. Decoherence - i.e. the scrambling of phases caused by the quantum mechanical coupling of a system to its uncorrelated environment - was long believed to introduce a clear cut between the quantum realm and the classical world [14]. Even today, new decoherence mechanisms are proposed that supposedly possess this property [15]. While it is clear that decoherence can make quantum effects unobservable [16], it is argued that the increasing amount of entanglement, that is generated when a system is gradually coupled to its environment or a measurement device, does not introduce classicality but rather creates ever more complex quantum states. In brief, decoherence does not solve the measurement problem [17].

Everett's many worlds hypothesis takes the possibility of never-ending quantum evolution seriously and predicts the creation of new universes with each measurement act [18]. Since this is both a discomforting prospect and inherently untestable, theorists have focused on adding stochastic terms to the Schrödinger equation which govern the quantum to classical transition by randomly collapsing the wave function. This concept was first formulated by Ghirardi, Rimini and Weber [19] and later generalized to the Continuous Spontaneous Localization (CSL) model [20]. In line with this idea, Diosi and Penrose (DP) developed a model which assumes that the collapse is induced by the interplay between quantum mechanics and gravity [21, 22]. Experiments have been proposed to test the DP model [23], but no results are published to date. The CSL theory has been tested in various ways. According to the model, the interaction with a stochastic background field causes a collapse of the wave function and localization of particles at a mass dependent rate. First upper bounds were set by the Kapitza Dirac Talbot Lau matter-wave interferometer [24] and later by measurements of heating rates of a mechanical oscillator [25] and cold atoms [26]. Finally, X-ray spectra of Germanium [27] and, most recently, data from gravitational wave detectors [28] were used to exclude a large area of the CSL-parameter space. As the space of untested parameters shrinks, CSL is becoming less and less likely to be the solution to the measurement problem[1].

[1]Note that, even if one succeeded in detecting anomalous noise with a mass dependence similar to the one proposed for CSL, it would be hard or impossible to prove

The universality of the proposed collapse mechanism is indicated by the diversity of these experiments, yet none of them are, at the moment, actually sensitive to macroscopic superposition states. This is not a hindrance for a test of CSL, since the recoil associated with the localization would measurably effect system dynamics that are well described by classical mechanics [29–31]. Matter-wave interferometry, too, is sensitive to spontaneous wave function collapse [2], yet directly probes the superposition principle for a model-independent test of quantum mechanics in the limits of large mass or complexity.

This thesis documents the setup and characterization of an experiment that was designed specifically for this purpose: the Optical TIme domain MAtter-wave (OTIMA) interferometer. This Talbot Lau interferometer uses three pulsed photo depletion gratings and operates in the time domain [1, 3].

The OTIMA builds upon matter-wave research that was kicked off in 1923 with de Broglie's hypothesis, according to which a wavelength is associated with every massive particle [9]. This wavelength, λ_{dB}, is determined by the particle mass m, velocity v and Planck's constant h:

$$\lambda_{dB} = \frac{h}{mv} \tag{1.1}$$

Soon after its first formulation, the hypothesis was confirmed for electrons [32, 33], helium and hydrogen molecules [34], by the observation of diffraction at crystal surfaces. Neutron diffraction and interferometry followed [35–37]. Ramsey spectroscopy experiments with various atoms, which were carried out during the 1980s, were in hindsight identified as the first atom interferometers [38, 39]. Simultaneously, the progress in atom optics has enabled diffraction of atomic matter waves at a standing light grating [40] and later a mechanical grating structure [41]. Several three grating interferometers for atoms were presented a few years later, with material gratings [42], optical Raman gratings [43], optical phase gratings [44]. These setups operated in the far-field and coherently split the beam by more than the beam envelope. A near-field experiment in the Talbot Lau (TL) configuration, where the path separation may be on the order of the grating period, followed soon [45, 46]. Atoms interferometers are used today for absolute measurements of gravity [47], tests of the equivalence principle [48] or the search for dark energy [49], have even been launched on board a rocket very recently [50] and will be used for fundamental and applied experiments in outer space [51].

Atom interferometers have reached an impressive level of sophistication [52], however, they are less suited for detecting a breakdown of the quantum superposition principle, since, in this regard, the coherently en-

that this is not simply another decoherence mechanism.

closed area is expected to be less critical than the mass of the interfering particle [53]. This is where molecular matter-wave interferometry comes into play. The plan has been clear since the first far-field diffraction experiment with C_{60} fullerenes in 1999 [54]: to measure interference of increasingly heavy particles and compare the contrast to the predictions of standard quantum mechanics. The single-grating interferometer, a version of which is still running today [55], offers the same benefits as the atomic counterparts: it is comparatively easy to align, robust to vibrational dephasing and clear in the interpretation of the results, since there is no classical effect known to produce similar fringe patterns. The count rate, however, suffers from the stringent requirements for beam collimation. This is a deal breaker for interferometry in the limit of high mass, where signal intensity is usually a significant constraint. TL near-field interferometers require around 100 times weaker beam collimation, since each opening of the first grating functions as a point-like matter-wave source [45]. The first molecule interferometer that made use of this was comprised of three micro-mechanical gold gratings [56]. An optical phase grating replaced the center grating in the next version of the setup [57] which holds the current mass record in matter-wave interference [24]. While mechanical masks are arguably the most universal elements for matter-wave diffraction of small particles, since their working principle is, with a few exceptions [58], independent of internal particle properties, they suffer from several drawbacks: as the particles become heavier, slower and more polarizable, they interact more strongly with the grating walls via van der Waals or Casimir-Polder forces. These lead to velocity and position dependent phase shifts, requiring increasingly stringent velocity selection and thinner gratings [1, 56, 59]. Also, the grating period, thickness and quality are limited to the accuracy of lithographic production methods. And: mechanical masks break and clog. To overcome this, the idea of an all optical TL interferometer was conceived [60] and finally led to the setup of the OTIMA interferometer.

Since the time and distance for measuring TL interference scales quadratically with the grating period, we implemented grating lasers with the shortest wavelength commercially available: 157 nm Fluorine excimer lasers. These emit pulses of vacuum ultraviolet (VUV) light and allow to operate the interferometer in the time domain. The benefits of this scheme are outlined in section 1.1. When retro reflected at a mirror surface, the pulses form standing waves in which the photo depletion efficiency in the antinodes is high for many different types of particles, ranging from small molecules over van der Waals and metal clusters to large nanoparticles. This mechanism and other important aspects of the theory behind OTIMA are detailed in section 2.1.

Naturally, an OTIMA test of the wave-particle duality requires a thorough understanding of systematic effects and decoherence mechanisms

which is why the detailed characterization of the device was a focus of our work in the past years. Limits of the method are discussed in section 2.2. Since the fringe pattern in a TL interferometer can mimic a classical shadow of the grating structures, I have dedicated section 2.3 to the features that differentiate the classical effect from interference. The experimental setup and its main ingredients, including the grating lasers, the interferometer mirror, beam sources and detector assembly are discussed in chapter 3. I introduce the most important measurement protocols and techniques in chapter 4 and present the first results of cluster interference in section 4.2. The most common way to map out the interference pattern in the OTIMA setup is to record the dependence of the interference effect on the pulse separation symmetry. There are, however, several ways to record the spatial fringe pattern and methods to do so are reviewed in section 4.3. Crucial results for understanding the influence of systematic effects and new depletion mechanisms for VUV gratings are presented in sections 4.4 and 4.5, respectively. After proof of principle tests and characterization of the setup, the plan was conceived to explore the use of synthesized nanoparticles for OTIMA interference experiments. The requirements for such particles include favorable photoionization properties and scalability of the mass during the synthesis. Interim results of these ongoing test are discussed in section 4.6.

The OTIMA was from early on dedicated to fundamental tests of the wave-particle duality and will continue to serve this purpose. There are, however, spectroscopic advantages of OTIMA that shall be exploited in near-future experiments. These will rely on the sensitivity of the interference effect to external perturbations, which can be caused by the interaction of the particles with a spectroscopy laser beam, as described in more detail in section 5.1.

1.1 TL interferometry in time and space

At the heart of the OTIMA experiment lies the Talbot effect. This effect, known for nearly two centuries in classical optics [61, 62] and put to use in many other fields of technical imaging [63, 64], causes the emergence of sharp images of a coherently illuminated periodic object at specific distanced in the near field of this object. These distances are integer multiples of the Talbot length L_T, which is a function of the wavelength λ of the illuminating waves and the spatial period d of the illuminated object:

$$L_T = \frac{d^2}{\lambda} \tag{1.2}$$

In experimental situations where intrinsically coherent sources are unavailable, it is easier to observe a variant of the Talbot effect, the Talbot

Lau (TL) effect [65]. Here two identically periodic transmission masks G_1 and G_2, spaced by L_T and with parallel grating vectors, are illuminated by a spatially incoherent source. In this configuration, each opening of the first transmission mask will prepare transversal - i.e. parallel to the grating vector - coherence among the emerging wavelets. If the hereby prepared coherence sufficiently covers two openings of G_2, diffraction occurs and an interference pattern with periodicity d is projected in a plane parallel and spaced to G_2 by L_T. The observation of this effect with de Broglie matter waves requires thin transmission gratings, such that the distance between the gratings is well defined, and velocity selected particles. These two requirements ensure that all particles in the interferometer have the same time to build up coherence, after the first grating, or form a diffraction pattern after the second grating. This has been the working principle of many successful interference experiments with molecules [3, 56, 57].

The effect is illustrated further by resorting to a semi-classical point of view: A particle localized in a grating opening receives a recoil, parallel to the grating vector, and proportional to the size of the grating opening. In accordance to Heisenberg's uncertainty principle, this momentum transformation places the particles in a superposition state of being accelerated parallel and antiparallel to the grating vector. Since this *grating kick* leaves the forward velocity of a traversing particle unchanged, it is the time it takes particles to travel from grating to detector, or from grating to grating, rather than the flight distance, that is fundamentally important for the experiment[2]. In this *time domain* picture, the Talbot Lau effect occurs on a characteristic time scale

$$T_T = \frac{m\,d^2}{h}, \tag{1.3}$$

rather than a length scale. Contrary to the space-domain Talbot Lau effect, the pulsed optical gratings may be extended in flight direction, since it is not the distance between the gratings that must be well defined but the time between their appearance.

To make best use of the longitudinal velocity independence of the diffraction effect, one needs to detect the pattern over an extended region of space. This can be realized by pulses of UV light which are retroreflected at a mirror surface to form standing waves with periodicity $d = \lambda_L/2$, where λ_L is the wavelength of the laser. The waist of these pulses must be chosen such that all detected particles have been illuminated by the grating pulses. In order for a standing light wave to act as an absorptive grating, absorption of a grating photon must lead to the re-

[2]Velocity selection might still be required to ensure overlap of the particle cloud with the gratings, however, this does not enter the error budget of the visibility measurement.

moval of the photo-excited particle. This can happen via photoionization and subsequent deflection in an electrical field or photofragmentation, which recoils the fragments out of the beam [3, 4].

In most TL matter-wave interferometers, the interference pattern is recorded by masking the fringes with a third absorptive grating G_3, which is identical to the other gratings and placed a Talbot length away from G_2 [66]. Periodic variation of the number of particles behind G_3 occurs if this mask is scanned along the fringe pattern. If the particles are uniformly distributed in space, the count rate will remain constant during the scan. The grating-scan method is viable in the time domain case, too. This requires, ideally, one of the gratings to be formed at a separate mirror which is mounted on a translation stage to facilitate the scanning. Experimental ways to circumvent this need are discussed in sections 4.2 and 4.3.

Chapter 2

Theory

The following section will discuss aspects of the theory underlying the OTIMA experiment. Since the full mathematical treatment is comprehensively presented in other works [1, 67, 68], I will limit the discussion to results that are important for the understanding of the data in the experimental part of this thesis. The calculations that produce the equations and simulations in this section can be found in said references.

2.1 The OTIMA model

It is assumed in the following that a single absorption event suffices to trigger the removal of the particle from the beam and the particles are given to be at rest during the grating pulse as well as not have an spatial extension. Also, the gratings are assumed to act only on the particle dynamics in x-direction, i.e. parallel to the grating vector. The motional quantum state $\psi(x)$ of a particle is then transformed like $\psi(x) = t^{(k)}(x)\psi(x)$, where $t^{(k)}(x)$ is called the transmission function of the k-th grating (in the following referred to as G_k). The probability for a particle at position x to remain in the beam after the grating pulse is then given by $|t^{(k)}(x)|^2$, which equals the probability of not absorbing a photon and is thus given, under the assumption of poissonian statistics, by

$$|t^{(k)}(x)|^2 = \exp(-n^{(k)}(x)), \tag{2.1}$$

where $n^{(k)}(x)$ is the amount of photons absorbed in the k-th grating pulse at the position x:

$$n^{(k)}(x) = n_0^{(k)} \cos^2\left(\frac{\pi x}{d}\right) \tag{2.2}$$

Here, $n_0^{(k)}$ is the average number of photons absorbed at a anti node of the k-th grating and

$$n_0^{(k)} = \frac{4\sigma_{depl} E^{(k)} \lambda_L}{hc}, \tag{2.3}$$

where the single-photon depletion cross section is denoted with σ_{depl} and $E^{(k)}$ is the pulse energy of the k-th grating pulse[1].

Expanding expression (2.1) in a Fourier series results in

$$|t^k(x)|^2 = \sum_{m=-\infty}^{\infty} B_m^{(k)}(0) \exp\left(\frac{2\pi i n x}{d}\right), \tag{2.4}$$

where the Fourier components $B_n^{(k)}(\chi)$ for $\chi = 0$ are given by

$$B_m^{(k)}(0) = \exp\left(-\frac{n_0^{(k)}}{2}\right) J_m\left(-i\frac{n_0^{(k)}}{2}\right), \tag{2.5}$$

Here, J_m is the Bessel function of the first kind. This describes the transmission through a purely absorptive mask. Additionally, coupling of the particle's dipole polarizability α_L to the light field will modulate the phase of the wavefunction by imprinting the phase shift

$$\phi^{(k)}(x) = \phi_0^{(k)} \cos^2\left(\frac{\pi x}{d}\right) \tag{2.6}$$

onto the traversing matter waves at position x in the k-th grating. Here $\phi_0^{(k)} = 4\pi^2 E^{(k)} \alpha_L / hc$ is the difference between the average phase shifts experienced by particles at a node and at an antinode of the k-th grating. The particle properties α_L and σ_{depl} enter the calculations through parameters (2.3) and (2.6) it is convenient to introduce the dimensionless parameter β:

$$\beta = \frac{n_0^{(k)}}{2\phi_0^{(k)}} = \frac{\lambda \sigma_{depl}}{8\pi^2 \alpha_L} \tag{2.7}$$

When the phase grating effect is taken into account via β, the Fourier components of the gratings take the more complicated from:

[1]Throughout this section it is assumed that the mirror surface is perfectly flat and reflective, the grating lasers are aligned parallel to the mirror surface's normal vector and the longitudinal coherence length of the grating lasers is long enough too generate a standing wave with 100% contrast in the region where the particles are illuminated by the grating. In section 4.4 the formalism is modified to accept more realistic experimental parameters.

$$B_m^{(k)}(\chi) = \exp\left(\frac{-n_0^{(k)}}{2}\right)\left(\frac{\sin\,\pi\chi - \beta\,\cos\pi\chi}{\sin\,\pi\chi + \beta\,\cos\pi\chi}\right)^{\frac{x}{2}} \times J_m\left(\mathrm{sign}\left(\frac{\sin\,\pi\chi}{\beta} + \cos\,\pi\chi\right)\frac{n_0^{(n)}}{2\beta}\sqrt{\sin^2\,\pi\chi - \beta^2\cos^2\,\pi\chi}\right) \tag{2.8}$$

and the total grating transmission function reads

$$t^{(k)}(x) = \exp\left(-\frac{n^{(k)}(x)}{2} + i\phi^{(k)}(x)\right). \tag{2.9}$$

As expected, the transmission probability $|t^{(k)}(x)|^2$ does not depend on the strength of the phase grating. While $|t^k(x)|^2$ is not easily accessible experimentally, the total grating transmission $\mathcal{T}^{(k)}$ through the k-th grating is, and it follows by integrating $t^{(k)}(x)$ over an entire grating period d:

$$\mathcal{T}^{(k)} = J_0\left(i\frac{n_0^{(k)}}{2}\right)\exp\left(-\frac{n_0^{(k)}}{2}\right). \tag{2.10}$$

A plot of $\mathcal{T}^{(k)}(n_0^{(k)})$ is shown as a blue graph in figure 2.4*a* and *b*. One can now calculate the normalized density pattern of the particles after traveling for a time $2T$ through two of the described masks spaced in time by T

$$D(x,T) = \frac{1}{d}\sum_{l=-\infty}^{\infty} B_{-l}^{(1)}(0)B_{2l}^{(2)}\left(l\frac{T}{2T_T}\right)\exp\left(\frac{\pi i l(4x - aT^2)}{2d}\right) \tag{2.11}$$

Here the presence of an acceleration a along the grating vector, e.g. in the earth's gravitational field, was taken into account. Thanks to the Talbot Lau effect, $D(x,T)$ is d-periodic in x if T is an integer multiple of T_T. This interference pattern can be resolved by masking it with a third grating G_3, which is identical to G_1 and G_2. The absorptive mask G_3 will then deplete the beam at its antinodes and allow only for the particles in its nodes to be transmitted to the detector.

The amount of signal at the detector depends on the relative shift Δx between $D(x,T)$ and G_3. In a three grating setup, this fringe shift Δx is a function of the positions Δx_k of all three gratings with respect to a common reference:

$$\Delta x = \Delta x_1 - 2\Delta x_2 + \Delta x_3 \tag{2.12}$$

Constructive (destructive) interference occurs for $\Delta x = 0$ ($\Delta x = d/2$). This case will, in the following, also be referred to as positive

(negative) contrast. Note how the shift Δx is independent of d and holds, for geometrical reasons, for the classical shadow of three transmission masks as well as for a pattern formed by matter-wave diffraction[2]. The Signal behind the third grating reads

$$S(\Delta x, T) = \frac{1}{d} \sum_{l=-\infty}^{\infty} B_{-l}^{(1)}(0) B_{2l}^{(2)} \left(l \frac{T}{2T_T} \right) B_{-l}^{(3)}(0) \exp\left(\frac{\pi i l}{d} (4\Delta x - aT^2) \right) \tag{2.13}$$

The symmetric pulse separation time ΔT is defined as

$$\Delta T \equiv T(G_2) - T(G_1) = T(G_3) - T(G_2), \tag{2.14}$$

where $T(G_k)$ is the appearance time of the k-th grating pulse. The treatment in this section here is limited to the case $T = \Delta T$. In such a time-symmetrical situation, the Talbot Lau effect is most robust and offers the highest contrast[3]. A few features of $S(\Delta x, t)$ must be emphasized. Firstly, since $B_{-l}^{(1)}(0) = B_{-l}^{(3)}(0)$, the first and third grating influence the signal in exactly the same way. Secondly, $B_l^{(k)}(0)$ only depends on $n_0^{(k)}$ and not on $\phi_0^{(k)}$. G_1 and G_3 thus alter the signal only via particle depletion, not via dipole interactions and may be treated as purely absorptive masks. Also, the particles impinge on G_1 with a transversal momentum distribution that is broad compared to the grating kick $\hbar\pi/d$ or the deflection arising from optical forces in G_1. This explains why, for a weakly collimated beam of particles, no interference effects are visible behind G_1 and G_3, which can thus be treated as classical transmission masks.

The periodicity of $S(\Delta x, t)$ can be measured either by scanning the fringe shift Δx via the grating phases or by a variation of the acceleration along the grating vector. Before investigating the dependence of $S(\Delta x, t)$ on experimental parameters such as grating pulse power or pulse timing, one needs a suitable measure for the contrast. In many cases $S(\Delta x, t)$ is sine shaped and its contrast is defined as the common interference visibility

[2]Differences between the fringe shift of a shadow image and an interference pattern arise in the limit of very strong particle beam collimation, when the width of the momentum distribution in x-direction becomes smaller than the *grating recoil* $\hbar\pi/d$. In this case, classical shadows cannot form at certain grating configurations Δx_k, since all classical trajectories are blocked, while an interference pattern can nevertheless form due to the coherent spread of transversal momenta.

[3]It is possible to observe contrast when $T(G_2) - T(G_1) = 1.5(T(G_3) - T(G_2))$, for example. This is interesting since it allows to operate the interferometer in a magnifying mode rather than the self-imaging mode [69]. The discussion will, however, focus on the symmetric configuration, since magnification of the interference pattern was not useful for the experiments presented in this thesis.

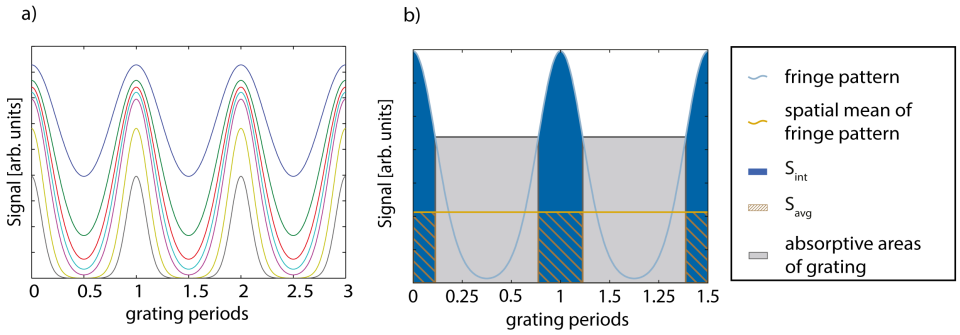

Figure 2.1: a) Simulated interference patterns for different G_2-powers. Low grating power ($n_0 = 3$) results in the blue curve which is nearly sine shaped and has a contrast of $S_{vis} = 34\%$. For increasing G_2-power the contrast increases (the higher the power, the lower the fringe pattern in the graph), until it saturates at $S_{vis} = 100\%$ for the yellow and black graphs ($n_0 = 20$ and $n_0 = 30$, respectively) which are no longer well represented by a sine wave. S_N for these curves is 2 and 4, respectively. b) A simulated interference pattern is shown as a blue line. The spatial mean of this pattern is the yellow line in the graph. The absorptive areas of G_3 are colored in gray. Here $\Delta x = 0$, and everything between the gray areas is transmitted to the detector. S_N is related to S_{int} (blue areas) and S_{avg} (red shaded areas) via definition (2.16).

$$S_{vis} = \frac{S_{max} - S_{min}}{S_{max} + S_{min}}, \tag{2.15}$$

i.e. via its extremal values S_{max} and S_{min}. This, however, is no longer a good measure for the contrast of the pattern, when the shape of the pattern increasingly deviates from a sine, which is the case for strong grating powers and small grating openings, as illustrated in figure 2.1*a*. For patterns that are not well represented by a sine curve it is more accurate to measure the contrast in terms of the *normalized signal* S_N. The area of the fringe that is transmitted by G_3 is integrated and normalized with the integral over the fringe pattern, as shown in figure 2.1*b*. If S_{int} is the area under the fringe and S_{avg} is the area under the spatial mean, then one can define S_N as

$$S_N = \frac{S_{int} - S_{avg}}{S_{avg}} \tag{2.16}$$

S_{avg} results from detuning the interferometer from symmetry by δT, so that

$$[T(G_2) - T(G_1)] - [T(G_3) - T(G_2)] = \delta T, \tag{2.17}$$

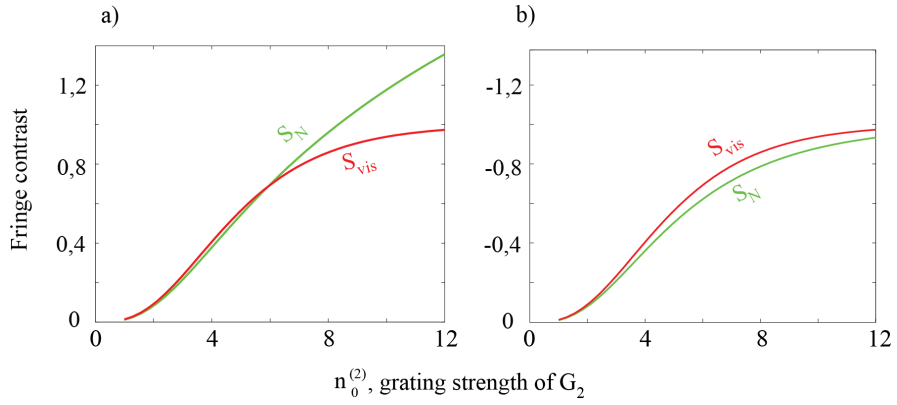

Figure 2.2: Simulations of S_{vis} and S_N versus G_2 grating strength $n_0^{(2)}$ for positive contrast $\Delta x = 0$ (panel a) and negative contrast $\Delta x = d/2$ (panel b).

and measuring the transmission though all three gratings, since for suitably large δT, no contrast is expected[4]. Using S_N as a measure for the contrast is convenient since it can be obtained without a scan of the fringes.

Figure 2.2 compares the expected S_N and S_{vis} for different laser powers in the second grating, where $n_0^{(1)} = n_0^{(3)} = 10$ and $\Delta T = T_T$ was assumed. For small powers, where the contrast is low, both measures give similar results. For larger powers and higher contrast, deviations appear, up to the point where S_{vis} is bound by 1 and S_N increases with no upper bound. For negative contrast, i.e. $\Delta x = d/2$, S_N is a good approximation for S_{vis}. S_N is a more accurate measure of high contrast, since it is sensitive to pattern changes when S_{vis} is already saturated. This can be beneficial for experiments where fringe shifts due to gravitational, rotational or electromagnetic deflection are measured. In such a situation one benefits from a steep fringe slope and measuring S_N allows to optimize the experiment accordingly. In the rest of this section, however, S_{vis} will be used since it is easier to grasp and illustrates equally well how the interferometer reacts to the variation of parameters.

Figure 2.3a shows the expected visibility S_{vis} as a function of the pulse delay time ΔT in units of the Talbot time for $\beta = 1,5$ (solid blue line), $\beta = 0,4$ (dotted blue line) and $\beta = 1$ (dashed blue line). Resonances occur at $\Delta T/T_T \lesssim n$, where n is an integer [5]. The n-th contrast maximum corresponds to the n-th Talbot order. The width of the resonances depends on the polarizability of the particles: the larger α_λ, the

[4]The amount of asymmetry necessary to make the contrast disappear depends on the divergence angle of the particle beam, as explained in section4.1.

[5]For particles in a low field seeking state β is negative and contrast is highest for $\Delta T/T_T \gtrsim n$, where $n \in \mathbb{N}$.

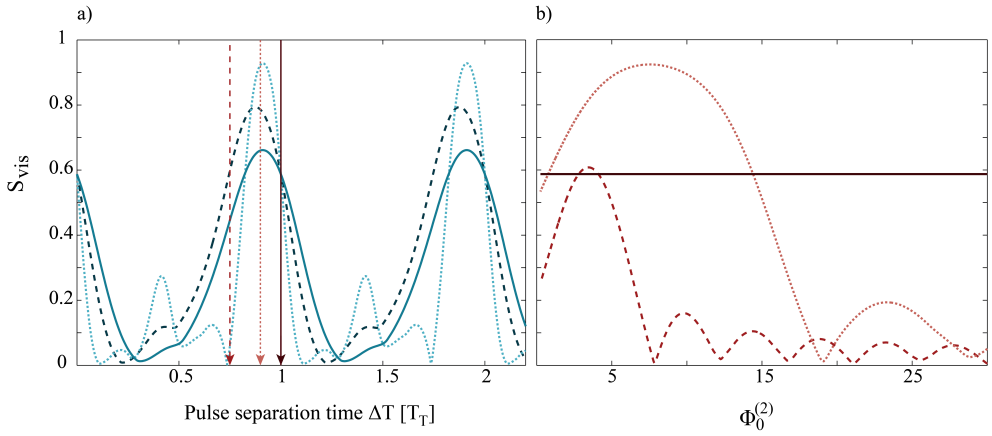

Figure 2.3: *a*) Expected S_{vis} as a function of the pulse separation time in units of the Talbot time for $\beta = 1, 5$ (solid line), $\beta = 0, 4$ (dotted line) and $\beta = 1$ (dashed line). The contrast is highest for ΔT slightly shorter than integer multiples of the Talbot time. The vertical brown arrows mark the three times at which S_{vis} is evaluated in *b*) as function of $\phi_0^{(2)}$, the phase shift at an antinode of G_2, which is related to α_λ according to equation (2.7). The contrast is independent of the polarizability (i.e. no phase grating effect occurs in G_2) when ΔT is exactly equal to the Talbot time or an integer multiple hereof. A version of this figure is published in [5].

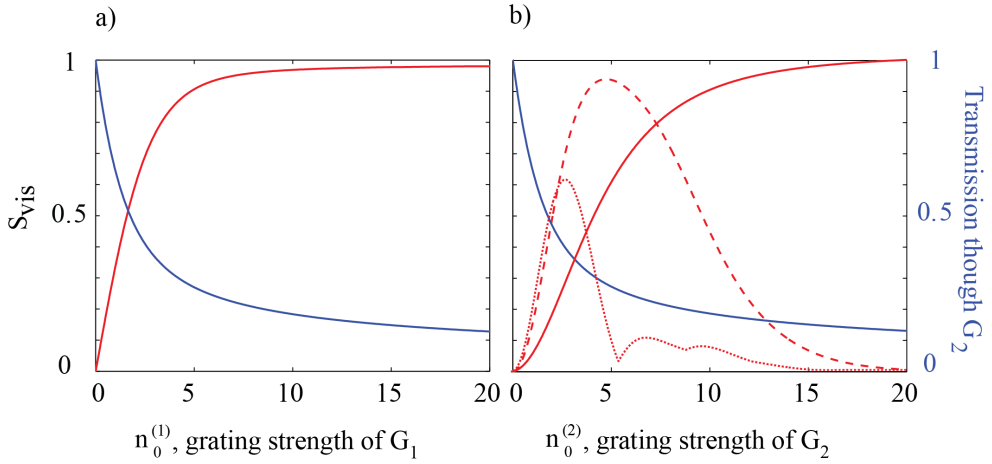

Figure 2.4: *a*) Transmissivity $\mathcal{T}^{(1)}$ though G_1 (blue line) and S_{vis} (red line) as a function of absorbed grating power in G_1. *b*) Transmissivity $\mathcal{T}^{(2)}$ though G_2 (blue line) and S_{vis} (red lines) as a function of absorbed grating power in G_2. Pulse times were set to $\Delta T = T_T$ (solid red line), $\Delta T = 0.8T_T$ (dashed red line) and $\Delta T = 0.6T_T$ (dotted red line). For all simulations the optical properties were set to $\beta = 0.5$ and the other gratings fixed at $n_0 = 9$.

narrower the resonance. The fractional Talbot effect occurs between two Talbot maxima, which is most pronounced for $\beta = 0, 4$ (dotted blue line). Since the particle beam is assumed to illuminate infinitely many grating openings, each resonance is of the same height for a given β.
For three different pulse separation times $\Delta T = 0.75\,T_T$ (dashed arrow), $\Delta T = 0.9\,T_T$ (dotted arrow) and $\Delta T = T_T$ (solid arrow) the strength of the phase grating was evaluated. This is shown in part b of the figure, where S_{vis} is plotted versus the phase shift $\phi_0^{(2)}$, which is proportional to both the optical polarizability α_λ and to the G_2 laser power. No phase grating effect occurs when $\Delta T/T_T = n$ and $n \in \mathbb{N}$. This can be seen in equations (2.14) or (2.11) where all $\phi_0^{(2)}$ dependent terms in $B_{2l}^{(2)}$ cancel out (see definitions 2.8 and 2.6). This reduces the Talbot coefficient of the second grating to (2.5). Intuitively, this can be understood by reexamining the Talbot effect: on Talbot resonance, an exact replica of the matter-wave phase image in G_2 is projected onto G_3. At the appearance time of G_2, however, there is no phase pattern yet, since it requires a certain time to build up. Hence, the fringe pattern formed on Talbot resonance is independent of the dipolar interaction in G_2 and the polarizability must not be known in order to predict the interference contrast. This feature was used for the experiments described in section 4.4.

The grating power dependence of S_{vis} and the transmission though a single grating and $\beta = 0.5$ are shown in figure 2.4. Panel a shows the dependence of the contrast on $n_0^{(1)}$ as a red solid line, where the other gratings were fixed at $n_0^{(2)} = n_0^{(3)} = 9$ and $\Delta T = 0.97\,T_T$. Exchanging the role of G_1 and G_3 produces an identical graph. For panel b, $n_0^{(2)}$ was varied and $n_0^{(1)} = n_0^{(3)} = 9$ fixed for three different pulse separation times: $\Delta T = T_T$ (solid red line), $\Delta T = 0.8\,T_T$ (dashed red line) and $\Delta T = 0.6\,T_T$ (dotted red line). While for $\Delta T = nT_T$ and $n \in \mathbb{N}$ the contrast only increases with $n_0^{(2)}$, as expected for diffraction at an absorptive mask with decreasing grating openings. For $\Delta T < T_T$ or $\Delta T > T_T$, the contrast can also decrease with increasing $n_0^{(2)}$ due to the phase grating effect. The shape and height of the visibility curve strongly depend on the pulse timing.

Examining the power dependences of the transmission and the fringe contrast shows that the choice of laser power is always a trade-off between high contrast and high particle throughput.

2.2 Limits of OTIMA interferometry

In this section, the limits of OTIMA will be discussed, some of which are specific to the current experiment and can be alleviated in a future version. This includes the sensitivity to machine vibrations and gravitational deflection. Some are universal, such as the requirements for vacuum and internal particle temperature. Generally, two categories of contrast reducing effects can be identified: Machine vibrations and gravitational deflection constrain the experiments to a certain range of useful pulse separation times ΔT. On the other hand, the observation of interference will eventually be hampered, to an extent that depends on the particle mass and size, by decoherence due to collisions with background gas particles, emission and absorption of thermal radiation and particle-size effects in the gratings. The following simulations of decoherence in OTIMA are based on results published in [2].

Vibrations and thermal drifts induce fringe fluctuations in multi-grating interferometers [70]. The OTIMA setup is inherently well protected from these influences because a common boundary for the standing waves is established by the use of a single mirror. This one can read off relation (2.12): if a shift or tilt of the mirror surface appears on a timespan much slower than ΔT, it effects Δx_1, Δx_2 and Δx_3 proportionally and thus does not influence the overall fringe phase Δx. For a grating period of $d = 79\,\mathrm{nm}$, vibrational dephasing will reduce the contrast from 1 to the 1/e if the mirror is displaced by $x_c = 15\,\mathrm{nm}$ during the timespan of ΔT. From this follows a critical mirror velocity $v_c = x_c/\Delta T$, that should not be exceeded. In a sinusoidal oscillation with amplitude x_m and frequency f, the maximal velocity is $v_m = 2\pi f x_m$. One thus arrives at the criterion

$$v_m \overset{!}{<} v_c \implies x_m(f,m) < \frac{x_c h}{2\pi m d^2 f}, \tag{2.18}$$

where ΔT was substituted by the Talbot time $T_T = md^2/h$ as defined in equation (1.3). In figure 2.5, x_m is plotted as a function of particle mass for f = 500 Hz, 1000 Hz, 2000 Hz and 3000 Hz. These frequencies cover the range of mechanical noise sources common to a high vaccum apparatus like the OTIMA. The horizontal dashed line marks the threshold above which $x_m < 1\,\mathrm{nm}$ and the vertical lines indicate the corresponding masses, above which the contrast would be reduced to 1/e if $x_m > 1\,\mathrm{nm}$.

Since 1 nm amplitude of mechanical noise on the vacuum chamber and mirror mount is a realistic estimate, vibrational dephasing can be expected to compromise experiments with particle masses larger than 75 000 amu. Fortunately this can be compensated for in a time domain setup: since the grating position is relevant only during the grating lifetime, which in the OTIMA setup amounts to 7 ns, the mirror position

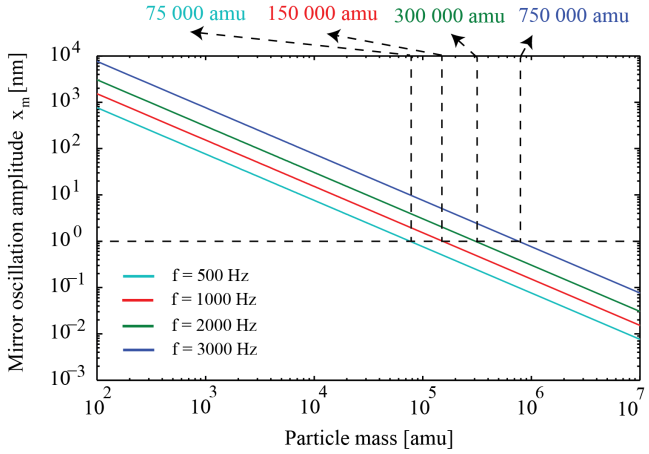

Figure 2.5: Mirror oscillation amplitude x_m, for which the interference contrast of a particle with mass m is reduced to 1/e of its highest value. x_m is plotted for four common mirror oscillation frequencies. The dashed lines indicate the highest masses that can be interfered with a contrast larger than 1/e if $x_m = 1\,\mathrm{nm}$.

can be measured, time tagged and later correlated with the interference sequence. This will allow, either, to post select only those experiments with a fixed fringe phase Δx, or use all measurements for an effective scan of Δx. In such a way one could resolve the interference pattern in space, provided the mirror is displaced by more than a grating period during its oscillations.

In the current OTIMA setup, the grating vectors are oriented parallel to gravity. From this follows a limit to the duration of the experiments since the particles are deflected to regions of the gratings where, due to the limited longitudinal coherence length of the lasers, the standing wave visibility is reduced. As depicted in figure 3.2 and explained in section 3.1, the standing wave visibility drops to 40 % in a distance of 0.5 cm from the mirror surface. From inserting the gravitational deflections at the grating trigger times, $\Delta x_1 = 0$, $\Delta x_2 = g\Delta T^2/2$ and $\Delta x_3 = g(2\Delta T)^2/2$, into expression (2.12), one arrives at a total fringe shift of $\Delta x = g\Delta T^2$, where g is the gravitational acceleration. Δx reaches the critical value of 0.5 cm for $\Delta T = 22.4\,\mathrm{ms}$, which is the Talbot time of a particle with mass of $1.5{\times}10^6$ amu. For experiments with masses much larger than this, the gravitational deflection could be compensated for by uprighting the interferometer, such that the particle beam is parallel to gravity.

An obvious limit to high mass OTIMA interferometry arises when the diameter of the particles reaches a significant fraction of the grating period d. In this case, particles average of the grating structure, which reduces the grating strength and hereby the contrast. For gold clusters, this contrast-reducing size effect starts to play a role for particles heavier

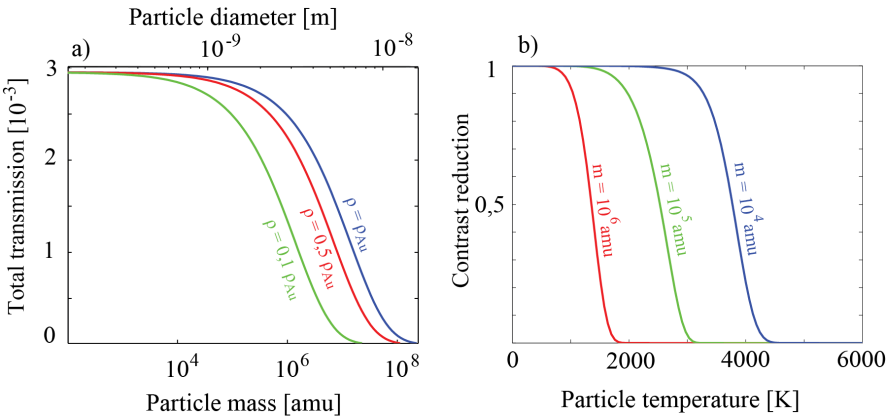

Figure 2.6: *a*) Calculated transmission though three OTIMA gratings for gold particles of increasing mass and diameter (blue curve). The red and green curve show the transmissions of particles with optical properties similar to gold but with smaller densities. The grating power is scaled with mass to ensure constant contrast. *b*) Expected contrast reduction due to emission of thermal radiation as a function of internal particle temperature for gold particles with $m = 10^4$ amu, $m = 10^5$ amu and $m = 10^4$ amu. The environment was assumed to be cooled to a temperature of 100 K.

than 10^8 amu (see blue line in figure 2.7). Much before this limit is reached, however, the transmission will tend to zero, since the particles always cover high energy regions of the gratings. To a certain degree, this can be compensated by scaling down the laser power. The total interferometer transmission is plotted for gold clusters in figure 2.6*a* (blue graph). Here, the laser power is assumed to be scaled such that the contrast is at its highest possible value. The optical properties were set to the bulk values of gold from [71]. The simulation was repeated under the assumption of the same optical particle properties but with 10 times (green graph) and 2 times (red graph) smaller particle density, approximately corresponding to the bulk densities of silicon and silver. For the least dense particles, the simulation shows that size effects start influencing the transmission already at 10^4 amu, or particle diameters of 0.5 nm. For the densest particles, the effect is not relevant until a mass of 10^5 amu.

Internally hot particles cool down by emitting thermal radiation, leading to decoherence if it happens during the flight through the interferometer [16]. The effect increases with ΔT, since more emission events occur and the photon recoil leads to larger transversal shifts of the emitting particles. The contrast reduction on Talbot resonance due to thermal decoherence is shown in figure 2.6*b* for gold particles with $m = 10^4$ amu, $m = 10^5$ amu and $m = 10^6$ amu. The simulation also incorporates the

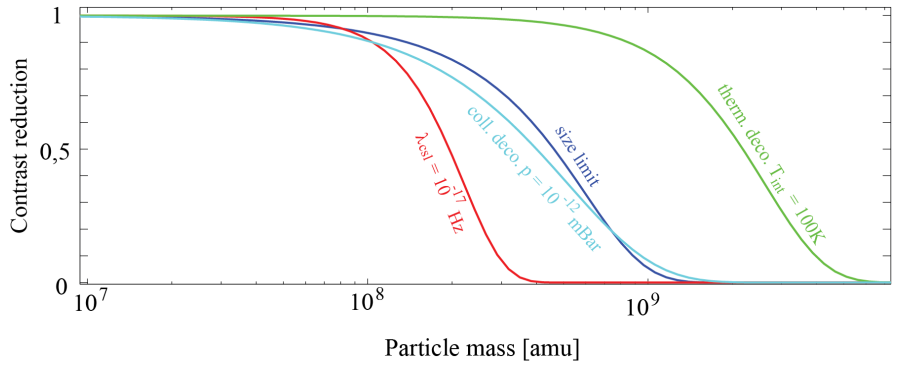

Figure 2.7: The bound on interference of gold clusters introduced by the CSL model with a localization frequency of $\lambda_{csl} = 10^{-17}$ Hz (red graph) is compared to the size effect (blue graph), reduction due to emission of thermal radiation (green graph) and collisional decoherence (light blue graph). For the latter two simulations it was assumed that the environment and the particles are in thermal equilibrium at 100 K and that the pressure in the interferometer region is $p = 10^{-12}$ mbar.

effect of scattering of black body radiation from the environment, which plays a minor role under the assumption of an environmental temperature of 100 K. The results demonstrate the necessity to cool large particles internally, since, for a particle with a mass of $m = 10^6$ amu, already 1000 K is too hot to observe the full contrast. Buffer gas cooling might be a viable option for obtaining a beam of internally cool particles. The feasibility of pulsed buffer gas cooled beams is currently under investigation in our lab.

Finally, decoherence due to the collision of particles with molecules in the background gas must be taken into account. The effect has been observed in a TLI experiment with C_{60} fullerenes [72] and has been theoretically investigated in the context of OTIMA interferometry [2]. The reduction factors that were calculated in said reference are plotted in light blue as a function of gold cluster mass in figure 2.7. For a mass of 4×10^8 amu and a pressure in the interferometer chamber as good as $p = 10^{-12}$ mbar, the contrast is reduced to 50 %. Although it presents an experimental challenge to obtain such low pressures, they are reachable with common techniques.

In figure 2.7 the mass dependence of thermal and collisional decoherence as well as the size effect is compared to the bounds introduced by the most widely studied collapse model, namely the continuous spontaneous localization (CSL) model. Within this theory, a nonlinear term is added to Schrödinger equation, which interrupts the standard quantum evolution by randomly collapsing spatial superpositions at a mass dependent rate [73]. The CSL model is characterized by the frequency

λ_{csl} at which collapse occurs and r_{csl}, the spatial resolution of the subsequent localization. When CSL was first introduced, the authors suggested $\lambda_{csl} = 10^{-17}\,\mathrm{Hz}$ and $r_{csl} = 100\,\mathrm{nm}$ [20]. These bounds are still open for the test, despite the recent progress in ruling out the CSL model over a large parameter space [25, 27]. The simulations show that the decoherence mechanisms discussed here would not prevent an OTIMA test of the CSL model in the mass range between 10^8 and $10^9\,\mathrm{amu}$. This would require, however, to perform the measurements in an environment with reduced gravitational acceleration, since the gravitational deflection currently imposes the most stringent mass constraints on OTIMA interferometry.

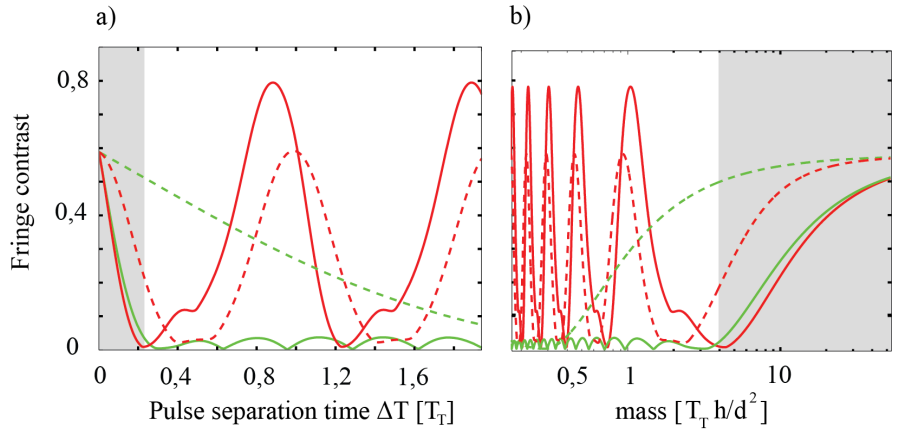

Figure 2.8: Simulated fringe contrast as function of the pulse separation time (panel a) and mass (panel b). The red curves show several orders of the expected interference contrast for $n_0 = 6$ in all three gratings and $\beta = 1$ (solid red line) and $\beta = 10$ (dashed red line) . The same parameters were assumed for the simulation of the contrast of a grating shadow shown in green. The gray-shaded area marks a regime, where matter-wave interference cannot be distinguished from a classical description for $\beta = 1$.

2.3 Interference pattern or shadow?

The observation of a d-periodic particle density in a Talbot-Lau interferometer with grating periods d may also be interpreted in terms of classical particle trajectories. For a solid test of the wave-particle duality one must therefore operate the three-grating setup in a regime where matter-wave diffraction can clearly be distinguished from classical pathways. The dependence on the pulse separation time ΔT of the two effects are compared in figure 2.8. Here, the simulated fringe contrast is shown as a function of ΔT in units of the the Talbot time (panel a) and as a function of particle mass (panel b), for particle dynamics governed by quantum (red graphs) and classical mechanics (green graphs). For the calculations, all three gratings were set to $n_0 = 9$ (see definition (2.3)). The particle properties, represented by the parameter β (see definition (2.7)) were set to $\beta = 1$ for the solid graphs and to $\beta = 10$ for the dashed green graphs. For very small ΔT, this regime is shaded in gray, the classical effect cannot be distinguished from matter-wave interference for $\beta = 1$. The classical shadow contrast is generally larger when the lensing is strong and the grating opening fraction is small. This is simulated by using a larger β parameter. Here the classical model predicts contrast of nearly 40 % at timings at which also the first Talbot order appears. Only particles with very low polarizability will exhibit β values this high. For atoms these can appear at so called *tune out* wavelengths [74]. For

molecules or nanoparticles, the occurrence of tune out wavelengths would require unusually narrow absorption resonances. Still, the example illustrates that contrast measurements at a single pulse separation time allow to distinguish with certainty between the classical effect and interference if the particle properties are well known and the interferometer is well characterized[6].

For particles with less well-defined properties it is favorable to measure the contrast as a function of ΔT. The quantum effect is expected to show characteristic contrast resonances. The classical effect shows an oscillatory behavior as well (see the solid green graphs in figure 2.8) due to lensing in G_2, yet the expected contrast is much lower for pulse separation times outside the gray area. The separation between two contrast revivals in the classical picture depends on the strength of the lensing and on the laser power in in G_2. On the other hand, the absolute time difference between two maxima in the interference contrast is determined only by the particle mass and the grating period. If it is possible to measure the contrast as a function of pulse separation time and to resolve contrast revivals spaced by the Talbot time, one can confidently claim the quantum origin of the observed particle density fringes. This requires either a particle beam with a broad velocity distribution, such that one can change the pulse timing without reducing the overlap of particle pulse with the gratings, or a variable spatial distance between the gratings. In situations where the particle beam contains a distribution of masses, it is often not even necessary to measure at various ΔT. Instead one can trace the fringe visibility as a function of mass, as simulated in figure 2.8b.

The methods discussed so far require the β values to be known at least approximately, since in a *worst case* scenario, the particle properties could change with velocity or mass such that the classical prediction mimics the characteristic behavior of interference. This *loophole* is closed by investigating the ΔT dependence of the spatial period of the interference pattern, as pictured in figure 2.9. The upper panel shows the expected visibility of the interference (red graph) and shadow effect (green graph) as a function of ΔT in units of the Talbot time and for $\beta = 10$ and $n_0 = 10$. At each point on these graphs, the spatial fringe pattern before G_3 was computed and its period calculated via fast Fourier transform. This is plotted in the lower panel. Both effects produce d-periodic patterns at full Talbot orders. At fractional Talbot orders, i.e. for $\Delta T = 0.5\,T_T$, $\Delta T = 1.5\,T_T$ etc, the interference fringe period is half of the grating period, while the shadow image has periodicity d. This allows to distinguish the two effects without the knowledge of exact parti-

[6]Note that for gratings with unknown quality, the exact values of n_0 are *a priori* unknown, too. This additionally complicates the interpretation, as detailed in section 4.4

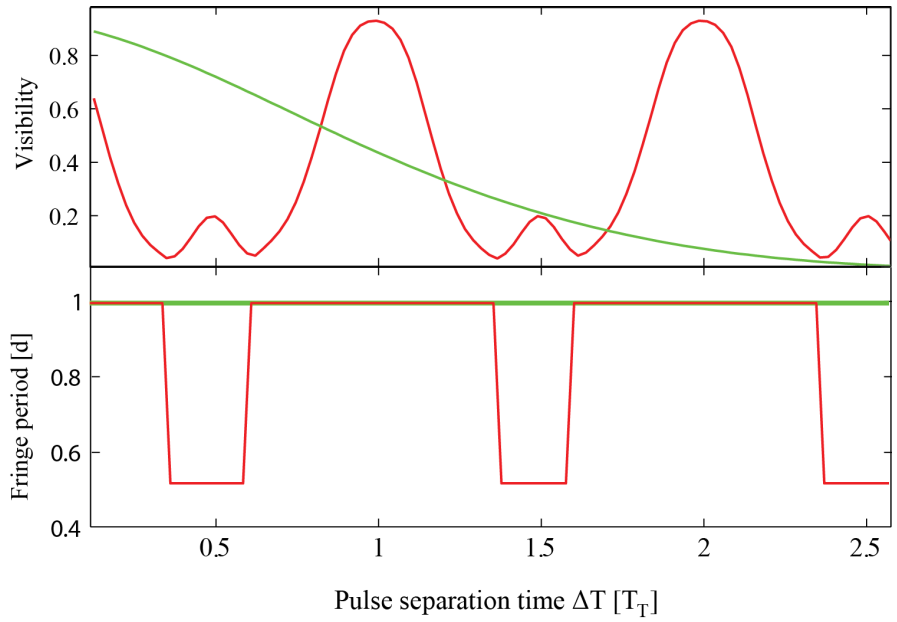

Figure 2.9: Computed interference (red graph) and shadow visibility (green graph) for $\beta = 10$ and $n_0 = 10$ as a function of symmetric pulse separation time ΔT in units if the Talbot time T_T (upper panel). The lower panel shows the spatial period of the fringe patterns in units of the grating period d. At fractional Talbot orders, only the interference effect (red graph) produces $d/2$-periodic patterns. The shadows, time independantly, exhibit a period of d.

cle properties. Experimental techniques for recording spatial interference patterns in OTIMA are discussed in section 4.3 and have been used to resolve fringe patterns at the first Talbot order. While contrast was observed at fractional Talbot orders (see figure 4.6), the spatial resolution of a $d/2$-periodic pattern is an outstanding challenge. Although high contrast at fractional Talbot orders requires very small grating openings and thus appears only for very small particle transmissions, it is the best option for a high-mass test of the wave-particle duality.

Note that for measurements of particle properties in the OTIMA interferometer, such as deflectrometry or spectroscopy (see section 5.1) it is not necessary to prove the quantum origin of the fringe pattern since the classical effect and interference, for given ΔT and contrast, are equally sensitive to shifts, perturbations and the action of decoherence mechanisms. Grating deflectrometers make use of this classical effect and can be seen as the classical analogue to TL interferometers [75].

Chapter 3

Experimental setup

Figure 3.1 shows a drawing of the OTIMA interferometer. The Experiment in its most basic configuration is housed in at least three vacuum chambers: the main chamber (MC), the optics chamber (OC) and a source chamber (SC). The main chamber accommodates the interferometer mirror and the mounting assembly, as well as a time-of-flight mass spectrometer (ToF-MS). It is pumped via three turbo molecular pumps with a total pumping speed of 1000 l/s for N_2[1]. For additional pumping power, a baffle (B) may be cooled with liquid nitrogen (LN2). Pressures as low as 2×10^{-9} mbar can be reached with this configuration. Two linear translation stages are fed through the chamber wall with which horizontal (H) and vertical (V) delimiter slits can be positioned to collimate the particle beam. A high-voltage feed through connects a wire electrode in proximity to the interferometer mirror surface to a power supply. The electrode is typically charged with 1 kV and serves to deflect ionized particles out of the opening volume of the detector and away from the mirror surface. In the opening of the ToF-MS, the particles are ionized by a 157 nm excimer laser[2].

All the optics, with exception of the interferometer mirror, are mounted inside of a dedicated vacuum chamber, the optics chamber. Within this chamber, the VUV light is guided from the apertures of the three grating lasers into the main chamber. Each beam line contains two mirrors mounted on remote controlled mounts allowing in-situ alignment of the beams without breaking the vacuum. A biased GaP photodiode collects stray light from the optics and allows emission-timing and power monitoring of the grating lasers. Finally the beams are focused onto a point about 10 cm behind the interferometer mirror with cylindrical lenses. The main chamber is interfaced to the optics chamber via a window of 8 cm in diameter.

The source chamber has been adapted several times to accommodate

[1] 2x Pfeiffer Vacuum Hi Pace 700 and 1x Pfeiffer Vacuum Hi Pace 300
[2] Coherent Excistar XS 200

various beam sources. A continuous-beam metal cluster source [76] was originally attached to the apparatus. Later this source was replaced with the Even Lavie valve [77] which produces intense and μs-pulsed beams of clusters of organic molecules. This source is described in more detail in section 3.4.2. The aggregation of clusters in both of the mentioned sources relies on several bar pressure of a noble seed gas. This puts high demands on the pumps in the source chamber and necessitates at least one differential pumping stage as an interface between the source chamber (typical vacuum of 5×10^{-4} mbar) and the main chamber (typical vacuum of 5×10^{-9} mbar). For the experiments with the laser heating source (described in section 3.4.3) the source chamber was swapped to a custom-made cube which contains a liquid nitrogen cooled copper baffle structure and allows to mount and manipulate a sample plate inside the vacuum. Since the laser heating source operates without buffer or seed gas, vacuum as good as 2×10^{-7} mbar can be maintained in this chamber during source operation. The alleviates the need for a differential pumping stage.
Photographs of the experiment can be found in Appendix 1.

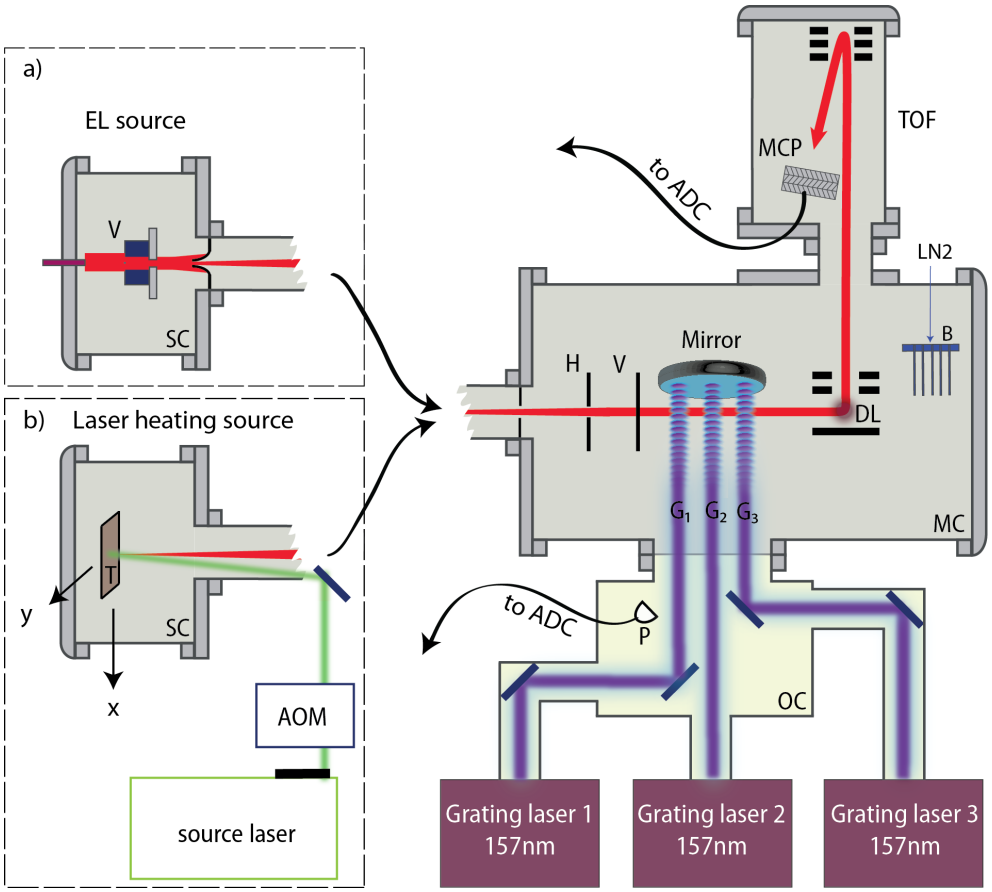

Figure 3.1: Sketch of the OTIMA setup. Two source chambers (SC) have been used for the experiments in this thesis: *a*) the Even Lavie (EL) source and *b*), the laser heating source. The latter requires a source laser beam to be focused on the target plate (T). This laser can either be a pulsed nanosecond laser or a continuous laser which is chopped with an acousto-optic modulator (AOM). The particle beam enters the main chamber and is collimated with horizontal (H) and vertical (V) slits. The actual interferometer consists of the interferometer mirror and the standing wave gratings. These are formed by the grating laser beams, which are manipulated by lenses and mirrors in the optics chamber (OC). After passing though the gratings, the particles are ionized by the detection laser (DL) and accelerated into the drift tube of the reflectron time-of-flight mass spectrometer (TOF), where they finally hit a micro-channel plate (MCP). The signal from the MCP and the photodiode (P) are digitized by an analog-to-digital converter (ADC) and fed to a PC for processing. All chambers are evacuated by turbo molecular pumps (not pictured). The vacua in the MC and SC *b*) can additionally be improved by liquid nitrogen (LN2) cooled baffles (B). A version of this figure is published in [3]

3.1 Grating lasers

In the OTIMA setup, the light for the optical gratings is provided by three identical *GAM EX50* excimer lasers. These lasers are discharge pumped Fluorine lasers that emit at two vacuum ultraviolet wavelengths around 157 nm with a repetition rate up to 250 Hz. The active gas, a mixture of He 99.7 vol% and F_2 0.3 vol% is contained in a sealed and passivated tube, which houses the cavity assembly. The cavity of the lasers has a length of 50 cm and consists of a high-reflector mirror (R = 98 %) and an uncoated output coupler, both manufactured from CaF_2. Electrodes are mounted along the cavity axis, from which up to 16 kV of high voltage are discharged, triggered by a thyratron which acts as a low-jitter high-voltage switch. We have measured the trigger-to-emission jitter to lie below 5 ns FWHM. This jitter is accompanied by a constant 2-3 μs trigger-to-emission delay. The pulse length and energy are specified to 5 ns and 4 mJ, respectively. The pressure of the active gas determines the output power and can be changed from slightly above room pressure up to 3 bar. The output spectrum of a similarly constructed laser is shown in figure 3.2*a*. It exhibits several emission lines, the most pronounced of which are at 157.52 nm and 157.63 nm with a intensity ratio of 1/5 and a FWHM line width of 0.85 pm [78]. The light gratings in the OTIMA are superpositions of standing waves formed by running waves of all the wavelenghts contained in these two spectral lines. The simulated intensity of such a standing wave (SW) is presented in figure 3.2*a* as a function of the distance to the mirror surface, where a perfectly reflecting mirror was assumed. The finite widths of both lasing lines leads to a decay of the SW visibility which is calculated via the local maxima I_{max} and minima I_{min} of the intensity fluctuations: $vis_{SW} = I_{max} - I_{min}/(I_{max} + I_{min})$. The SW visibility, plotted in green into figure 3.2*b*, has decayed from 1 to $1/e \approx 3.7$ within the distance of 5 mm from the mirror, which is in agreement with a longitudinal coherence length of $\Lambda_{coh}^{long} = 1$ cm. A closer look (figure 3.2*b*) reveals a beating of the SW intensity on the 100 μm scale. This is attributed to the presence of the second lasing line and is, practically, not of concern for the interferometer: in a typical experiment, 1 mm of the grating is illuminated by the particle beam, a distance over which the beating averages out.

The beam profile of the grating lasers has a Gaussian shape along both axes and is spread out over an area of roughly $D_x \times D_y = 9 \times 4$ mm with a manufacturer specified divergence of 0.8×1.6 mrad. From this follows a transversal coherence length of $\Lambda_{coh}^{trans} = \lambda R/2\big[D_x \times D_y\big] = 13.0 \times 29.5\,\mu$m, where a distance of $R = 1.5$ m to the mirror surface was assumed and $\lambda = 157.63$ nm. It is reported in [78] that the spectral properties of F_2 excimer lasers are independent from operating conditions such as temperature, gas-filling pressure, high-voltage level and aging of

the system. For the OTIMA this is crucial, as an example illustrates: if 1 mm, or roughly 6000 grating openings, are used for interference, the difference between the grating periods of two standing waves must be significantly smaller than 3 pm, otherwise the phase of the gratings is shifted by π from one end of the illuminated area to the other and no interference can be measured. Since the contrast in OTIMA does not increase with a reduction of the illuminated grating area, we infer temporal stability and equality of the spectral properties of the light emitted by all three grating lasers[3].

Some experimental situations in the OTIMA interferometer require

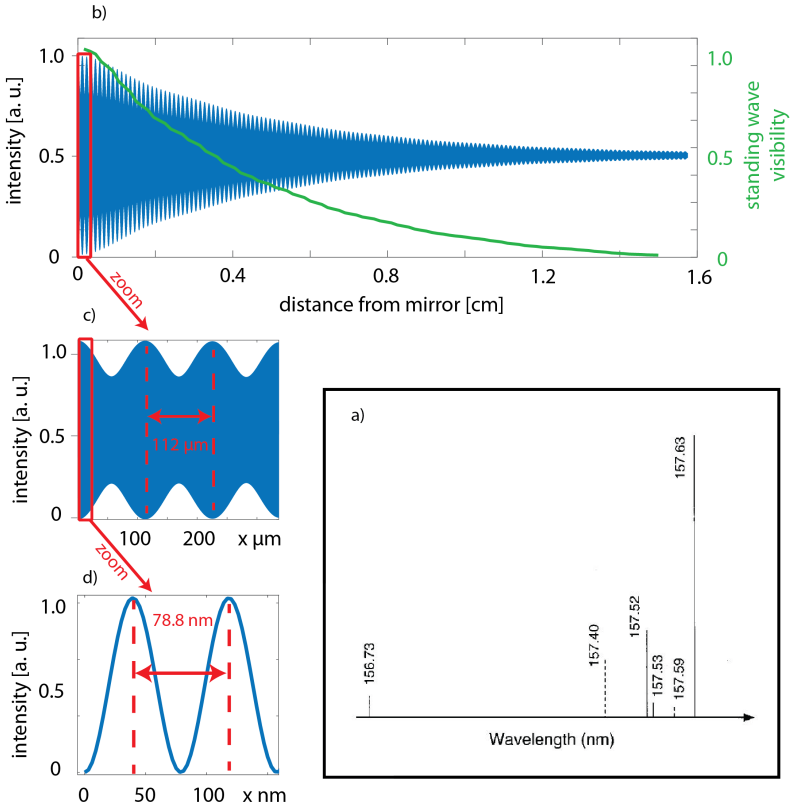

Figure 3.2: *a*) Output spectrum of a fluorine excimer lasers. Figure taken from [78]. *b*) blue graph: Intensity of superposition of standing waves with wavelengths contained in the spectral lines at 157.52 nm and 157.63 nm in *a*). green graph: standing wave visibility as a function of distance from the reflecting mirror surface. Beating with a period of 112 μm is visible in *c*) and the grating period of 78.8 nm in *d*).

precise tunability of the grating power and, ultimately, opening fraction

[3]Note that, nevertheless, the illuminated area of the grating cannot be increased arbitrarily since the visibility of the SW decays with increase of the number if used grating openings. We have found that using 1 mm of the gratings is optimal.

of the gratings (see section4.4 for an example). The pulse energy on the EX50 can be varied by altering the high voltage of the discharge or the filling pressure of the active gas. Both methods don't offer sufficient reproducability and dynamic range. We have thus devised a novel type of attenuator for the grating lasers. This device consists of a machined aluminum cell which is sealed with anti-reflex (AR) coated CaF_2 windows from two opposing sides. The cell may be evacuated up to 1×10^{-4} mbar and simultaneously purged with a well controlled flux of ambient air. The presence of oxygen in the cell will attenuate the laser light as it passes through the cell. When using a photodiode downstream of the absorption cell one can reproducibly set the transmitted laser power ranging from 90 to few percent of the laser power before the cell. This attenuation cell was implanted into the beam line of the center grating laser, the pulse energy of which effects the interference contrast in the most characteristic way of all three gratings (see figure 2.4 for an example). Controllability of the pulse energy is thus most desirable for this laser.

3.2 Calcium fluoride optics

Using 157 nm VUV light for the gratings is beneficial since it allows for a short interferometer and facilitates single-photon ionization gratings for a large range of different particles. However, light with wavelengths below 200 nm is increasingly absorbed by air [79] such that it is necessary to guide the grating beams through an evacuated or nitrogen-purged beam line. There are only a very limited number of materials from which optical elements for 157 nm can be crafted. Mirror coatings can be dielectrical stacks of CaF_2 and MgF_2 or VUV enhanced aluminium coatings. While high reflectance (HR) CaF_2 mirrors are specified to have reflectivities of up to 95 %, aluminium mirrors only reach reflectivities of 80 %. Vacuum windows and lenses for the VUV can only be made from especially pure CaF_2. We have found the 157 nm transmissivity of unused AR coated CaF_2 windows to vary between 70 and 95 %. All CaF_2 elements in the experiment that are surrounded by high vacuum suffer from rapid degradation of the surfaces. This effect is well known [80] and it can be avoided by purging the optics with nitrogen. For this reason the optics chamber is evacuated down to a base pressure of 5×10^{-4} mbar and then flooded with clean nitrogen. The amount of nitrogen flux is adjusted via a fine dosing valve and is typically set to have a pressure of 1 mbar inside the chamber. With this we have not observed degradation of the optics over several years. Since the AR and HR coatings consist of soft materials, the surface contaminations cannot be removed by the common optics cleaning procedures. According to the literature, these contaminations should be removable with ozone or oxygen purging during VUV or UV illumination [81]. Unfortunately, the contaminations in the OTIMA setup seem to resist these cleaning protocols. However, we have succesfully cleaned contaminated optics with in a plasma cleaner. Future improvements will include mounting a plasma cleaning assembly in the main chamber to clean the interferometer mirror without removing it from its mount.

The interferometer mirror is a calcium fluoride (CaF_2) substrate coated dielectrically for high reflectivity at 157 nm. The original batch of mirrors were round with 2 inches in diameter with a specified clear aperture over the entire mirror surface and a ground backside. Reflectivity was specified by the manufacturer to be better than 95 %. Figure 3.3*a* shows an image of a typical surface from the first batch of interferometer mirrors. Here one can see that the surface is flat only up to several tens of nanometers and also that the surface deformations are not cylindrically symmetric. The second batch of mirrors are rectangular and have a length of 7 cm and a width of 4 cm, with a clear aperture of 5×3 cm. An image of the overall much smoother surface can be seen in 3.3b. The backside of these mirrors is clear allowing a fraction of the grating light to be reflected outside the vacuum chamber for monitoring the timing

jitter of the gratings.

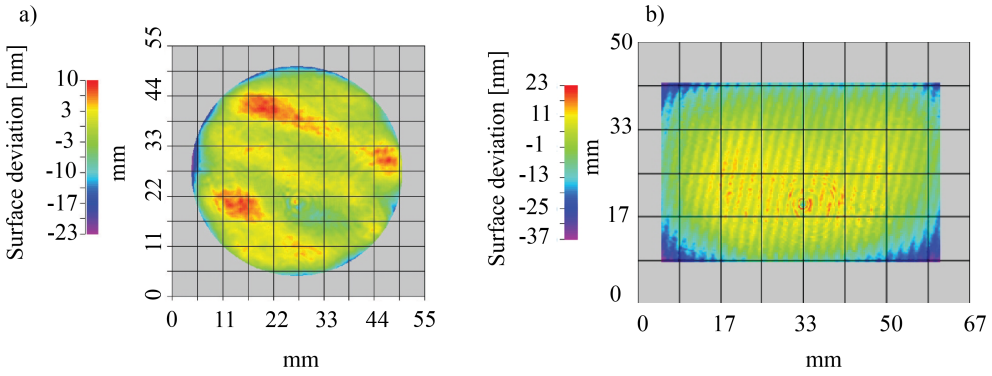

Figure 3.3: Surface profile of a typical interferometer mirror of the *a*) first and *b*) second batch. The fringes in *b*) are an artifact of the imaging method. Images provided by *LASEROPTIK GmbH, Garpsen*

3.3 Time of flight mass spectrometry

Since the interference effects observed in the OTIMA are time and mass dependent, it is important to record particle intensities with nanosecond time resolution as a function of mass. These requirements are met by the ToF-MS implemented in the experiment. This reflectron-type spectrometer from *Kaesdorf Munich* is positioned orthogonal to the particle beam. The combination of the two accelerating stages in Wiley McLaren configuration [82] and the reflectron results in a high mass resolution of $\Delta m/m = 5000$. This means that, with ideal voltage settings, the spectrometer allows to distinguish a peak at 5 000 amu and 5 001 amu, or 100 000 amu and 100 020 amu and so on. The mass resolving power of the spectrometer is thus sufficient to resolve the only weak mass dependence of time domain interference without loss of contrast. Mass calibration must be done for each voltage setting of the spectrometer and is typically exact only up to a few amu, in lack of calibration particles with exactly-known and large mass.

After the ions have passed the drift region inside the spectrometer, they are accelerated onto a three-stage micro-channel plate (MCP). This signal of ions impinging on the MCP contains the arrival time distributions and is fed to a 12 bit digitizer card[4] with 1 ns time resolution and recorded to a computer. Here it is processed with a custom-made software. Each frame is 1 ms long and contains the timing information of the grating lasers via the dedicated photo diode signal. Since the amplitudes of the raw ion peaks coming from the MCP are not proportional to the amount of simultaneous detection events, the number of ions detected during one measurement doesn't follow directly from the integrated signal. Instead, the software determines the standard deviation of the spectrum baseline in a region where no signal peaks are expected and sets the level of a peak height discriminator (PhD) such that only peaks higher than the noise floor are averaged. By comparing the total number of averaged frames with how often the PhD has let a peak pass through, one arrives at the probability P_{zero} of a *zero* event, i.e. of a shot where no ion was detected at a specific time in the ToF spectrum. According to Poissonian statistics, which can be applied since detection events are rare, $P_{zero} = \exp(-\lambda)$, where λ is the average number of ion counts per detection event. M frames thus contain $N = -M \ln(P_{zero})$ particles. From this one obtains a ToF spectrum with a proper particle-count y-axis. All experimental errorbars in this thesis represent 1σ of standard deviation, calculated from N via Gaussian error propagation.

[4] SP Devices ADQ412

3.4 Beam sources for the OTIMA experiment

3.4.1 Source requirements

The pulsed setup and use of absorptive gratings in the OTIMA experiment necessitates a precisely triggerable and bright molecular beam source emitting slow and internally cold particles. While the velocity selection in a time domain interferometer is not necessary in the sense of a deBroglie wave length selection, it must be strong enough such that all detected particles have been subjected to all three gratings. Situations must be prohibited in which particles overtake each other while avoiding one of the grating pulses. Also dependent on the velocity selection is the effective grating thickness in flight direction, for which the tolerable limit is fixed by the curvature of the interferometer mirror surface (see figure 3.3). The width of the velocity distribution is determined by the length of the detector volume in flight direction, the overall flight distance from source to detector and the opening time of the source. Experimentally, the velocity selection can be conveniently adjusted by varying the opening time of the source. Since having an unnecessarily narrow velocity selection is a waste of signal, the opening time of the source is typically increased until the transmission through the gratings increases. This is a sign that no longer all detected particles are subjected to the same grating intensity and that an upper bound to the opening time is reached.
In the current setup the distance between the centers of two adjacent gratings is around $s_g = 2\,\mathrm{cm}$. As a rule of thumb it holds that the particle velocity must be low enough for the particles to fly approximately this distance within their Talbot time. The upper bound on the velocity is thus

$$v_{max} = \frac{s_g h}{d^2 m}, \tag{3.1}$$

where h is Plank's constant, m the particles mass and d the grating period. In figure 3.4 the constraint on the particles velocity imposed by this rule is compared to thermal velocities at 500 K. As illustrated in the graph, thermal beams at this temperature are slow enough for experiments with masses up to $1,7 \times 10^5\,\mathrm{amu}$. For larger masses additional cooling will be necessary. This could be done with a cryogenic buffer gas cell, optically in a cavity [83] or, for charged particles, with ion guiding and slowing [84].

3.4.2 Even Lavie valve

For initial proof of principle interference experiments in the OTIMA interferometer an Even Lavie (EL) valve [77] was attached to the setup,

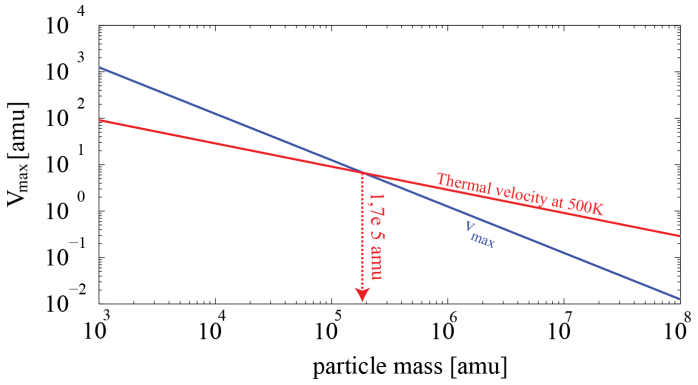

Figure 3.4: The constraint imposed on the particle velocity by v_{max} (see 3.1) is compared to the mass dependence of the thermal velocity at 500 K particle temperature.

for experiments with beams of clusters of organic molecules, such as anthracene (Ac) or ferrocene (Fc). With its pulsed working principle, the source is a perfect match for the OTIMA setup, avoiding the need to use a beam chopper. Also, the source assembly worked reliably and produced stable and intense beams over long periods of time and the broad mass distributions emitted by the valve allowed to observe the characteristic mass dependence of time domain Talbot Lau interference. The source works as follows: molecules are heated and evaporated inside a metal tube at the center of the valve. The molecular vapor is then expanded into the vacuum for a duration of up to 30 μs together with a noble gas. The molecules aggregate to clusters, while the excess binding energy is transfered via collisions to the coexpanding seed gas. With this procedure we have routinely obtained beams with clusters consisting typically of up to 15 monomers. The velocity distribution of the emitted particles is determined by the atomic mass and pressure of the noble seed gas used for the expansion. We have found the most probable particle speeds to lie around 700 m/s for an argon seeded beam and 900 m/s for a neon seeded beam, largely independent on the mass of the evaporated molecules. Although we have successfully generated clusters with masses of up to 12000 amu with the source, these were too fast to be used in the current OTIMA setup. The source can be used in the current OTIMA setup for particles with masses up to 4000 amu.

3.4.3 Laser heating source

The laser heating source was implemented to facilitate experiments with tailor-made macromolecules and calibration molecules such as TPP. The working principle of a continuous-beam version of this source was first demonstrated in the context of far-field diffraction at a single grating [85]. The source assembly consists of only very few parts: a sample holder to which two metal rails are attached and two motorized linear vacuum feedthoughs with rectangular neodymium magnets attached to the ends. As the motorized manipulators are mounted to two adjoining sides of a cubic vacuum chamber and the magnets slide in the rails on the sample holder, the sample can be manipulated automatically inside the vacuum (see figure 3.5). The molecules are coated onto either a glass or metal slide which attaches to the sample holder. The desorption laser, which can be a pulsed nanosecond laser or a chopped continuous-beam laser, is focused onto the sample plate. Motorized x and y-stages can scan the sample surface with respect to the laser spot where the molecules are evaporated. The signal is optimized by adjusting the scanning speed, the thickness of the molecular layer on the sample plate, the laser power and wavelength. The homogeneity of the molecular layer thickness is crucial for stability of the signal.

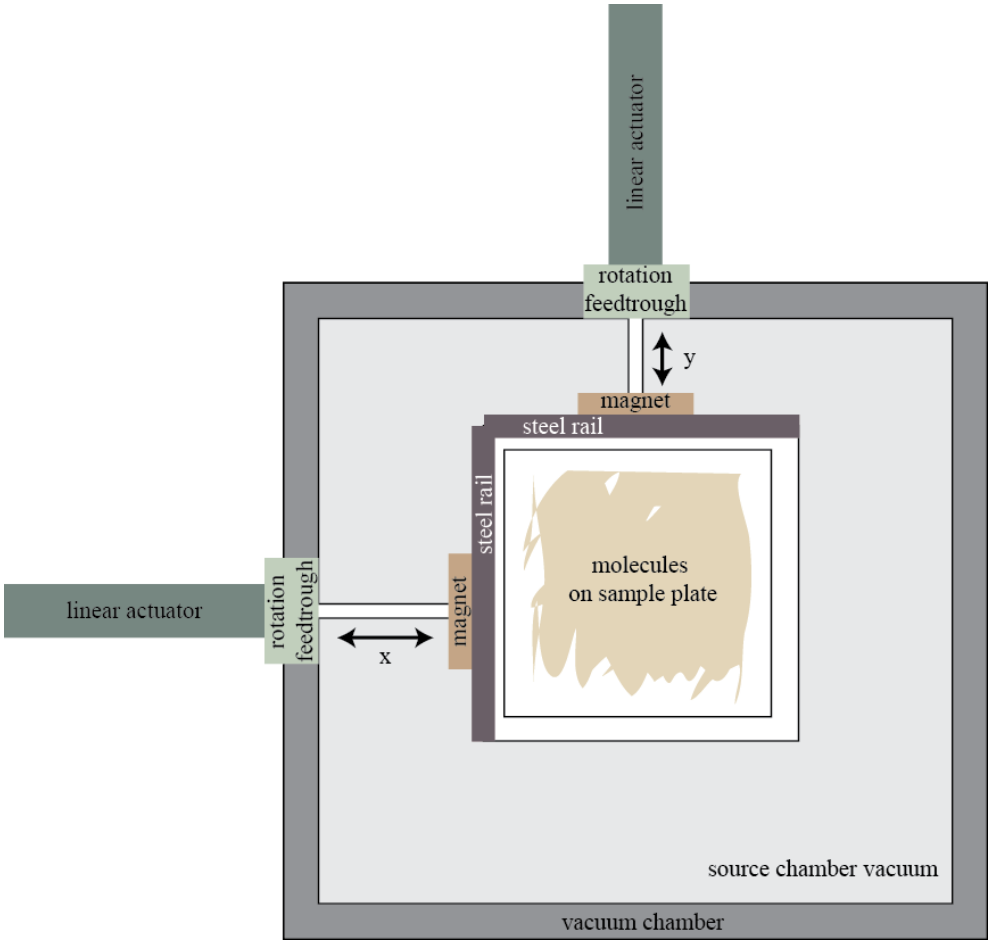

Figure 3.5: Drawing of the laser heating source. The molecular sample is applied to a sample plate, which is fixed to a sample holder. Steel rails are attached to adjoining sides of this square frame. Inside the source vacuum chamber, the x and y position of the sample is controlled with linear actuators. These dock to the sample holder via magnets, which slide in the steel rails.

Chapter 4

Results

Since the OTIMA is a one-of-a-kind interferometer, many experimental methods have been developed from scratch in order to operate the machine. This section will cover the most important techniques and experimental results.

4.1 Experimental protocol

A single experiment from beginning to end typically takes several milliseconds. This cycle is repeated at a frequency of 100 Hz. The sequence starts with triggering the source to emit a pulse of particles which passes aerodynamic beam skimmers in a differential pumping stage and enters the main chamber. Here the beam is collimated with horizontal and vertical collimators. The particles then fly in close vicinity, usually in a distance between 0.1 mm and 1.1 mm, along the mirror surface while being subjected to the three subsequent 157 nm VUV laser pulses. Particles that survive the grating sequence without depletion from the beam fly into the ion-extraction region of the ToF-MS. Here they are again illuminated by a 10 ns pulse of 157 nm light and are photoionized. The spot size of this ionization laser is chosen such that only a fraction of the traversing particles is ionized and later detected, namely those who have been struck by all three gratings and inside a volume small enough as not to average over too much of the mirror surface. The size of this volume in flight direction is the effective overall grating thickness. Following the ionization in the ion source region of the spectrometer, the repeller and extractor electrodes are triggered with a delay of about 10 μs with respect to the ionization laser[1], accelerating the particles in a 90° angle upwards into the drift tube of the mass spectrometer. Finally, the

[1]This order was chosen since the ionization laser has a significant trigger-to-emission jitter of up to 25 ns FWHM which would reflect in a loss of time resolution in the mass spectra if the ions were extracted from the repeller region immediately after being formed.

signal from the MCP is recorded by a fast digitizer card and send to a computer for analysis. Since the grating lasers have a trigger-to-emission jitter of up to 10 ns FWHM, the actual emission time of each grating is measured with a biased GaP photodiode each time the laser is triggered. The three photodiode signals are fed to the digitizer in real time, just before the ToF spectrum is recorded, such that each frame sent to the computer contains the spectrum and the respective timing information. This allows post selection of those frames during which the lasers had accurate timing.

Directly recording the interference pattern in the OTIMA setup is not as straight forward as it is in a non-time domain setup such as the KDTLI [57] where the first and last gratings are nano fabricated silicon nitride structures. In this experiment the pattern is measured by recoding the transmission through the three gratings as a function of the position of the third grating, which is scanned parallel to the grating vector. In contrast to that, all three gratings in the OTIMA setup are formed at the same mirror surface and the gratings cannot be easily scanned in space. We can, however, exploit time-like resonances and the mass spectrum to extract the interference fringe visibility. The Talbot Lau effect in the time domain is very sensitive to the temporal symmetry of the grating sequence ans asymmetric delays will make the contrast disappear. During a measurement we thus toggle between two modes: firstly, a symmetric mode, in which the delays are equal up to one or two nanoseconds. This is the mode in which contrast is expected to appear. Secondly, an asymmetric mode, where the delays are detuned from symmetry by δT (see definition (2.17)), usually several tens of nanoseconds. The interference will be visible as an intensity difference between the spectra recorded in each mode[2].

A quantitative measure, S_N, for the visibility is obtained when the signal difference is normalized with the signal in the asymmetric mode:

$$S_N = \frac{S_{int} - S_{avg}}{S_{avg}}, \tag{4.1}$$

where S_{int} and S_{avg} is the signal recorded in the symmetric and asymmetric mode, respectively. How equal (unequal) the delays in the symmetric (asymmetric) mode must be, depends on the vertical collimation of the particle beam: when two particle trajectories[3] enclose an angle α in the

[2]Since not all beam sources offer long term signal stability, the experiment usually alternates between the symmetric and the asymmetric modes from shot to shot. This averages out all signal instabilities, with the exception of strongly periodic shot-to-shot intensity fluctuations. These can be detected by swapping the operating mode only every two shots, for example.

[3]Using the trajectory picture in the description of a matter-wave interferometer may seem problematic. The angles in this section, however, are typically three or-

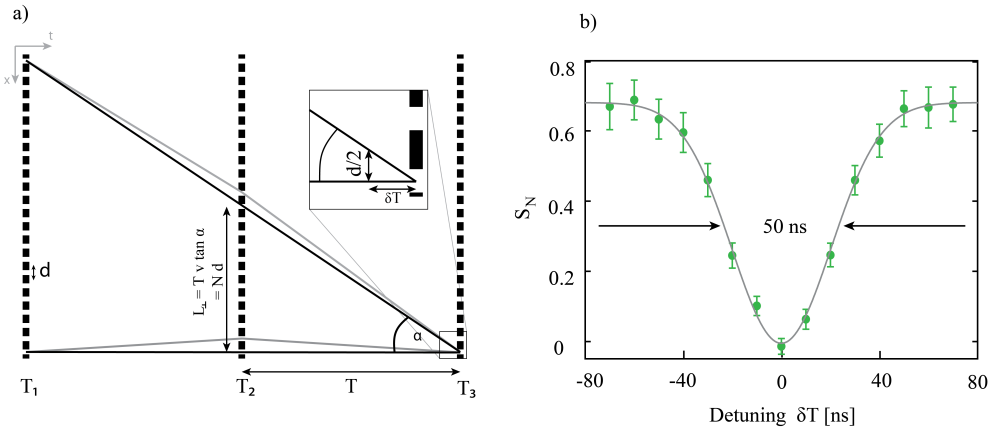

Figure 4.1: *a*) A sketch to illustrate the requirements for timing precision in a three grating interferometer. In this semi-classical picture, the two trapezes correspond to the trajectories of two interfering particles. They contribute to two shifted interference patterns if probed by the third grating too early or too late with respect to the symmetric timing T_3. *b*) Normalized signal S_N of a 7-fold anthracene cluster versus δT. A Gaussian (grey line) was fitted to the data (green points). Versions of both figures are published in [68] and [3].

interferometer (see figure 4.1*a*), they will contribute to shifted interference patterns if they are probed by the third grating too early or too late with respect to symmetric timing. For a given grating asymmetry, the shift is determined by the distribution of transversal velocities, i.e. velocity components parallel to the grating vector, in the particle beam and hence depends on the beam collimation and the total time of flight from source to detector.

It is straight-forward to experimentally identify the necessary amount of asymmetry: S_N is measured for different detunings δT in the asymmetric mode, as illustrated in figure 4.1*b*. As δT is scanned from negative to positive, S_N reaches a minimum when the timing is identical in both modes [4]. Figure 4.1*b* shows data of an anthracene cluster experiment, where the particle beam collimation of $\alpha = 2\,\mathrm{mrad}$ and a maximal transversal particle velocity of $v_{trans}^{max} = 1,8\,\mathrm{m/s}$ amounted to a FWHMt of around 50 ns. For this particular experiment the contrast reached its highest value of nearly 70 % for $\delta T > 30\,\mathrm{ns}$ (or $\delta T < -30\,\mathrm{ns}$). The data is well fitted by an inverted Gaussian, indicating the Gaussian shape of

ders of magnitude larger than the diffraction angles imposed by the gratings. The semiclassical picture can thus safely be employed.

[4] This is also a convenient way to check for systematic errors: when the minimum is reached not at $\delta T = 0$ but before or after, this is a sign that there is an offset in the timing measurement of one of the grating lasers, for example due to a mismatch in cable length to one of the photo diodes.

the transversal momentum distribution.

4.2 Interference of Van der Waals clusters

Molecular beams with a wide mass distribution are beneficial for OTIMA interferometry for several reasons: they facilitate the observation of the signature mass dependence of the Talbot Lau effect in the time domain which allows to distinguish interference from shadowing or other systematic effects. Conveniently, non-interfering particles are measured simultaneously with the interfering ones, serving as references. Also, the mass dependence of coherence loss may be investigated in a single experiment without changing the interferometer timing or source properties. The data presented in this section is published in [3].

Figure 4.3 shows an anthracene cluster mass spectrum, recorded in the resonant (red data) and off resonant mode (black data) and magnified locally for better graphical representation. The clusters were generated in a jet of argon and accelerated to a mean velocity of around $v = 620\,\mathrm{m/s}$ (see section 3.4.2). The laser power of the gratings was adjusted such that larger clusters are transmitted with a probability between 20 - 30 %, as shown in figure 4.2. The pulse separation time was set to $\Delta T = 25.9\,\mu\mathrm{s}$, which corresponds to the Talbot time of the mass $m = 1726\,\mathrm{amu}$. The intensity difference between the red and black spectra are attributed to constructive interference. The green bars in the upper panels display the normalized signal S_N which was computed for each cluster according to equation 4.1, where S_{int} and S_{avg} were obtained by integrating over the cluster peaks. The highest contrast within the first Talbot order was reached for the 10-fold cluster with a mass of 1784 amu showing over 80 % of contrast. The contrast maximum can be shifted to smaller masses by reducing ΔT. This behavior is evident in figure 4.4. Here, neon was used as a seed gas, creating clusters with a mean velocity of $v = 930\,\mathrm{m/s}$. This allowed us to set the grating delay to $\Delta T = 18.9\,\mu\mathrm{s}$, which corresponds to the Talbot time of the mass $m = 1260\,\mathrm{amu}$. The laser intensity was adjusted to achieve a cluster transmission of 20 - 30 % and the highest contrast was measured for the 7-fold cluster with a mass of 1248 amu. Both the argon and the neon experiments have also revealed second order Talbot interference as contrast maxima at half the mass of the first Talbot order.

The theoretically predicted S_N is a function of the grating power and pulse delay. On the other hand, it also depends on the optical particle properties at the grating wavelength, specifically the depletion cross section σ_{157}^{dep} and the optical polarizability α_{157}. Depletion includes any process that renders the particles undetectable to the mass spectrometer. For the anthracene monomer we find the statical polarizability

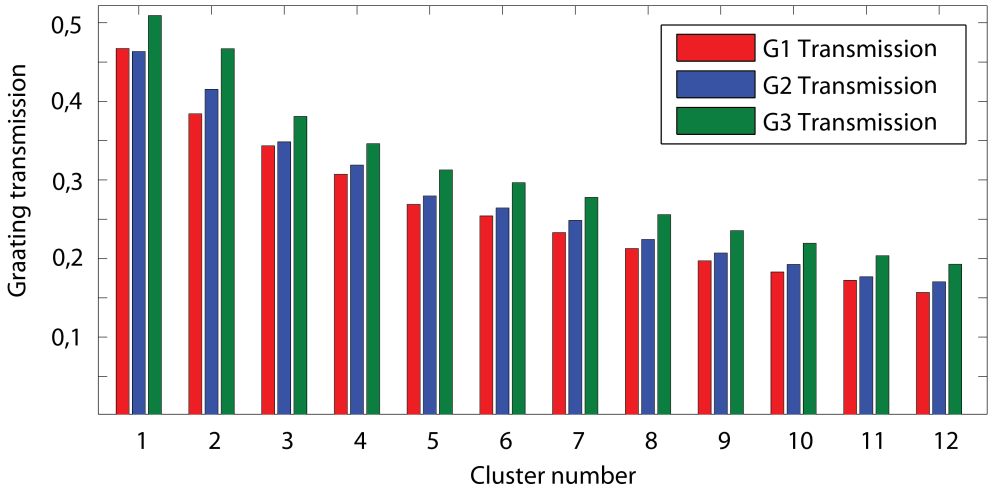

Figure 4.2: Transmission of anthracene clusters through the first (panel a), second (panel b) and third grating (c). The laser power of the grating lasers was adjusted such that 20 - 30 % of clusters with masses around the first Talbot order are transmitted through each grating. The fact that the depletion probability rises with cluster size is evident in the decrease of transmission with climbing cluster number

$\alpha_{stat} = 25.4 \times 10^{-30}\,\mathrm{m}^3$ [86] and assume $\alpha_{stat} = \alpha_{157}$ due to the off-resonant interaction between the light field and the particles. For the monomer we extracted the ionization cross section $\sigma_{157}^{ion} = 1.1 \times 10^{-20}\,\mathrm{m}^2$ from [87]. The ionization energy of anthracene is 7.4 eV [88] and lies well below grating photon energy of 7.9 eV [89] and we assume that it does not change for the clusters. This is justified since no electrons are exchanged between the molecules within van der Waals clusters. We also assume that the quantum yield of single-photon ionization is close to unity ($\sigma_{157}^{dep} = \sigma_{157}^{ion}$). Since neither σ_{157}^{dep} nor α_{157} are known for the clusters we assume that they exhibit the scaling behavior of the cluster transmission through the gratings. The predicted values for S_N are plotted as purple bars in figures 4.3 and 4.4. The uncertainty of the predictions is marked in a lighter shade of purple at the top of each bar and captures the assumption that the polarizability is known up to $\pm 30\,\%$. The impact of the polarizability is stronger for clusters with masses larger than the mass for which the ΔT is the Talbot time. This meets the expectations, since the phase grating effect is weakest directly on TL resonance. While the mass dependence of the expected contrast fits well to the data, there is a discrepancy between the data and the predictions in terms of the absolute S_N values. This can be attributed to the uncertainty in the current knowledge about the VUV properties of such clusters.

Were the contrast only a consequence of classical shadowing and lensing [45], one would expect the mass dependence plotted as grey bars. The

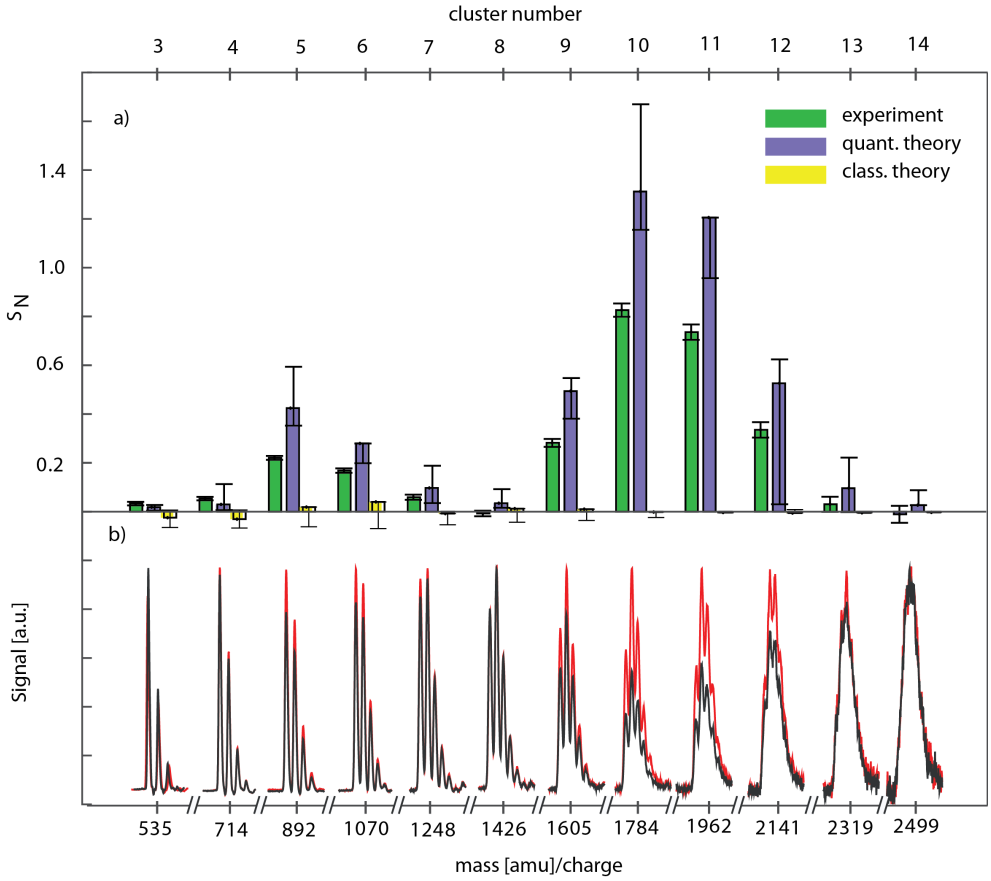

Figure 4.3: The lower panels show mass spectra of anthracene clusters expanded in an argon jet. The red spectra were recorded in the resonant mode and the spectra in black were measured in the off-resonant mode. The normalized signal S_N was calculated from the data and is presented in green bars in the upper panels. The theoretical expectation is shown as purple bars.

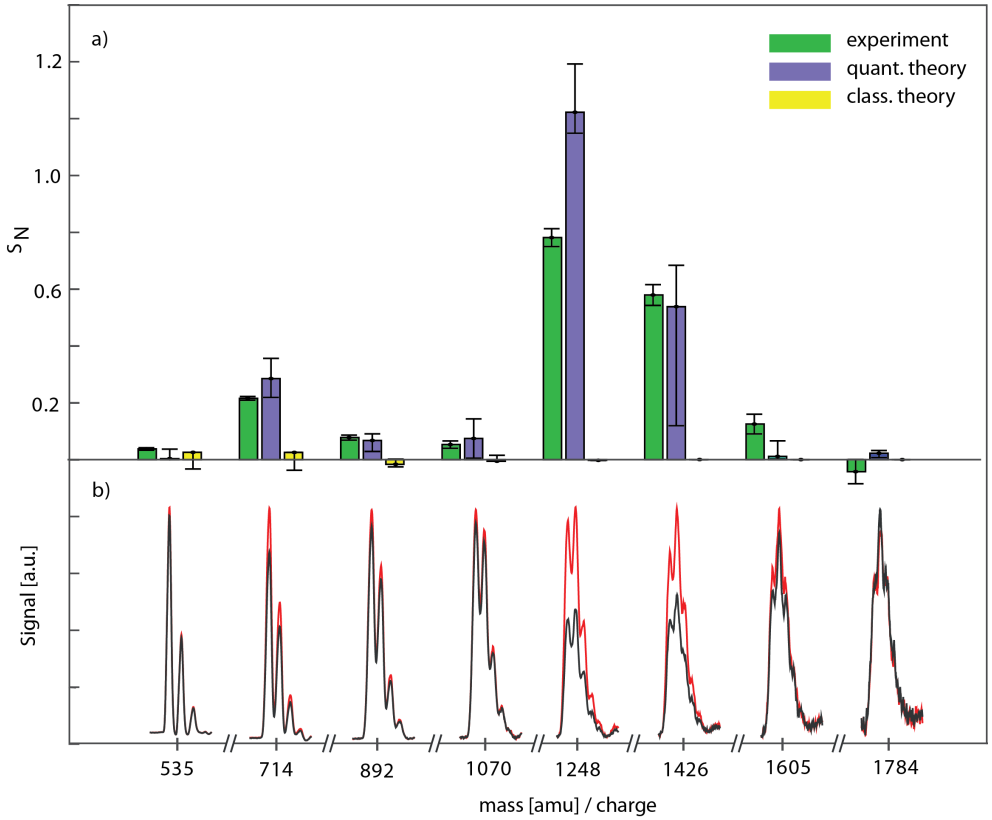

Figure 4.4: Same as figure 4.3, however, here neon was used as seed gas. The mean cluster velocity was $v = 930\,\mathrm{m/s}$, which shifts the TL resonance to smaller masses.

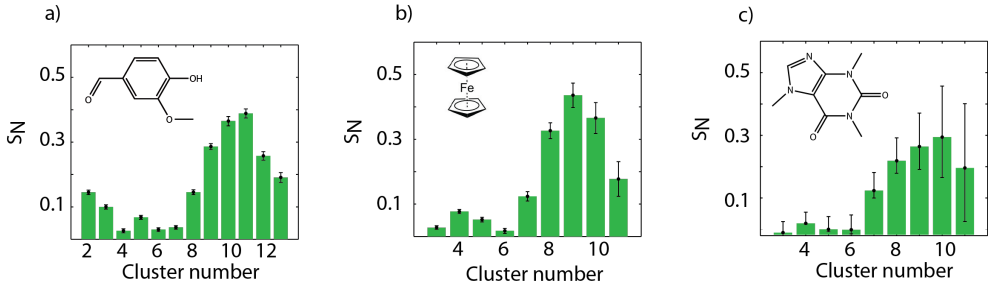

Figure 4.5: Normalized contrast measured with clusters of vanillin (m = 152 amu), ferrocene (m = 186 amu) and caffein (m = 194 amu), from left to right. The data reveals first Talbot order interference for clusters of all three molecules, demonstrating the universality of the method.

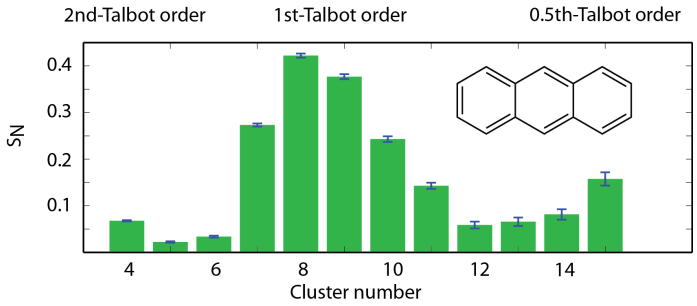

Figure 4.6: Normalized signal of anthracene clusters measured with a pulse delay of $\Delta T = 19\,\mu$s. The first, second and half order effect could be observed in this experiment.

strong deviation between the data and the grey bars allows us to confidently identify the contrast as interference.

For the sake of demonstrating the universality of the OTIMA method interference experiments have been conducted with a variety of different clusters from molecular vanillin, ferrocene and caffeine. The results are presented in figure 4.5. The normalized signal S_N shows the mass dependence expected of first order Talbot Lau interference.

The quantum mechanical origin of the contrast in OTIMA interferometry is evidenced by the the mass dependence of the normalized signal. However, as described in section 2.3, the observation of the $d/2$-periodic fractional-order interference pattern is even stronger proof.

The first step towards observing the fractional Talbot effect was taken by an experiment with anthracene clusters, the results of which are displayed in figure 4.6. For this experiment, the pulse separation was set to $\Delta T = 18.7\,\mu$s placing the first Talbot order around the 8-fold cluster. The EL valve was adjusted such that the source produced signal up to the 15-fold cluster. The depletion efficiency in the gratings varies between the clusters interfering in the different orders: A laser energy

that allows sufficient depletion of the small clusters will strongly diminish the signal of the large clusters. Still, contrast could be observed for the half, first and second Talbot order. Since the fractional order contrast depends less steeply on the grating power than for the integer order effect, the contrast is smaller for the fractional effect at fixed grating power. While resonances in the mass dependence fit well with our expectations, the demonstration of the $d/2$-periodicity of a fractional Talbot order interference pattern is an pending goal for OTIMA interferometry. The fractional Talbot order provides even stronger proof for quantum interference than the first order peak. Additionally, for any given beam velocity, it allows doubling the mass range of particles for which the quantum predictions differ clearly from any classical prediction.

4.3 Measuring spatial interference patterns

It is convenient to extract the visibility from S_{int} and S_{avg}, because it can in principle be done in only two experimental shots, without the need to resolve a sine-shaped signal. For this practical reason it has become the common way to operate the OTIMA interferometer. There are, however, methods to map out the spatial interference pattern. One of them is based on the same type of experiment performed for recording a dip like depicted in figure 4.1. The concept is illustrated in figure 4.7*a*. When the particle beam (in the figure enclosed in red lines) is not normal to the grating k-vector, the fringe pattern acquires a velocity component v_{trans} parallel to the gratings. The fringe position relative to the third grating is then time dependent and can be scanned by shifting the third grating in time around the resonance. A fringe pattern becomes visible if the divergence angle α of the particle beam is smaller than the angle γ at which the beam is tilted with respect to the normal vector of the gratings. Figure 4.7*b* shows S_N as function of δT, i.e. the time by which G_3 is detuned from symmetry. The scan of δT reveals the spatial fringes of the interference pattern, which are enveloped by the resonance dip associated with the divergence α (see figure 4.1). By fitting a sine-modulated Gaussian function to the data, both the fringe spacing as well as the width of the resonance dip can be extracted. From this we arrive at $\alpha = 1.1\,\text{mrad}$ and $\gamma = 3.5\,\text{mrad}$, which is in good agreement with the experimental beam parameters. This method works reliably but it requires stronger collimation of the particle beam than is necessary for interferometry with $\gamma = 0$. Note that the angle γ cannot be increased arbitrarily since particles average over increasingly large fractions of the grating structure, thus reducing the transmission through the gratings.

An alternative method of spatially resolving the interference pattern relies on slightly modifying the period d of one of the gratings, here the

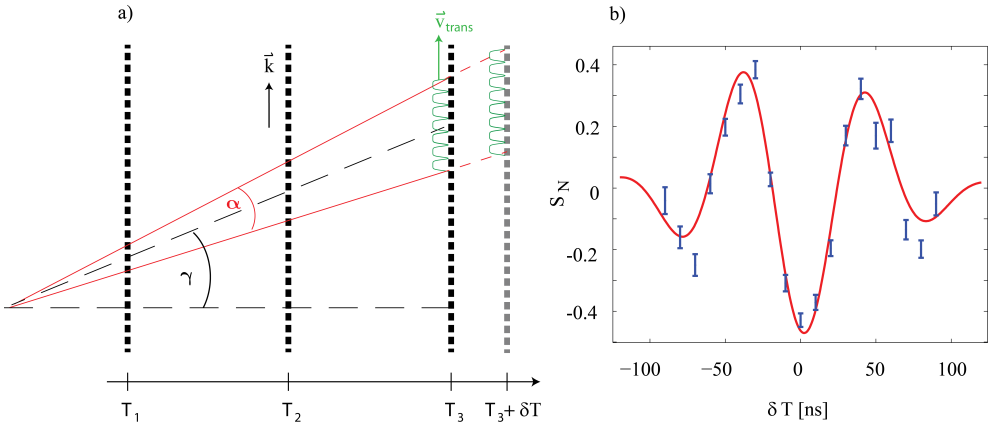

Figure 4.7: *a*) The area between the red lines represents a particle beam with divergence α, entering the interferometer at angle γ. The interference pattern (shown in green) acquires a transversal velocity $\vec{v}_{trans}$ parallel to the grating vector $\vec{k}$ and for $\gamma > \alpha$, the fringe position can be scanned by temporally shifting G_3. *b*) S_N of TPP molecules as a function of the detuning δT, revealing the interference pattern (blue data points). A sine function enveloped with a gaussian is fitted to the data (red graph).

most influential G_2. The output spectrum of the excimer lasers is determined by resonances in the active gas and cannot be altered. Changes in d of one of the gratings can, however, be induced by increasing the angle β at which the beam is incident on the interferometer mirror and enlarging the separation between the mirror and the molecular beam. This is illustrated in figure 4.8. The period change is $\Delta d = d \cos \beta$. When the distance between the particle beam and the mirror surface is increased, the phase of the angled grating will change with respect to G_1 and G_2[5] Results of such an experiment can be seen in figure 4.8. Here we set $\beta = 5\,\text{mrad}$ for G_2. Each panel shows S_N as a function of mirror height for a different cluster of anthracene. Periodic oscillations of S_N appear for clusters with Talbot times close to the fixed pulse separation time of $\Delta T = 25\,\mu\text{s}$. The damping of the oscillations at large mirror heights is attributed to the limited longitudinal and transversal coherence lengths (on the order of 1 cm and 50 μm, respectively) of the gratings laser beam. Also, S_N is slightly reduced even for small mirror heights because of grating-phase averaging over the particle beam height.

To wrap up this list of fringe scanning techniques I will review one, which comes closest to the common practice in space domain interferometers such as the KDTLI. Liquid graphite spray is applied to the backside of the

[5]Note that the grating vectors are always orthogonal to the mirror surface and thus stay parallel even when the angles of incidence are different for each grating.

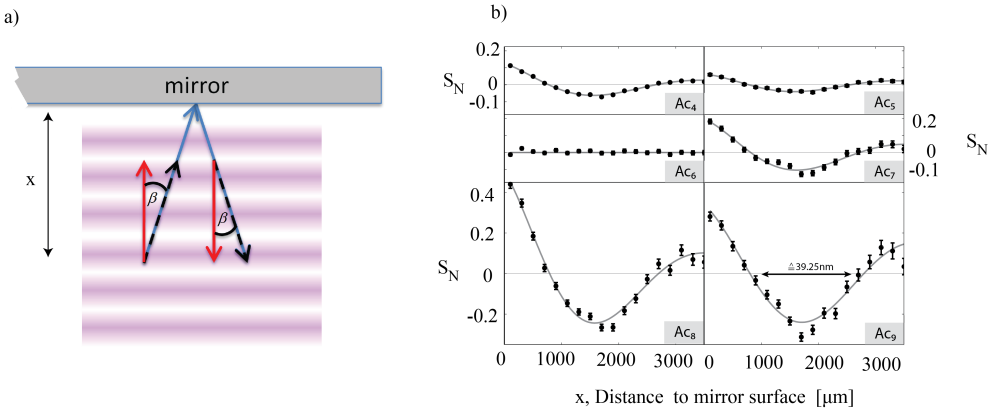

Figure 4.8: *a*) Aligning the grating lasers with an angle β to the surface of the interferometer mirror, leads superposition of wave vectors (red arrows) that are shorter compared to the free running wave vectors (black dashed arrows). This results in an optical grating with larger grating period. *b*) Measurement of S_N for various clusters of anthracene as a function of the beam-mirror distance x. Here, the center grating hit the mirror surface at $\beta = 3\,\text{mrad}$, such that a variation of the mirror height effectively scanned the fringe phase. This figure was previously published in [68]

interferometer mirror over an area that is illuminated only by the center grating. When the graphite spot is heated with a 1.5 W laser diode, the mirror expands thermally and G_2 is shifted. Since it is difficult to keep the local mirror temperature stable, interference measurements were performed during the heating (expansion) and cooling (contraction). The data is presented in figure 4.9. The panels shows the intensity of one anthracene cluster as a function of heating time (cooling time) after the heating laser is switched on (off). The data points show the signal averaged over 3 s. Since contraction and expansion of the mirror substrate follow an exponential decay, the oscillations are fastest at the beginning of each process. Only those clusters show the oscillations for which ΔT was suitable for interference.

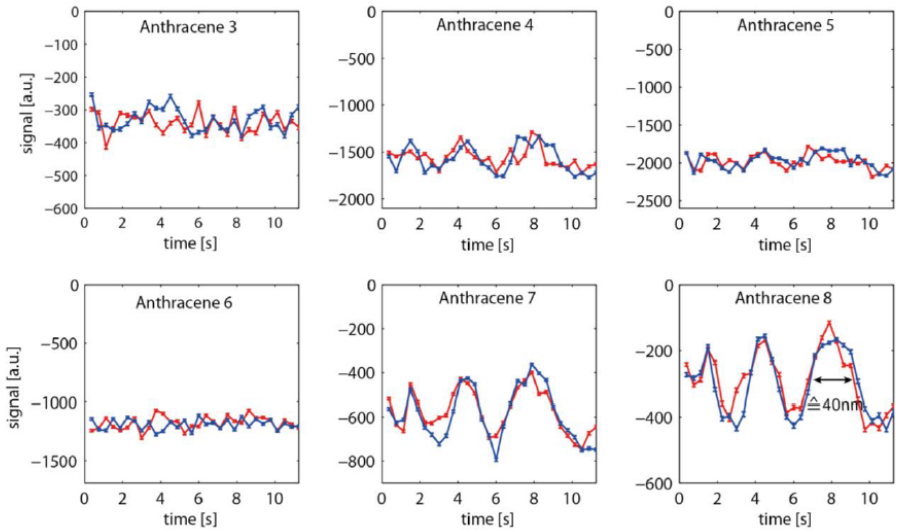

Figure 4.9: Here we scanned the fringes in real space by locally heating the interferometer mirror, as explained in the text. Figure taken from [90].

4.4 Refining the OTIMA model

If quanutm theory had to be modified for high-mass objects, this would show up as a difference between the measured interference visibility and the theoretical predictions. Such a comparison requires precise knowledge of all decoherence mechanisms as well as a strong handle on systematic effects. The role of decoherence has been discussed in section2.2 as well as in [2]. Here, the model of the OTIMA interferometer as presented in 2.1 is refined by taking into account experimental imperfections such as finite mirror quality and grating laser coherence. The results presented here are published in [5].

Theoretically, the contrast of an OTIMA experiment, can always reach unity for particles with a given mass, since optical gratings offer tunability of the opening fraction via a variation of the grating laser power[6]. Often, however, 100 % contrast is not necessary and the laser power can be reduced for higher signal throughput.

Finding out if the experimental results live up to the theoretical expectations requires a good understanding of the gratings, fully characterized both in position, visibility and strength. The quality and geometry of the mirror surface must therefore be taken into account as well as alignment and coherence of the grating laser beams.

The normalized signal measured in OTIMA as described in section4.2 shall be related to the predicted contrast $\mathcal{V}$ via

$$S_N = \Lambda\,\mathcal{V}. \tag{4.2}$$

where Λ incorporates visibility reduction due to imperfections in the experimental setup as well as the fringe phase Δx (see definition (2.12)), i.e. the relative phase between the fringe pattern and the third grating. For a perfectly flat mirror surface and gratings with identical periodicity, the fringe phase would always amount to zero, and the intensity maxima of the interference pattern would be perfectly aligned with the openings of the third grating. Unfortunately, CaF_2 mirrors cannot be polished to be flat by less than several tens of nanometers over an aperture of several centimeters (see section 3.2 for details).

The experiments in this section were all recorded with $\Delta x \approx d/2$ and $-1 \leq \Lambda \leq 0$. As exaggeratedly illustrated in figure 4.10 the deformation of the mirror surface has two implications: on the one hand the over-all curvature shifts the gratings with respect to each other, thus introducing a non-zero fringe phase. On the other hand, the roughness of the mirror surface creates shifted gratings within one grating pulse. This leads to the formation of differently shifted interference patterns depending on

[6]This is in contrast to space domain interferometers with material gratings, where the highest achievable contrast is often limited to well below 100 % due to the fixed opening ratio of the gratings [57]

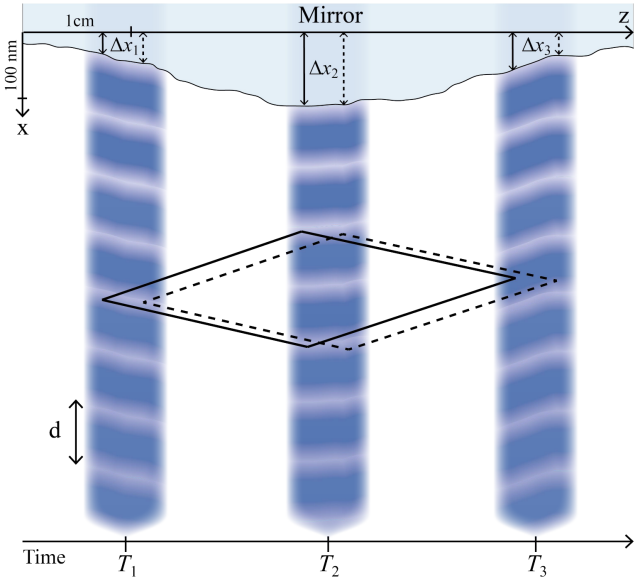

Figure 4.10: The curvature of the interferometer mirror surface diplaces the gratings and creates a dependence of the interference fringe shift on the location of the particles in the grating pulses. If Δx_i is constant over the effective grating depth in fligh direction then the fringe pattern has full contrast and is merely shifted with respect to the third grating. If Δx_i changes across the grating depth the final interference pattern will be an average of shifted patterns resulting in reduced overall visibility. Figure taken from [5].

where a particle was located when the grating was triggered (see figure 4.10, where the effect is illustrated with the use of semi-classical paths).

Now follows a characterization of the standing wave gratings. The intensity of a perfect optical standing wave is given by

$$I_{ideal}(x) = 4I_0 \cos^2(2\pi x/\lambda), \tag{4.3}$$

where I_0 is the intensity of the laser beam hitting the mirror, λ is the laser's wavelength and x is the position along the grating vector. In the experiment, limited mirror quality and finite laser coherence must be taken into account, both of which reduce the visibility of the standing wave. Let R (with $0 \leq R \leq 1$) be the reflectivity of the mirror surface. Then

$$I_{trans}(x) = I_0(1 - R) \tag{4.4}$$

is the amount of intensity that is transmitted through the mirror surface. Due to finite coherence of the lasers, some amount of the reflected

light will form an incoherent superposition of running light waves with the intensity

$$I_{inc}(x) = RI_0(1 - C), \tag{4.5}$$

where C (with $0 \leq C \leq 1$) is a measure for the spatial coherence of the laser beam. The total intensity in the standing wave thus reads:

$$I(x) = \left[4RC\cos^2\left(\frac{2\pi x}{\lambda}\right) + R(1 - C) + (1 - R)\right] I_0. \tag{4.6}$$

At each position x in the grating pulse of duration t_λ, a particle with the absorption crosssection σ_λ at the laser wavelength λ absorbs at average

$$n(x) = I(x)\frac{2\pi\lambda\sigma t_\lambda}{\hbar c} \tag{4.7}$$

photons. The probability of not absorbing a photon at position x in the grating is equal to the transmission probability, which reads, under the assumption of possonian statistics: $\mathcal{T}(x) = \exp(-n(x))$. Integrating this expression over one grating period gives the total grating transmission:

$$\begin{aligned}
\mathcal{T} &= \int_0^{\lambda/2} \exp(-n(x))\,\mathrm{d}x \\
&= \int_0^{\lambda/2} \exp\left(-\frac{2\pi\lambda\sigma_\lambda t_\lambda}{\hbar c} I(x)\right)\,\mathrm{d}x \\
&= J_0\left(i\frac{n_0}{2}\right)\exp\left(-n_0\left(\frac{1}{4RC} + \frac{1}{4C}\right)\right) \\
&= J_0\left(i\frac{n_0}{2}\right)\exp\left(-\frac{n_0}{2K})\right),
\end{aligned} \tag{4.8}$$

where

$$n_0 = \frac{8\pi\lambda\sigma_\lambda t_\lambda RC}{\hbar c} \tag{4.9}$$

and

$$K = \frac{2RC}{(1 + R)} \tag{4.10}$$

were introduced. The difference between the amount of photons absorbed in a node and antinode of the grating is n_0 and K is a measure for the quality of the standing wave, i.e. its visibility. For known σ_λ and I_0, the visibility of the standing waves can be extracted from fitting the power dependence of the transmission with equation (2.10). Typically,

however, neither σ_λ nor the laser power are known with sufficient accuracy. This means that n_0, which is a measure for the grating strength and thus an important parameter for estimating the expected matter-wave interference visibility, cannot be extracted from a measurement of the particle transmission alone. Still, the standing wave visibility and n_0 can be determined by measuring the power dependence of the interference contrast for different cluster masses. For this, a characteristic feature of Talbot Lau interference is exploited, namely the absence of the phase grating effect when $\Delta T = T_T$. The contrast will then only depend on n_0, independent of the particles polarizability (see section 2.1 for details).

We measured the normalized signal and grating transmissions for anthracene clusters as described in section4.2, for different G_2-laser powers. The absorption cell described in section3.1 served as a variable attenuator for the G_2 laser beam. The pulse delay of the gratings was set to $\Delta T = 16.65\mu s$, corresponding to the Talbot time of the 6-fold cluster, for which n_0 fully determines the expected contrast. Starting with an educated guess of $\Lambda = \Lambda_{start}$ we calculate for each G_2-power the n_0 for which $S_N(Ac_6) = \Lambda_{start}\mathcal{V}(Ac_6, n_0)$, where $\mathcal{V}(Ac_i, n_0)$ is the theoretically predicted contrast for the i-fold anthracene cluster. Together with the measured transmission $\mathcal{T}(Ac_6)$, the resulting n_0 is then inserted into equation (2.10). This yields a value K_{start} for the standing wave visibility, which we assume to be the same for all three gratings[7]. K_{start} is then used to calculate, again via equation (2.10), the n_0 for all other clusters and their scaled VUV absorption-to-polarizability ratios β follow from $S_N(Ac_i) = \Lambda_{start}\mathcal{V}(Ac_i, n_0, \beta)$. This procedure is repeated for various values of Λ to minimize a least squares fit of the data $S_N(Ac_i)$. The experiment and fitting routine were carried out three times: with anthracene clusters for a mirror height of 1 mm and 2 mm as well as with ferrocene clusters at a mirror height of 1 mm. The results of these experiments are shown in figure 4.11. The normalized contrast of the 6-fold clusters steadily increases with laser power, as one would expect for purely absorptive gratings. In contrast to that, the measured S_N of all larger clusters declines after a maximum is reached, due to the phase shifting effect in G_2. The theory graphs fit to the data reasonably well with the data shown in table 4.11.

[7]This assumption is justified if, firstly, the coherence lengths of all three lasers are equal, secondly, all three gratings are equally well aligned and thirdly, if the mirror reflectivity is constant across the mirror surface. We take point one for granted, since the line widths of the lasers are determined by the resonance in the active laser gas and not affected by operating conditions such as gas pressure or temperature [78]. We ensure condition number two to be valid by carefully aligning all three lasers as well as possible. The reflectivity of the mirror is most strongly affected by contaminations of the CaF_2 surface which seems to degrade at equal rates for all three gratings. This observation indicates that condition number three is valid as well.

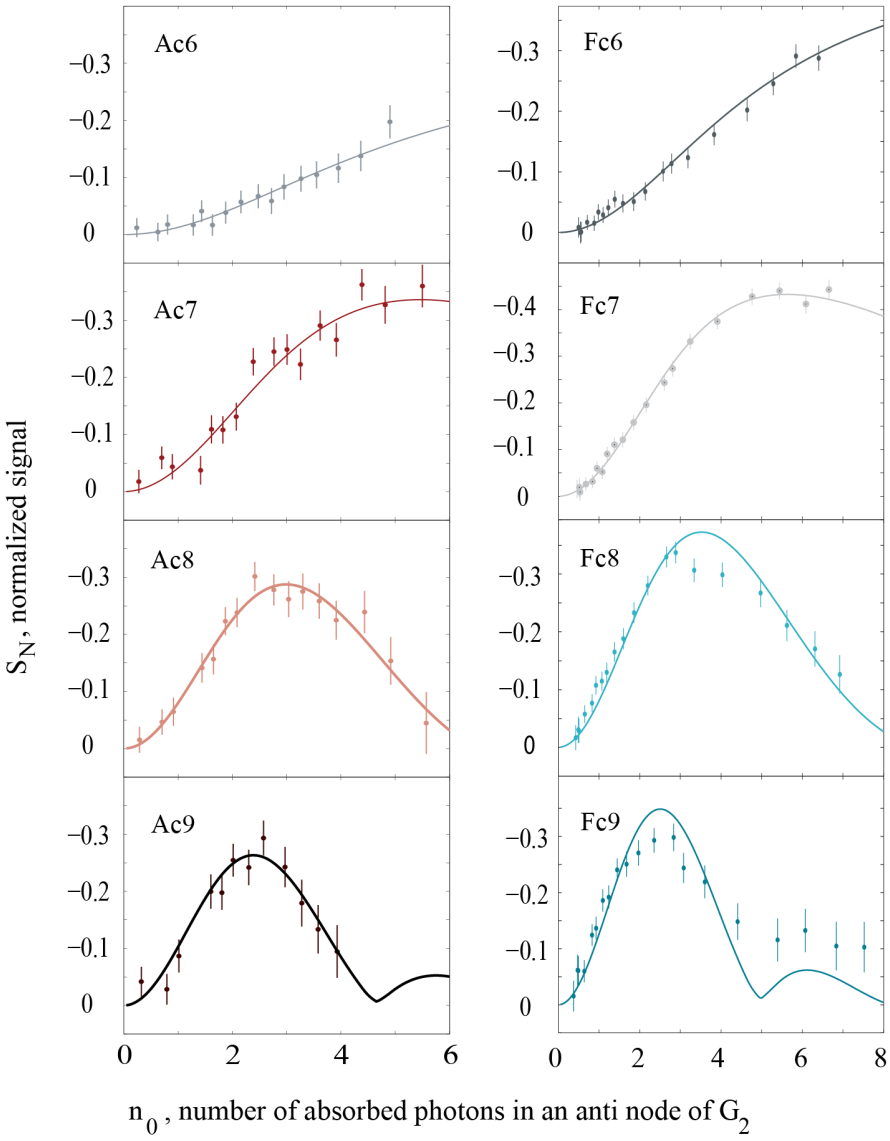

Figure 4.11: The dots show the normalized signal of anthracene (panels on the left) and ferrocene clusters (panels on the right) as a function of n_0 in G_2, which is proportional to the G_2 grating power. ΔT was set to the Talbot time of the 6-fold clusters. The theory graphs (solid lines) show the expected contrast for the parameters in table 4.11.

fitting parameter	anthracene, height 1 mm	anthracene, height 2 mm	ferrocene, height 1 mm
K	0.75 ± 0.02	0.70 ± 0.03	0.80 ± 0.01
Λ	-0.47 ± 0.03	-0.47 ± 0.04	-0.51 ± 0.01
β_7	0.53 ± 0.06	0.42 ± 0.05	0.56 ± 0.03
β_8	0.41 ± 0.03	0.39 ± 0.04	0.51 ± 0.02
β_9	0.40 ± 0.05	0.42 ± 0.05	0.41 ± 0.02

Table 4.1: Output of the fitting routine described in the text.

The reduction of the standing wave visibility with increased mirror distance is consistent with the green graph in figure 3.2. For that simulation, perfect reflectivity and optimal alignment were assumed, which is why the graph starts at unity visibility. In any real experiment, the standing wave visibilities are expected to be smaller than unity even at zero mirror distance due to degradation of the mirror surface and imperfect grating alignment, which is reflected in the K values of table 4.1. For the ferrocene experiment, the K parameter was slightly higher at similar mirror height which indicates that the mirror surface has degraded between the two experimental runs (the ferrocene data are older by several weeks). The grating timing of all three experiments was similar and the mirror curvature unchanged, resulting in $\Lambda \approx -0.5$. The β_i should not depend on the mirror height and indeed they agree within the uncertainty for both anthracene experiments. A comparison of the experimentally obtained optical properties to the literature would be interesting, however, neither absorption cross sections nor dynamical polarizabilities are known for clusters of anthracene or ferrocene.

Our new method is capable of filling this gap. Absolute values for VUV absorption cross sections can straightforwardly be measured by recording the depletion efficiency of the cluster beam in the pulse of a fluorine excimer laser with the accuracy at which the pulse energy and beam profile are known. Since beam shaping optics and calibrated power meters are readily available, this can be done with existing tools. With the absorption cross sections known, one can calculate α_λ from the measured β.

Small, well known molecules can thus be used to calibrate the mirror and grating conditions for high-mass experiments. Once a high-mass test has been successfully concluded a beam of smaller clusters or molecules with known optical properties can be used to determine K and Λ for the current grating-mirror setup. With these values one can compute the theoretical expectations for the high-mass experiment.

4.5 Fragmentationgratings

Over the course of this thesis the name OTIMA has evolved from standing for ***O**ptical **T**ime domain **I**onizing **MA**tter wave interferometer* to ***O**ptical **TI**me domain **MA**tter wave interferometer*. This change was initated by the results presented in this chapter, which are published in [5]
VUV-optical absorptive gratings, such as the ones used in the OTIMA setup, have many properties that make them favorable for matter-wave interferometry with large particles: they do not clog or break, they have nearly perfect periodicity, they have grating periods smaller than what can currently be fabricated by lithographic means, they offer tunability of the opening fraction and they function without velocity dependent grating wall-particle interactions. When the concept of the OTIMA gratings was originally conceived [60] and theoretically worked out [1] their universality was also highlighted since single-photon ionization with photons of 7.9 eV of energy is an efficient process for many particles such as metal clusters [91], organic [92] and anorganic clusters [3] or tailor-made nanoparticles [93, 94]. While especially metal clusters are ideal for pursuing the goal of high-mass matter-wave interferometry (see section5 for details) a spectroscopy or metrology oriented experiment would benefit from the ability to choose from an even greater pool of particles. Many large molecules with biological relevance, for instance, which would be interesting candidates for different kinds of spectroscopy in OTIMA (see section 5.1), have larger ionization thresholds than 7.9 eV. Although absorptive gratings based on multi-photon ionization are theoretically possible, lower contrast and dephasing due to non-depleting single-photon absorptions make them more difficult to handle than gratings based on single-photon effects [95].

This led to the idea to search for other photoabsorption induced processes that eject particles from the beam. Photofragmentation is such a process, if it is triggered by the absorption of a single grating photon and the recoil associated with the fragmentation suffices to deflect the fragments beyond of the acceptance volume of the mass spectrometer. The number of photons involved in the depletion process can be indentified experimentally by measuring the laser power dependence of the effect. Under the assumption of poissonian statistics the single-photon absorption probability reads

$$P_{SPA} = 1 - \mathrm{e}^{-n_0}, \tag{4.11}$$

where n_0 is the mean number of absorbed photons in the beam, proportional to the pulse energy. For small energies $P_{SPA} \to P_{SPA} \propto n_0$. This linear dependence in the low-power regime is a characteristic feature of a single-photon processes. To test the capabilities of fragmentation

gratings, an experiment with clusters of hexafuorobenzene (C_6F_6, HFB) was devised. HFB is an organic molecule with a mass of $m_{hfb} = 186$ amu. It is similar to benzene, with all hydrogen atoms exchanged with fluorine atoms. HFB is liquid at room temperature and efficiently forms van der Waals bound clusters behind the Even Lavie source (see section 3.4.2). The ionization threshold of the monomer lies at 9.97 eV [96] which renders the molecule immune to efficient single-photon ionization (SPI). For the clusters of HFB the ionization threshold is unknown, however it is unlikely to fall by more than 10 % with respect to the molecule, as indicated by measurements on clusters of up to 5 benzene molecules [97]. HFB clusters are thus expected to be energetically excluded from SPI, as well. A first test showed that the beam of HFB clusters could nevertheless be depleted in the OTIMA gratings and transmissions as low as 20 % were easily be reached.

A schematic of the setup used for this experiment is shown in figure 4.12*a*: the clusters are formed in a supersonic expansion of neon and travel parallel to the interferometer mirror surface, which has been retracted to a height of 1 cm away from the particle beam. They are then subjected to the center grating pulse which, at this distance from the mirror surface, has already dephased to a running wave (see green graph in figure 3.2). This is convenient since it means that the, typically unknown, grating visibility does not influence the power dependence of the depletion. The transmission is measured as a function of the laser power, which is varied as described in section3.1. A measure for the laser energy is provided by the signal of a GaP photodiode. An attenuator was placed in front of the photodiode in order to avoid detector saturation and allowing to assume a linear relation between the laser energy and the photo diode voltage. Figure 4.12*b* shows the measured depletions of the 2, 4 and 5-fold cluster. Relation (4.11) fits well to the data, proving that the cluster depletion in the beam is indeed triggered by a single-photon event. The next step of the experiment is depicted in figure 4.12*c*: the cluster intensity is measured while the power of the detection laser, also a fluorine excimer laser, is scanned, with all the grating lasers disabled. The curves show a strongly non-linear power dependence in the low power regime. Since the mass spectrometer is only sensitive to ionized particles, this proves that ionization of the HFB clusters occurs and must require more than one 157 nm photon. This excludes SPI from the possible depletion mechanisms in the grating laser. Unfortunately, it is not easy to identify which depletion mechanism is triggered in the grating, since, ideally, no particle is be detected after absorption of a grating photon. One can, however, estimate the impact that a possible photodissociation event would leave on a cluster in the beam. For this it is assumed that the entire photon energy is absorbed by only one of the molecules in the cluster and that UV photo dissociation always leads to

the emission of a single fragment molecule, which has been shown to be the case for benzene cluster ions [98]. The kinetic energy of the daughter fragment is thus

$$E_{kin} = \frac{h\nu}{3(N+1)-6} - E_{diss}, \tag{4.12}$$

given that all of the $3(N+1)-6$ vibrational modes are excited equally. Here, N is the number of atoms in the fragment molecule to which 1 is added, representing the van der Waals bond to the mother cluster, $h\nu$ is the photon energy and E_{diss} the dissociation energy of the van der Waals bond[8]. For $h\nu = 7.9\,\mathrm{eV}$, $N = 6$ and $E_{diss} = 70\,\mathrm{meV}$ one arrives at an escape velocity of around 730 m/s of the daughter fragment[9]. Conservation of momentum determines the velocity of the mother fragment. If, after evaporation of a monomer, the cluster consists of, for example, 5 HFB molecules, then it will gain about 150 m/s. There is no preferred direction along which the dissociation takes place so the recoil associated with the fragmentation occurs isotropically in space. The solid opening angle of the detector depends on the grating in which the fragmentation was triggered. For the third grating, the opening angle is estimated to be around 100 mrad. Even with a slow escape velocity of 150 m/s, the heavier fragment will not be detected, either because they are deflected outside of the acceptance zone of the mass spectrometer or because they are accelerated in particle beam direction such that they reach the detector too early or late to be ionized by the detection laser. It is thus plausible that single-photon fragmentation is the dominant depletion mechanism in our HFB cluster beam.

As a next step interference was measured using the protocol described in section 4.1. Figure 4.13a shows the normalized signal of the monomer and the first 4 following clusters. The pulse separation time was set to 11.5 μs which means that the first-order contrast is expected to be high around the 4 -fold cluster and the second order contrast around the dimer. While this is clearly the case, the contrast is not expected to be high between these clusters, which it is in the experiment. These results are consistent with the observation of strong photo fragmentation which naturally also takes place in the ionization region of the spectrometer. Here, destruction of large clusters will add fragments to the signal intensities of smaller clusters. This effectively causes the loss of cluster number resolution: the clusters that are detected to have a certain mass may

[8]Note that assuming thermal equilibrium of all vibrational modes is conservative: the van der Waals bound will more likely absorb most of the energy, yet this would result in even larger escape velocities and is thus neglected.

[9]The value for the dissociation energy was taken from [98], where it was measured for the neutral benzene dimer. I assume the value for larger clusters of HFB to be not far off from this.

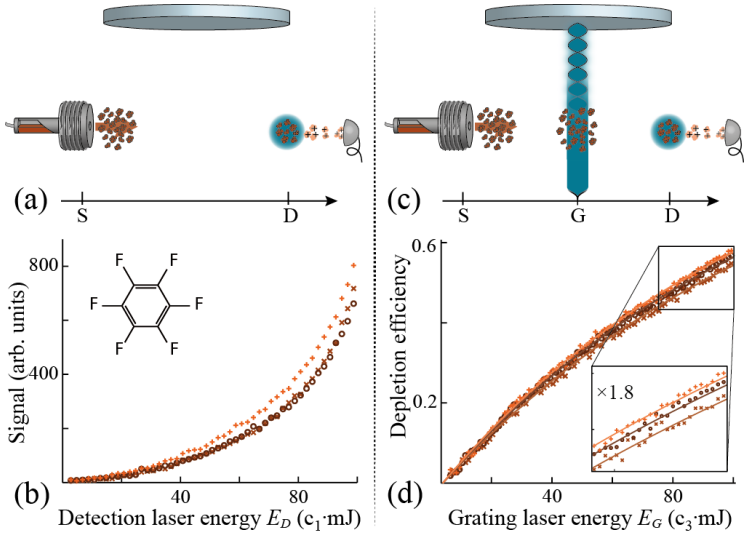

Figure 4.12: *a*) Experimental setup for measuring the HFB (pictured as inset in lower panel) cluster detection efficiency as a function of detection laser power. *b*) Results of this experiment. *c*) Experimental setup for measuring the HFB cluster depletion efficiency as a function of grating laser power. The mirror is retracted from the beam to ensure the particles are subjected to a running wave. *d*) Results of this experiment. The figures are published in [5].

have had a higher mass during their travel through the interferometer. While the amount of normalized signal and its resonant temporal character (see dips in figure 4.13*b* and *c*) point towards the quantum mechanical origin of the contrast, it does not allow to identify the signature mass dependence of Talbot Lau interference. A fully-developed fragmentation grating interferometer would therefore need to be coupled to a softer detection method, for example a resonant two-photon ionization method. Ideas in this direction and plans how to utilize the photofragmentation and dissociation in future experiments are discussed in [99].

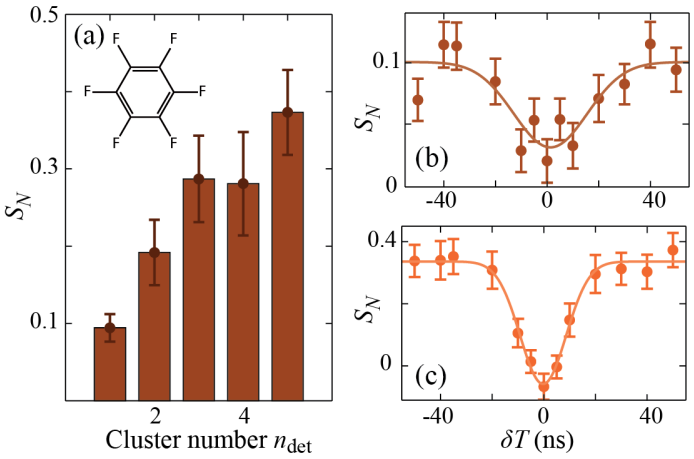

Figure 4.13: *a*) Normalized signal S_N of HFB clusters. *b*) and *c*) S_N of the monomer and the 5-fold cluster, respectively, versus the grating pulse asymmetry δT. Figures taken from [4]

4.6 Interference of tailored nanoparticles

Metal clusters are in many respects ideal particles for OTIMA interferometry: clusters of many metals can be photoionized with high efficiency in the VUV [91], there are sources readily available that put out intense beams of broadly mass distributed particles [100] and, last but not least, their properties approach the bulk values as the number of constituent particles increases [91], making the particle's behavior in the interferometer easier to understand the larger they become. This last feature is particularly crucial for the test of collapse models: it allows to predict the interaction strength of the interfering particles with the gratings and environment and thus promises a thorough understanding of the systematic effects influencing the contrast. Unfortunately, the most common metal cluster source, the Haberland-von Issendorff source [100], which is a highly developed, reliable and well-established tool of cluster physics, emits continous beams of clusters at supersonic velocities. This is not a good match for the pulsed OTIMA interferometer for which supersonic beams are typically too fast for particles heavier than 4 000 amu. An alternative to seed gas-aggregated clusters are synthesised metal nanoparticles (NPs). Many methods have been developed for the synthesis of NPs with diverse properties [101]. While routine methods exists to lift various types of NPs into the gas phase [102, 103] the same cannot be said for the sublimation of neutral NPs which is an ongoing challenge: most pure, synthesised NPs are too fragile or strongly bound to their neighbors to be evaporated in an intact way [60]. However, sublimation of intact and neutral NPs can be facilitated by functionalizing perfluoroalkyl chains to their surface, which act as a stabilizing, 'non-stick' coating. This has been demonstrated, e.g. with C_{60} fullerens [104] or with silicon NPs [105]. It is understood that the favorable volatilization properties of such particles originate from the low polarizability of the attached chains, resulting in weakened van der Waals interactions between neighboring particles [106]. Also, perfluoroalkylation is known to increase the vapor pressure of certain chemical substances [107, 108]. Over the past decade this has been a successful recipe to prepare different types of particles for thermal sublimation in an oven for matter wave experiments [24, 57, 106, 109]. This research was carried out in close collaboration with the group of Professor Marcel Major from the chemistry department at the University of Basel.

The largest particle that was successfully evaporated in an oven so far was a fluorinated porphyrin with a mass around 10 000 amu [24]. However, the long heating times in the oven can fragment a significant amount of particles before they are launched. At the moment it seems that the end of the road is reached for thermal evaporation of such particles in an oven around a particle mass of 10 000 amu, since the thermal instability of

particles typically increases with mass. In order to obtain thermal beams of even heavier particles and to use them in conjunction with the OTIMA interferometer the plan was conceived to ablate tailored NPs from a surface with a pulsed laser. For this purpose, systems consisting of a variable number of fluorinated tetraphenylporphyrins have been chemically decorated with perfluoroalkyl chains to form particles with masses ranging from 2800 amu ($TPPF_{84}$) up to 25 000 amu (fluorinated porphyrin pentamers with around 40 perfluoroalkyl chains) [93,110]. Proof of principle tests have demonstrated the feasibility of ns-laser pulse desorption and VUV photoionization of some of these particles [93, 94]. These promising results have motivated interference experiments with TPP, $TPPF_{84}$ and TPPF(20-x+17x) = $C_{44}H_{10}F_{20-x}N_4(S(CH_2)_2C_8F_{17})_x$, where x is the number of side chains attached. The latter is synthesized as a molecular library. This means that the sample contains particles with a distribution of masses rather than only a single mass, as is the case e.g. for $TPPF_{84}$. For OTIMA interferometry this is very useful since it facilitates the simultaneous investigation of all masses without changing the interferometer settings and allows to use the methods originally developed for cluster interferometry (see section section4.2 for details). TPP, although not carrying fluorinated side chains, is a suitable test particle since it is the basic element of the other two molecules. From an experimental point of view it is also a convenient molecule for calibration of the interferometer since it can be evaporated very efficiently in the same source as its fluorinated cousins. Also, in this source TPP is emitted with a velocity distribution as wide as 400 m/s which allows investigation of several Talbot orders.

Data of four different TPP interference experiments is shown in figure 4.14. The pulse separation times ΔT were set to 57, 64, 93 and 103 μs, which corresponds to the $6th$, $7th$, $10th$ and $11th$ Talbot order. Due to the gravitational deflection, the normalized contrast S_N changes sign as the pulse delays increase. For these experiments, TPP molecules were initially evaporated onto a glas sample. This sample was then mounted inside the OTIMA source chamber. The molecules were desorbed from the surface by 100 μs pulses of a 532 nm laser with pulse energies of 0.5 mJ. For this, the continuous beam of a *Coherent Verdi V18* was chopped with an acousto-optic modulator. The grating intensities were adjusted such that the gratings transmit 20-30 % of the molecules. During all interference experiments in this chapter the contrast was recorded as described in section 4.2.

In order obtain a beam of $TPPF_{84}$ molecules, which are schematically displayed in figure 4.15a, the NP powder was solved in tetrahydrofuran (THF) and applied to a glas plate, where it dried to an around 200 μm thick layer. From this surface the molecules were desorbed with a 5 ns, 3 mJ laser pulse of an *Ekspla NT242a* tunable OPO laser, set to emit

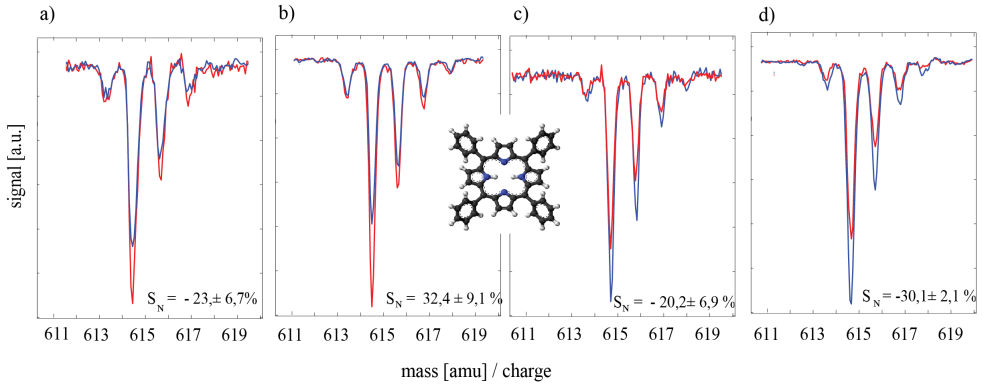

Figure 4.14: Mass spectra of TPP (shown in the center inset) recorded in the resonant mode (red line) and off resonant mode (blue line, asymmetric by 50 ns). The ΔT was set to *a*) 57, *b*) 64, *c*) 93 and *d*) 103 μs (corresponding to the data shown from left to right). Gravitational deflection of the interfering particles causes a sign change of the normalized signal S_N as the pulse delays increases.

at 650 nm and focused to a spot size of around 1 mm^2. The particle beam intensity was highest for a particle velocity of around 350 m/s. As usual, the VUV grating power was set to transmit around 25 % of the particles. The grating pulse delay in the resonant mode was symmetric up to a few nanoseconds and tuned to $\Delta T = 42.32\,\mu$s, which corresponds to the Talbot time of particles with a mass of 2 665 amu. The contrast amounted to around 29.6 ± 0.1 % (see figure 4.15*b*).

The next larger NPs under investigation were the molecular library TPPF(20-x+17x). The mass distribution is peaked at a mass of 5560 amu, as can be seen in the mass spectrum displayed in figure 4.16 which was recorded in the OTIMA machine. The sample plates were prepared similarly to the $TPPF_{84}$-samples. The desorption method was identical, as was the detection protocol. The velocity distribution was peaked around 160 m/s and the pulse delay was set to $\Delta T = 94.11\,\mu$s, which corresponds to the Talbot time of particles with a mass of 5 927 amu. After the interferometer the signal was, unfortunately, too low to resolve S_N for all mass peaks other than the one at 5 560 amu. Interference, amounting to a contrast of -36.3 ± 0.1 % could be observed only for this peak. Although the highest contrast in the OTIMA interferometer is usually achieved with identical delays between G_1/G_2 and G_2/G_3, in this experiment the contrast was highest for an interferometer that was asymmetric by over 40 ns. The standard Talbot Lau theory cannot explain this behavior, which may be due to a systematic error in the measurement of the grating pulse timing.

The next larger particles under investigation were a library of particles with masses centered around 20 000 amu. These particles have shown to

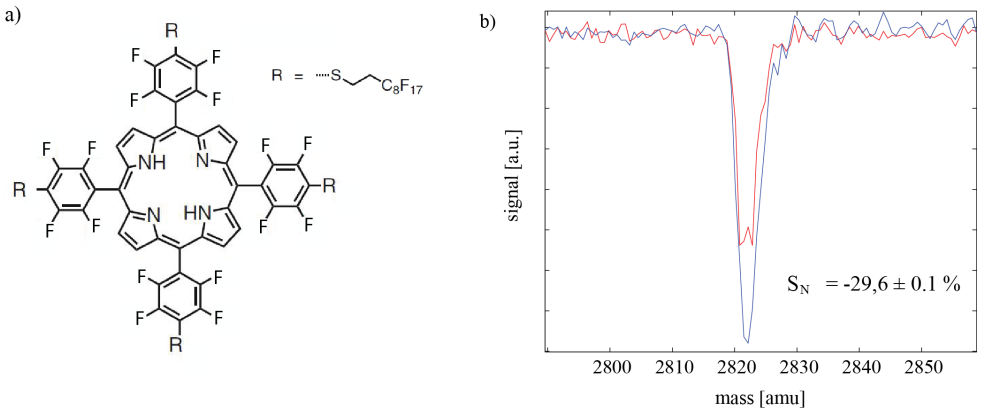

Figure 4.15: a) $TPPF_{84}$: Tetraphenylporphyrin (TPP) dressed in fluorine atoms and perfluoroalkyl chains. Figure adapted from [93]. b) $TPPF_{84}$ mass spectrum recorded in the resonant mode (red graph) and off-resonant mode (blue graph), showing an S_N of nearly -30 %. To reduce detection noise due to background ions, each point in the graph is an average over 5 data points measured over a time of flight interval of 5 ns.

be volatilizable under laser heating and have photoionized during earlier tests [94], inside the OTIMA setup, however, the beam intensity was still too low for interference experiments. This could be explained by the longer beam line in the OTIMA (around 50 cm) as compared to the proof-of-principle experiment, where the particles were desorbed directly inside the ion source of the mass spectrometer and detected after a flight distance of only a few mm. It is also possible that the NP sample has decayed over the year-long time between the two experiments.

The advantages of metal clusters for OTIMA interferometry in conjunction with the drawbacks of common metal cluster sources have motivated experimenting with the pulsed thermal laser evaporation of functionalized metal NPs. For this purpose Dr. Almudena Gallego-Gonzales from the group of Professor Major synhesised several prototypical NP libraries based on perfluoroalylization of a variety of different metallic core materials and also silicon cores. The particles with the most promising properties had a silver nanocrystal core [111] and will be referred to as AGS_2 in the following. They were synthesized by heating silver nitrate and a thiol ligand in ethylene glycol at 160°C for several hours, followed by centrifugation in methanol, THF and diethyl ether. FTIR spectroscopy then confirmed successful formation of NPs and that the ligands were indeed attached to the silver core. MALDI spectra as well as TEM images of the particles deposited from the gas phase on a sample plate provided promising evidence that the particles stay intact during evaporation at masses ranging up to 15 000 amu. These particles

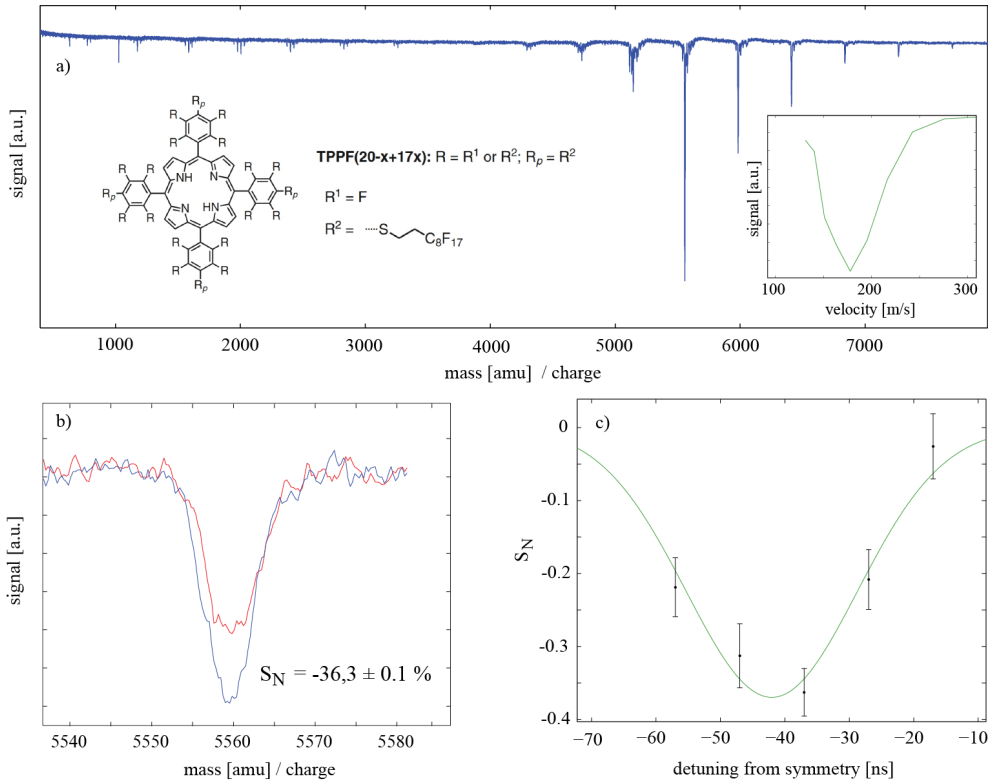

Figure 4.16: *a*) Mass spectrum of the molecular library TPPF(20-x+17x). The left inset shows a schematic of the molecules, taken from [93], the inset in the right shows the velocity distribution of the highest peak in the mass distribution. *b*) Mass spectrum of the highest peak in the TPPF(20-x+17x) library, recorded in the resonant mode (red graph) and off-resonant mode (blue graph), showing S_N = -36,3 %. *c*) S_N as a function of detuning from the symmetric interferometer configuration, revealing a maximum S_N for an interferometer asymmetry of over 40 ns. To guide the eye, a gaussian with FWHM of around 36 ns has been fitted to the data.

were tested in the OTIMA machine. They were sonicated to form an emulsion with THF which later evaporated as the mixture was applied to a glas plate, leaving a thin NP layer behind. This layer was evaporated by a 532 nm laser beam chopped to 100 to 300 μs and pulses with energies between 1 and 6 mJ. In the ionization region of the mass spectrometer, the particles were photoionized with a 2 mJ pulse of 157 nm light. A mass spectrum of the AgS2 library can be seen in figure 4.17. It is an average over 10 000 shots. A peak height discriminator was used to filter out detection noise and to facilitate ion counting (as explained in section3.3). The libraries typically contain a bi-modal mass distribution peaked between 10 000 and 15 000 amu and smaller masses up to 4000 amu. Peaks in the high mass range of the spectrum are spaced by roughly 270 amu. This is unusual since in other perfluoroalylizated libraries, such as TPPF(20-x+17x), the peaks were spaced by the mass of a single side chain weighing 376 amu. Since the chains are intrinsically very stable it is not conceivable that they fragment partially while staying attached to the silver core. Ag_2S, weighing roughly 250 amu could explain the difference in mass between two neighboring peaks, since the mass calibration of the mass spectrometer may be off by 10 or 15 amu. In this case the particles would be compounds of silver and sulfur atoms and not, as intended, perfluoroalylizated silver clusters. Two-fold charging of the particles could also explain why the spacing in the spectrum in figure 4.17 is roughly half of what is expected. It is unlikely, however, that only doubly charged ions are detected, and no ions with a single charge, which would be distributed around 5000 amu in the spectrum in figure 4.17 with a spacing of 484 amu, or larger number. The latter would occur at a spacing that is an integer fraction of 484 amu, depending on the number of charges carried by the ion. Also, multi charging requires the absorption of multiple photons, and the maxima of the envelopes of the differently charged particle distributions would strongly depend on the laser power. This was not observed in the experiment, where the envelope of the mass distribution did not change with laser power, apart from a mass-independent reduction of ion counts.

With the high-quality samples we tried to measure interference of AGS2. The pulse separation time was scanned from 100 to 150 μs corresponding to the Talbot times of a particle masses from 6000 to 9500 amu with mean velocities between 100 and 150 m/s. Grating transmissions ranging from 20 to 40 % were tried. Smaller particles with masses from 600 to 1300 amu, also present in the AGS2 library, showed contrast of up to 20 %, with a grating delay of 84 μs, as shown in figure 4.18, where the mass spectrum is compared to a simulation of the normalized signal. For that, the dimensionless parameter β was set to one, which is a common value for particles in this mass range with ordinary optical properties. The laser energy was set to achieve a cluster transmission of 30 %.

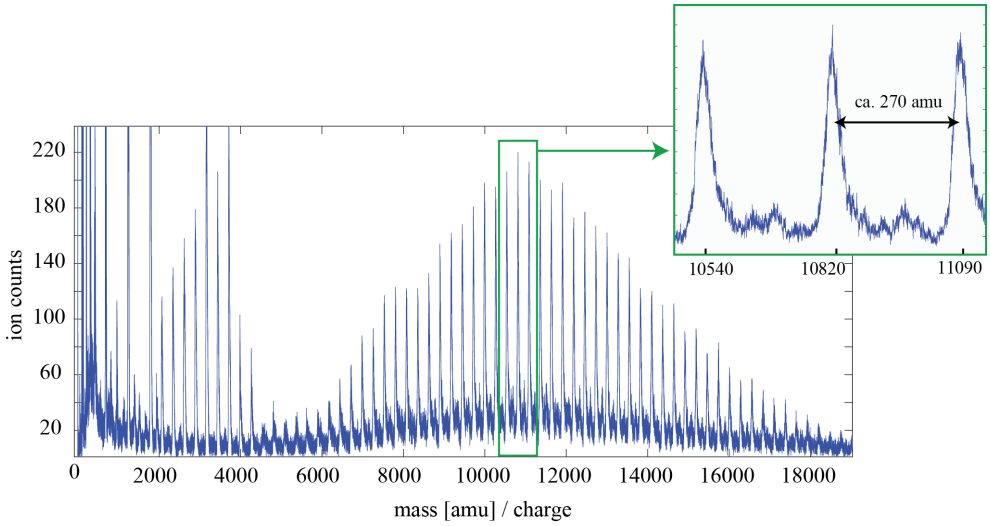

Figure 4.17: Mass spectrum of an AGS2 library, exhibiting the typical bimodal mass distribution. The high mass peaks are separated by roughly 270 amu.

Even though the optical properties of AgS particles are not known from first principle theory the simulation reproduces the mass dependence of the measured interference signal. This, in conjunction with previous calibration measurements with TPP which had produced contrast at a $\Delta T = 103\,\mu$s (see figure 4.14*d*), excludes unfavorable gravitational fringe phase, low grating quality and fringe averaging due to machine vibrations as reasons for the unobservability of large mass AGS2 interference. Also, decoherence due to collisions with background gas particles can be excluded since this is not expected to occur for masses smaller than 10^6 amu at a pressure of 1×10^{-8} mbar, which is the pressure that was measured on the main interferometer chamber [2]. What cannot be excluded is that the pressure is much higher in the particle beam due to smaller particles that are co-evaporated with the NPs of interest. This could lead to collisional decoherence and destruction of the interference pattern. Another reason for the loss of contrast could be related to the temperature of the particles. The long-pulse laser evaporation method produced the highest signal at a beam velocity of 150 m/s. Since the particles are launched from am open surface, it is unlikely that the beam is propelled by a supersonic expansion or a shock wave typically associated with ns-pulse desorption. If we assume a thermal sublimation process, the temperature of a particle with 10 000 amu right after launching amounts around 13,000 K. At such high temperatures the silver core would be liquid and emitting thermal radiation. Even if the particle travels for several milliseconds until it enters the interferometer and cools off significantly during the flight, decoherence due to the thermal emission of IR photons

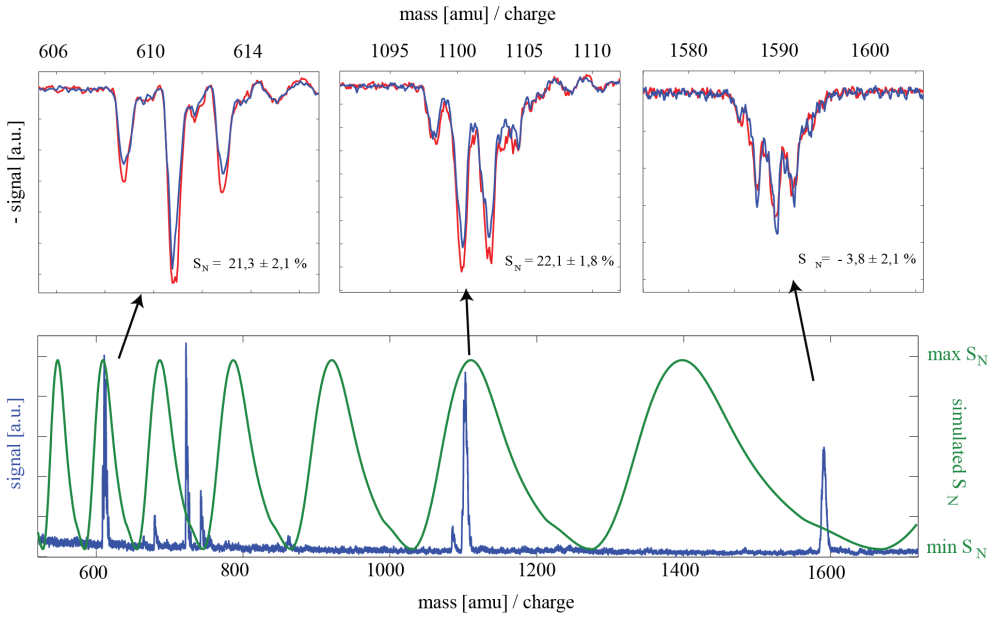

Figure 4.18: Interference of smaller-mass particles from the AGS2 library. Although the optical particle properties are not sufficiently well-known to make a prediction about the absolute amount of contrast, the mass dependence of the contrast is reproduced by a simulation, plotted in green in the lower panel. The lower panel also shows an overview spectrum of the mass range. The three upper panels show the peaks at 610, 1100 and 1590 amu, respectively, recorded with symmetric (red line) and asymmetric grating delays (blue line). As predicted by the simulation, the peak at 1590 amu shows no contrast.

would destroy the contrast. It seems unlikely that the particles would survive such elevated internal temperatures. The more probable scenario is that the particles are initially slower and colder, but are accelerated in a stream of smaller fragments, e.g. single side chains. Still, high levels of internal excitation cannot be excluded. Comparison with figure 2.6 in section2.2 shows that as much as 3000 K can cause decoherence during the flight though the interferometer. For particles that are internally very hot, fragmentation decoherence is also conceivable, caused by the dissociation of a bond between the ligand and the core.

Concluding remarks on OTIMA experiments with synthesized Nanoparticles

Measuring OTIMA Interference of synthesized nanoparticles is an ongoing experimental challenge. Especially the experiments with the AGS2 library have helped to refine the requirements that must be fulfilled by a future nanoparticle source for the OTIMA setup. First and foremost, the source must be as intensive as possible since the use of three absorptive gratings is very lossy. This is illustrated using the example of the AGS2 nanoparticles. The spectrum in figure 4.17 is an average of 10 000 shots. Since the grating lasers are limited to a repetition rate of 100 Hz, it thus took 100 seconds to record this spectrum. Integrating over the highest peak in the high-mass region of the spectrum one finds at least a number of 5000 particles. The source emits on average one particle per mass, every two shots. High contrast is expected if each grating transmits less than 25 % of the signal. That means that around 98.5 % of all particles are lost during the interferometer sequence. To measure the normalized contrast at a fixed grating pulse delay, one needs to measure in both interferometer modes roughly hundred times longer than without the gratings. Obtaining similar statistics as in figure 4.17 thus requires a measurement time of about 5 hours. The interferometer itself has proven to be stable over such a period of time, however, the nanoparticle plate must be changed about every hour. This entails breaking the vacuum and subsequently waiting for sufficiently good pressure in the source chamber. The experiments were additionally complicated by quality fluctuations of the nanoparticle samples. Each synthesis of the AGS2 library produced about 1 g of NP sample which lasts for about 5 hours of OTIMA interference measurements. Unfortunately the synthesis did not always yield consistent results and there were strong variation in sample quality from batch to batch. The quality range can be seen in figure 4.19, where averages over 10 000 shots are plotted. Some of the samples did not produce discrete NP peaks at high masses but rather a continuum of masses (see figure 4.19c). This not usable for interference experiments because one cannot discern the NP signal from a possibly present offset, arising from time-uncorrelated backgound noise in the spectrum. Other samples did not contain any high mass particles at all (see figure 4.19b).

Although it was possible to record data over several weeks of AGS2 measurements which would have allowed, statistically, to resolve a normalized signal of more than 15 % it is clear that, for future experiments, one needs particles that are more abundant and a more consistent source assembly.

Regarding the problem of high internal excitation of the particles, which can lead to thermal decoherence as described in the previous section and section2.2, the source must be optimized for low per pulse en-

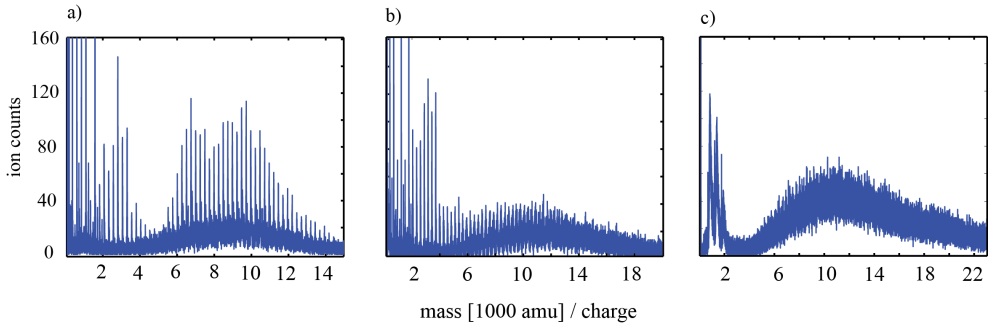

Figure 4.19: Mass spectra of three different synthesis batches of AGS2. Sometimes no signal at high masses could be detected (spectrum b) or no individual peaks were resolved (spectrum c).

ergies of the desorption laser. Unfortunately it is challenging to measure internal particle temperatures and for many particles boundaries on the internal temperature will be provided only by the observation of interference contrast, allowing to imply the absence of emission of thermal radiation. There are, however, buffergas cooling techniques available to internally cool particles in a thermal beam [112]. The feasibility of such a scheme and its compatibility with the pulsed OTIMA setup are currently under investigation. A possible strategy is to combine a cryogenic buffer gas with cavity cooling, a technique which promises an increase of signal due to a collimation of the particle beam [83].

Chapter 5

Outlook

5.1 Towards specroscopy in the OTIMA interferometer

Spectroscopy is one of the key tools of natural sciences and there is an impressive arsenal of methods for gas-phase spectroscopy of molecules [113]. The most straightforward way to investigate the spectral absorption of free molecules is to sublimate them in a gas cell and measure the attenuation of a laser beam passing though. For molecules that survive the transfer into the gas phase, this can provide the absolute absorption spectrum if the density of molecules in the gas is well known. This is typically very difficult to measure precisely [114]. Although there are sophisticated methods to reduce doppler line broadening [115] the molecules investigated in a gas cell will always be rotationally and vibrationally hot. Higher resolution is achieved with molecules supersonically expanded into the vacuum to form a beam of internally cold molecules [116]. Here one can either investigate the wavelength dependence of the efficiency of resonant multi-photon ionization (R2PI or REMPI) channels [117] or infer the absorption properties via the emitted fluorescence spectrum [118]. Another possibility is to either monitor the dissociation of molecules under illumination of spectroscopy light or the the ejection of messenger atoms that have been attached to the molecule of interest [119, 120]. All these techniques have in common that information about the photon absorption is obtained only indirectly, via some action that is triggered by the absorption process, be it emission of photons, electrons or fragments. The information about the absorption is thus always convolved with the efficiency of the relaxation process. For many molecules, the pure absorption characteristics can only be obtained by performing spectroscopy inside of a matter-wave interferometer [121, 122]. Here we can measure the recoil associated with every absorption process, irrespective of its consequences.

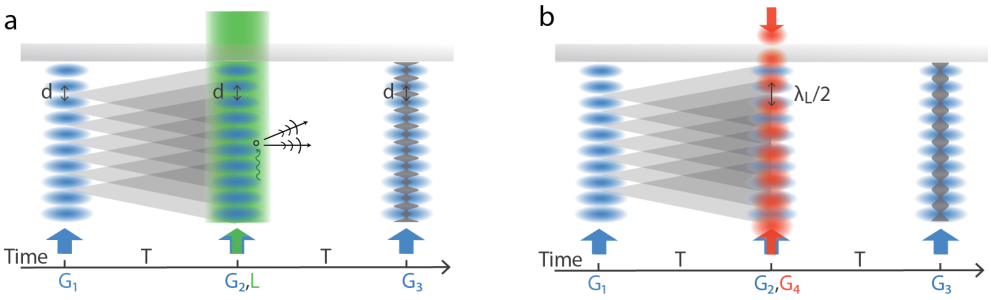

Figure 5.1: *a*) Schematic setup of a recoil spectroscopy experiment based on the three-grating OTIMA interferometer: the spectroscopy laser L overlaps with the center grating. *b*) Schematic setup of an experiment to measure the interaction of interfering particles with a wavelength-tunable standing wave, temporally and spatially overlapping with G_2

Aligning a Talbot Lau interferometer such as the OTIMA is an experimental challenge since already small perturbations acting on the particles during their flight though the interferometer suffice to destroy the fragile interference effect. This means, in turn, that the interferometer can be used as a sensor for measuring the strength of interactions between the particle beam and an external field, if this field leads to a deflection of particles parallel to the grating vectors. It has been demonstrated, for example, that electric susceptibilities of particles can be measured by mounting suitable electrodes to a Talbot Lau interferometer [123, 124]. This technique may be extended to the measurement of magnetic susceptibilities with the use of a Halbach-type magnet [125]. Extending such metrological applications of Talbot Lau interferometry to spectroscopy schemes will be a future goal of OTIMA interferometry. Absolute absorption spectroscopy in a Talbot Lau interferometer has been proposed in [126] and demonstrated recently in the KDTLI setup [121]. This section will review some ideas for spectroscopy experiments that will be carried out in the OTIMA interferometer and have been proposed in [6].

Matter-wave enhanced recoil spectroscopy

Absorption spectroscopy in a pulsed Talbot Lau interferometer works as depicted in figure 5.2*a*: in addition to passing though the three interferometer gratings, the particles are subjected to a spectroscopy laser beam parallel to the grating vector. The mean number of photons absorbed in the spectroscopy laser pulse with energy E_L and wavelength λ_L is

$$n_0 = \frac{2\pi E_L \lambda_L}{\hbar c A} \sigma_L, \tag{5.1}$$

where the intensity is assumed to be flat-top across the beam waist A and σ_L is the particle's absorption cross section at λ_L. The resulting interference pattern in the plane of G_3 will thus be an weighted average over two or more shifted interference patterns and the weights are determined by n_0. According to equation 2.12, the sensitivity for fringe shifts in the three grating configuration is highest at the appearance time of G_2 which is also the ideal time for the spectroscopy laser to be triggered. Assuming that the time between G_2 and G_3 is the k-fold multiple of the Talbot time for the interfering particles the imparted photon recoil amounts to a shift of

$$s = \frac{kd^2}{\lambda_L}, \tag{5.2}$$

where d is the grating period. Contrast of OTIMA interference patterns typically lies around 40% which are thus to good approximation sinusoidal, would suffer a reduction by the factor

$$R = \exp\left(-n_0 \left[1 - \cos\left(\frac{2\pi k d}{\lambda_L}\right)\right]\right) \tag{5.3}$$

The logarithm of the visibility reduction therefore depends linearly on the cross section λ_L [122]. Here it is assumed that there are no additional contrast altering effects associated with the passage though the spectroscopy laser beam, such as emission of thermal radiation after photon absorption, radiative relaxation by fluorescence or modification of the detection probability for the excited particles. Also, the power of the spectroscopy laser must be kept low, such that multi-photon absorptions are rare. This is necessary because multi-photon absorptions hamper the ability to extract absolute values for λ_L from the measurement.

Recoil measurements have been used successfully to determine the absolute absorption cross section of C_{70} fullerenes in a thermal beam at $\lambda_L = 532\,\text{nm}$ in the KDTLI setup [121]. We plan to extend such experiments to OTIMA interferometry, which offers several technical advantages compared to the continuous KDTLI setup. First and foremost, a pulsed interferometer allows the use of pulsed spectroscopy lasers, which are readily availalable in form of OPO systems. Such a laser exists in the OTIMA lab[1], which is continuously wavelength tunable from 200 nm to beyond $2\,\mu$m and sports a high per pulse output energy between 1 and 10 mJ across the wavelength range as well as a repetition rate matching the 100 Hz of the experiment. A table-top continuous laser with comparable optical flux and tunability does not exist. The OTIMA is also

[1] Ekspla NT242a

advantageous for spectroscopy because of the ample optical access to the interferometer region. This allows, for example, to illuminate the particle beam collinearily, which is not possible in a setup with material gratings and is very convenient, as described later in section5.1. On the fundamental side, an OTIMA spectroscopy experiment would benefit from the high contrast that can be achieved with the all-optical setup, since the signal to noise ratio of the σ_L-measurement increases with the contrast. Also, the strength of the velocity selection, which must be large in a continuous setup [122] does not enter the error budged of spectroscopic measurements in a time-domain experiment.

For the absorption spectroscopy to work well with OTIMA interferometry, the recoil imparted by a spectroscopy photon, defined via equation 5.2 must lead to a displacement of the particle of at least several nanometers at the time of G_3. For first-order interference, high sensitivity to the spectroscopy laser is expected in the 270-320 nm range (s = 23-20 nm). This could allow the study of electronic states of aromatic amino acids, nucleotides, peptides and oligonucleotides. The sensitivity can be increased by using slower particles that interfere in higher Talbot orders, i.e. coherently enclose a larger area within the interferometer. This could allow to record spectra in the visible wavelength range as well. A possible way how to extend this scheme to the IR range is discussed in the next section.

Multi-photon recoil spectroscopy

Photons in the near-infrared or far-infrared with wavelengths of $\lambda_L = 3 - 100\,\mu$m would impose shifts between 2 nm and 6 pm. Such small shifts will be very difficult to detect in the OTIMA interferometer. For particles that are sufficiently slow or small, one can resort to high Talbot orders to amplify the recoil effect, however, most particles beams will be too fast. One possibility is to induce multiple absorptions of IR photons. Resonant multiphoton absorptions within the same vibrational level is usually suppressed by the anharmonicity of molecular potentials, a phenomenon referred to as the *anharmonicity bottleneck* (see figure 5.2*a*). In larger and internally more complex molecules, however, electronic excitation is typically followed by relaxation to a different vibrational level, as depicted in figure 5.2*b* [127]. This dissipation of energy occurs on a timescale much shorter than the pulse duration of the spectroscopy laser and can thus enable the absorption of large numbers of IR photons. Since the number of photon absorptions is governed by Poissonian statistics, it is not known how many recoils each interfering particles has received. This can be seen as a random walk of the particles in momentum space. While the method does promise to provide position and widths of the absorption lines with high accuracy, absolute values for σ_L cannot be

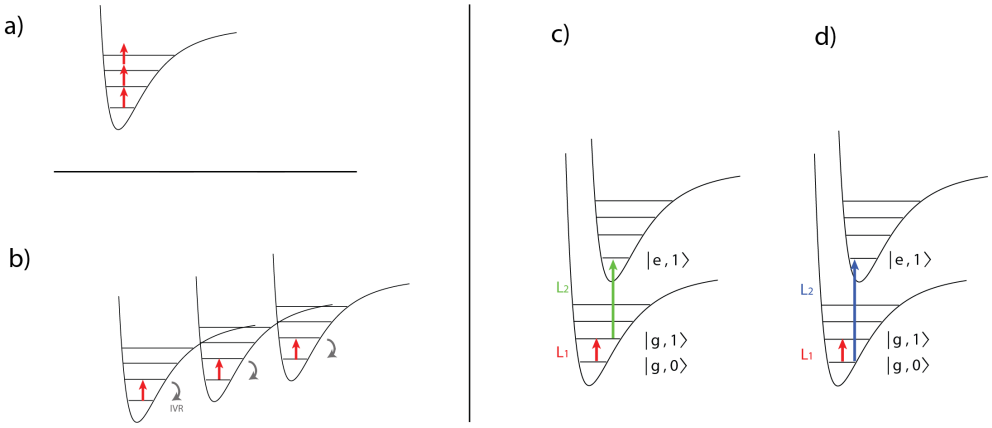

Figure 5.2: a) The *anharmonicity bottleneck* preventing multiple absorptions of IR photons with identical wavelength. b) Fast dissipation of energy by *Intra Vibrational Relaxation* (IVR) is a mechanism that eludes the anharmonicity bottleneck. IVR can facilitate multiple absorption events in molecules with a rich internal structure of vibrational modes and might be used for multi-photon recoil spectroscopy in OTIMA. c) and d) Illuminating the particles in the interferometer with two lasers L_1 and L_2 might allow to correlate the measurable recoil induced by a UV photon with the absorption of a spectroscopy photon in the IR and thus provide resolution of vibrational modes. A similar figure was published in [6]

determined in lack of the exact knowledge of n_0.

For certain fragile molecules the heating associated with the absorption of multiple IR photons will lead to spectroscopic shifts, conformational changes or dissociation and is thus not viable option for recoil spectroscopy. A solution might be to spatially and temporally overlap another laser L_2 with the spectroscopy laser. When the molecules are initially in the electronic and vibrational ground state they may absorb an IR photon of the spectroscopy laser beam which, in turn, triggers the resonant absorption of a L_2 photon. The wavelength of L_2 will be chosen to impart an amount of momentum onto the particle that is measurable in the OTIMA interferometer. This scheme is depicted in figure 5.2*c*. A variant of this method, illustrated in figure 5.2*d*, entails first exciting the ground state molecules with a UV photon from L_2, which will reduce the contrast. Shining in the spectroscopy laser will raise the contrast again, if the energy of the IR photons is sufficient to depopulate the electronic and vibrational ground state of the molecules and if the absorp-

tion of a UV photon is more probable for molecules in the ground state $|g,0\rangle$ than in the IR excited state $|g,1\rangle$. These two multi-photon methods promises to facilitate the investigation of spectroscopic properties of massive molecules with biological relevance that are usually not accessible with conventional spectroscopic techniques. They might also be interesting to determine vibrational spectra of metal clusters, which can give insight into the geometries of these particles [119]. Finally, pulsed two-color schemes like the ones discussed in this section might allow to quantify lifetimes of excited states by measuring absorption-induced contrast reduction as function of the time delay between the spectroscopy laser and L_2.

Fluorescence recoil spectroscopy

So far it was assumed that the spectroscopy laser influences the OTIMA contrast only by kicking a fraction of the particles and blurring the interference pattern. There are, however, molecules which do not store the absorbed photon energy entirely but emit fluorescent light on a nanosecond time scale. This probability is given by the fluorescence quantum yield P_f. Since photon emission is isotropic in space and associated with a recoil, fluorescence leads to decoherence. Each emission can be treated as a single decoherence event and if the fluorescence spectrum is denoted by $F(\omega)$ then the momentum kicks are distributed like

$$\gamma(x) = \int_0^\infty d\omega F(\omega) \mathrm{sinc}\left(\frac{\omega x}{c}\right), \tag{5.4}$$

as derived in [128]. The sinus visibility reduces by a factor of

$$R = n_0 \left(1 - \exp\left(\frac{2\pi i s}{d}\right)\left[P_f\left(1 - \gamma\left(\frac{i\lambda_L}{d}\right)\right) + 1\right]\right) \tag{5.5}$$

under the influence of the absorption recoil and fluorescence decoherence [126]. Here, s is the amount by which the absorption recoil shifts the excited particles to the time of the third grating. In the absence of fluorescence, i.e. for $P_f = 0$, R reduces to equation (5.3). However, for $P_f > 0$, measuring the influence of the spectroscopy laser on the contrast will not provide a value for σ_L because the mean number of absorbed photons enters also as the product $P_f \times n_0$. One possibility is to make a measurement where the spectroscopy laser overlaps collinearly with the particle beam[2]. In this way the recoil of the absorption has no effect on the particle dynamics parallel to the grating vectors and the reduction factor becomes

[2]This is equivalent to aligning the spectroscopy laser parallel to the interferometer mirror, which might, experimentally, be more convenient.

$$R = n_0 P_f [1 - \gamma(\lambda_L)] \tag{5.6}$$

In this mode the loss of contrast depends only on the product of the absorption cross section and the fluorescence quantum yield. By inserting the resulting $P_f n_0$ in (5.5) one can discern the effects of absorption and fluorescence decoherence and potentially obtains absolute values for P_f as well as for σ_L. This requires knowledge of $F(\omega)$ and there are established methods for measuring this close to the source opening of a supersonic expansion source [129].

Polarizability spectroscopy

Measuring dynamic polarizabilities of atoms or molecules is an ongoing experimental challenge [130], and the interest was fueled e.g. by the necessity to reduce light shifts for atomic frequency standards and clocks in the optical domain [131]. Dynamic polarizabilities have been determined via the ac-Stark effect [132], measurements of refractive indexes of gases or, more recently, with an atom interferometer [133]. For molecules the methods are less developed. Molecular dynamic polarizabilities can also, theoretically, be measured via the ac-stark effect [134] [135]. However, the light-molecule interaction will typically lead to a broadening, rather than a shift, of the lines and the interpretation is difficult since there are many reasons for line broadening in molecular spectroscopy. A different approach is the so called light force technique, first demonstrated for atoms [136] and later for C_{60} fullerenes [137]. In these experiments the defocussing of a particle beam at an intense and pulsed standing light wave is measured. It has been proposed to combine this method with OTIMA interferometry [6]. For this one would add a fourth standing wave to the interferometer which is formed by the spectroscopy laser and again overlaps with the second grating, as depicted in figure 5.1b. This spectroscopy grating acts as an array of dipole lenses that mix the phases of the traversing matter waves, hence reducing the interference contrast. Quantitatively, the reduction factor for the sinus visibility reads

$$R = \frac{\left| J_0\left(\sqrt{\phi_L^2 \sin^2\left(\pi \frac{2d}{\lambda_L} k\right) - \frac{n_0^2}{4} \cos^2\left(\pi \frac{2d}{\lambda_L} k\right)}\right)\right|}{J_0(i n_0/2)}, \tag{5.7}$$

where J_0 is the Bessel functions of the first kind and the interferometer timing is set to the k-fold multiple of the Talbot time. The reduction R depends on the number of absorbed photons n_0 as well on the maximal phase shift ϕ_L that the matter waves experience in the spectroscopy grating:

$$\phi_L = \frac{4\pi E_L \alpha(\lambda_L)}{A_L h c \varepsilon_0} \tag{5.8}$$

Here A_L is the beam profile area of the spectroscopy grating and E_L its per pulse energy. Assuming the knowledge of n_0, which can be obtained with the previously discussed techniques, one can measure the optical polarizability of the particles at λ_L.

There are two possibilities for realizing this type of experiment in the OTIMA setup. For a spectroscopy laser with a coherence length of at least several centimeters one could simply place a broadband mirror with the reflecting surface facing downwards on the back of the interferometer mirror. For the OPO available in the OTIMA lab this will not be possible, since its coherence length is far below 1 cm. It is conceivable, however, to position a thin mirror on a translation stage in the gap between the interferometer mirror surface and the particle beam. In this configuration it is not possible to perfectly overlap the spectroscopy grating in time and space with G_2 since then it would block the VUV laser beam, but it can be tolerated to have a gap between the two standing waves of a few mm. The cleanest, yet experimentally most challenging route is to feed the OPO through a Sagnac interferometer, the two arms of which overlap exactly where the particle beam is illuminated by G_2. Due to the short coherence length of the OPO laser, the arms must have the same lengths where they hit the particles. Otherwise the standing wave forms somewhere else and the particles experience just an incoherent superposition of two running waves. The relative arm-length difference could be tuned by passing one beam though a tunable delay stage made out of two mirrors and a reflecting corner cube. Just as for the VUV gratings (see section 4.4) the quality of the standing wave will be an important systematic. Other than with gratings formed at a mirror surface, the power of the two running waves generating the standing wave inside the Sagnac interferometer can be measured individually by measuring the influence of the light on the particle beam with one of the Sagnac arms blocked. It must be stressed that, irrespective of how the spectroscopy grating comes into being, it is not necessary to have its phase locked to the VUV gratings. On the contrary, it is even desirable to have the spectroscopy grating moving in space since this will average out possible shadowing effects or even constructive diffraction that might mask the reduction of contrast under observation [6].

Conventional beam depletion spectroscopy in the OTIMA setup

Especially when set to UV wavelengths, the spectroscopy laser will typically deplete a certain fraction of the particle beam because of photo ionization or photo dissociation. The particles that underwent one of these

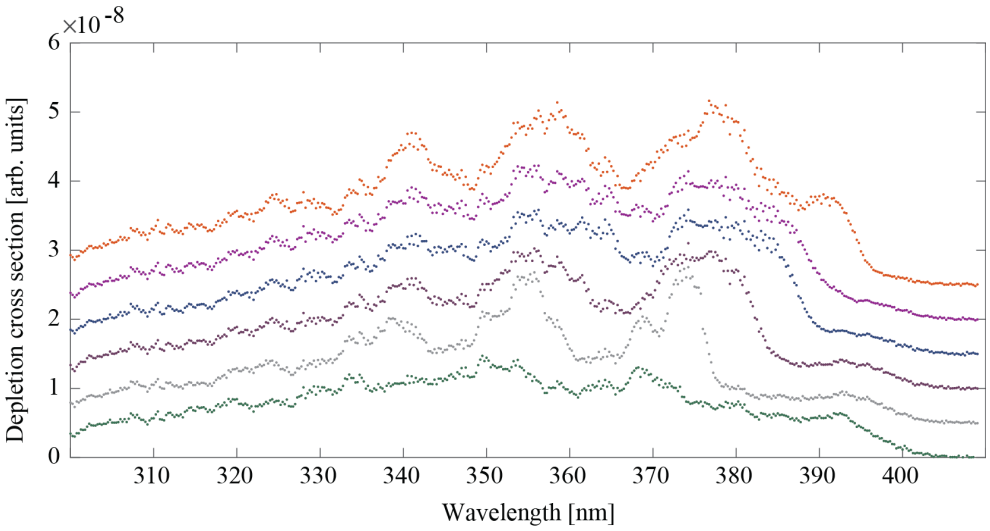

Figure 5.3: Depletion spectra of anthracene custers, from the monomer (bottom, green) to the 6-fold cluster (top, orange). An offset has been added to the graphs to make the differences better visible.

processes are likely to be ejected from the particle beam and deflected to outside the spatio-temporal opening window of the mass spectrometer, either because they are electro statically attracted by the grounded metal parts surrounding the beam and or because of the dissociation recoil. On the one hand, this is unfortunate since it reduces the signal and necessitates longer measurement times. On the other hand the spectral dependence of this depletion contains information about a potential relaxation channel following the photon absorption. Of course, it does not take a matter-wave interferometer to measure such macroscopic particle deflections but in a spectroscopy experiment in the OTIMA setup this information practically comes for free when one compares the signal with the spectroscopy laser on and off. Furthermore, beam depletion caused by the spectroscopy laser is a good measure for its overlap with the particle beam and can thus be used for alignment purposes.

Figure 5.3 shows the wavelength dependent depletion efficiency of anthracene clusters. These were emitted from the Even Lavie valve (see section 3.4.2 for details) in neon seed gas and detected in the time of flight mass spectrometer. The OPO laser was hitting the particles at a distance of 6 cm to the detector. The wavelength of the OPO laser was tuned from 300 to 410 nm in 0.25 nm steps and for each wavelength a cluster spectrum was recorded such that the depletion could be calculated. For each measurement a fraction of the spectroscopy laser light was passed to a biased photo diode[3]. A linear relationship between the photo diode voltage and the laser's intensity was assumed. The depletion was

[3]Thorlabs DET10C

then correlated with the photo diode-voltage, where both the spectral responsivity of the photo diode as well as the spectral reflectance of the mirror directing the laser light onto the particle beam have been taken into account. This eliminated, to good approximation, the intensity variation of the laser as it scans though the wavelength range. Naturally this was only permitted, because the pulse energy of the laser was kept low enough to assume proportionality between the cluster depletion and the laser intensity as well as neglect multi-photon absorptions. The lack of pronounced features for the monomer is consistent with the hypothesis that the absorption of a VUV photon in the ionization region of the mass spectrometer is not followed by the ejection of the photo electron leads to fragmentation of the cluster. The fact that already the dimer shows pronounced features that agree well with anthracene monomer spectra in the literature [138] corroborates the view that fragmentation of the clusters usually leads to a complete destruction of the cluster and only increases the signal intensity of the monomer. This is an important observation since it means that the detected clusters have had the same mass when they were illuminated by the spectroscopy laser and are not fragments of larger clusters. Comparision of the spectra with the literature shows that, compared to gas cell absorbance measurements [138], the spectra are red shifted by at least 10 nm which increases with cluster number.

Concluding remarks on OTIMA-assisted spectroscopy

This section has reviewed different spectroscopic techniques that could be realized within the interferometer setup. Remarkably, many different spectral particle properties could be investigated more or less in the same experimental run: cross sections for single or multi-photon absorptions, particle-light interactions via the dynamic polarizability, fluorescence emission and, finally, depletion of particles from the beam. In other words one could measure the complete dielectric function of particles in the gas phase in addition to investigating relaxation dynamics following the absorption. The only change in the experimental setup that one would need to make in order to enable switching between the different modes, is changing the angle at which the spectroscopy laser beam hits the particle beam. This could be done automatically with a motorized flip-mirror, or by driving a mirror in and out of the right position for retroreflecting the spectroscopy laser and forming the spectroscopy grating.

Acknowledgments

At the end of my third year of physics studies in Kiel, I traveled to Vienna for an ERASMUS semester. I hadn't organized anything except a room at the *Gasometer* dormitory and a meeting with Markus a few days after my arrival. On the day of the meeting, I took a taxi from the Schottentor station to Boltzmanngasse, because Vienna seemed like a dense urban jungle to me and I thought I would never make it on time if I walked. After a short conversation in the second floor office, I got a tour of the basement labs and was introduced to the OTIMA crew: Nadine Dörre, Philipp Haslinger and Philipp Geyer. At the time, the experiment was still under construction and pretty much consisted of empty vacuum chambers on an optical table. Markus told me that they could use another student to help with the setup of the new machine and invited me to join the team. I remember being amazed by this offer, considering that I had never worked in a real lab before.
Markus, I sincerely want to thank you for your trust, support and encouragement, that persisted when one ERASMUS semester turned into another one and finally into several years! In the mean time, we completed the machine and tried to understand what it was doing (and I think we succeeded, in that respect, to a certain degree!). Nadine, Philipp, Philipp and I, and later also Armin Shayeghi and Andrea Grimaldi, spent hours, days and nights in the lab, working on the experiment, talking about science, nonsense, politics, wolfs, pressure cookers, candy, the Waldviertel compared to the rest of the world, Tocotronic's song *Die neue Seltsamkeit* and whether rhinoviruses can pass though the material that surgical face masks are made from. While some of the discussions might have been a bit repetitive, I don't want to have missed a single one. Thanks guys for the friendship and the good times! I also want to thank Stefan Nimmrichter, Benjamin Stickler and Kay Walter, for their theory and MATLAB support. I want to thank Marcel Major, Lukas Felix and Almudena Gallego-Gonzales for synthesizing nanoparticles for us. I want to thank Gordon Murray from *GAM lasers* and Stefan Kaesdorf from *Kaesdorf time of flight mass spectrometers* for their tech support. I want to thank my thesis advisor Jook Walraven for his advice and encouragement. And finally, I have to thank Ferdinand Schmidt-Kaler for motivating me to go to Vienna and contact Markus in 2009: I don't know where I would be today if it wasn't for that suggestion, but I certainly wouldn't have met a certain physicist from Gdansk on my second day in Vienna.
And that thought is unbearable to me!

Publications

J. Rodewald, P. Haslinger, N. Dörre, B. Stickler, A. Shayeghi, K. Hornberger and M. Arndt
New avenues for matter-wave enhanced spectroscopy
Appl. Phys. B (2017) 123:3

N. Dörre, P. Haslinger, J. Rodewald, P. Geyer and M. Arndt
A refined model for Talbot-Lau matter-wave optics with pulsed photo-depletion gratings
JOSA B 32, 0000114 (2015)

P. Haslinger, N. Dörre, P. Geyer, J. Rodewald, S. Nimmrichter and M. Arndt
A universal matter-wave interferometer with optical ionization gratings in the time domain
Nature Physics 9,144–148 (2013)
News & Views,Nature Physics by Cronin & Holmgren

N. Dörre, J. Rodewald, P. Geyer, B. von Issendorff, P. Haslinger, and M. Arndt
Photofragmentation beam splitters for matter-wave interferometry
Phys. Rev. Lett. 113, 233001 (2014)
Editor's Choice, featured as a viewpoint by Gil Summy in **Physics 7, 122 (2014)**

M. Arndt, N. Dörre, S. Eibenberger, P. Haslinger, J. Rodewald, K. Hornberger, S. Nimmrichter, and M. Mayor
Matter-wave interferometry with composite quantum objects
"**Atom Interferometry" Proceedings to the Varenna Summer School 2014**
editors: G. Tino and M. Kasevich

P. Geyer, U. Sezer, J. Rodewald, L. Mairhofer, N. Dörre, P. Haslinger, S. Eibenberger, C. Brand and M. Arndt

Perspectives for Quantum Interference with Biomolecules and Biomolecular Clusters

Phys. Scr. 91, 063007 (2016)

Curriculum Vitae

Education

11/2017	**Visiting Student Researcher** at Stanford University in the group of Prof. Mark Kasevich
11/2011 -	**PhD student** at the University of Vienna, Supervisor Prof. Dr. Markus Arndt, topic of dissertation: *Experiments with a pulsed Talbot Lau matter-wave interferometer*
11/2011 -	**Doctoral studies** of physics at the University of Vienna
10/2011	**Master of science degree** from the University of Vienna, Supervisor Prof. Dr. Markus Arndt, title of thesis: *Setup of an optical time-domain matter wave interferometer for heavy particles*
9/2010 - 10/2011	**Master studies** of physics at the University of Vienna
9/2010	**Bachelor of science degree** from the University of Vienna, Supervisor Prof. Dr. Markus Arndt, title of thesis: *Vibration detector for an all-optical Talbot-Lau molecular Interferometer*
7/2008	**Pre-Diploma** in physics, University of Kiel

9/2006 - 9/2010	Studies of physics at the Christian Albrechts University of Kiel
8/1993 - 6/2006	Visit of schools in Basel (Switzerland) and Lörrach (Germany), Abitur at the Humboldt Gymnasium Ulm (Germany)

Scholarships

3/2012 –	**Doctoral program *Complex Quantum Systems* (CoQuS)**, Austrian Science Fund (FWF)
2/2012	University of Vienna "performance scholarship" for excellent grades in the summer semester of 2011
9/2009 – 6/2010	ERASMUS scholarship for studying physics at the University of Vienna

Languages

German	**native**
English	**native**
French	**basic knowledge, written and spoken**
Polish	**basic knowledge, written and spoken**

Participation at conferences

Talks:

46th Conference of the European Group of Atomic Systems (EGAS), Riga (Latvia) July 2015, Contributed Talk: "A time domain matter-wave interferometer for testing the mass limits of quantum mechanics"

46th Annual Meeting of the APS Division of Atomic, Molecular and Optical Physics (DAMOP), Columbus (USA) June 2015,
Contributed Talk: "A time domain matter-wave interferometer for testing the mass limits of quantum mechanics"

Meeting of the COST action "Fundamental problems of Quantum physics", Erice (Italy) March 2015,
Invited Talk: "Pulsed matter-wave interferometry for testing the mass limits of quantum mechanics"

Annual Meeting of the Faculty of Physics of the University of Vienna, Vienna November 2014, Invited Talk: "Pulsed matter-wave interferometry with large particles"

44th Conference of the European Group of Atomic Systems (EGAS), Gothenburg (Sweden) July 2012, Contributed Talk: "A universal matter wave interferometer in the time-domain"

International Conference of Physics Students (ICPS), Graz (Austria) Aug. 2010 Contributed Talk: "Wave nature of large metal clusters: Experimental setup of an all-optical near field molecular interferometer"

Poster presentations:

International Conference on Atomic Physics (ICAP), Seoul, South Korea, July 2016

Frontiers in Matter Wave Optics, Chania (Greece), Oct. 2014

International Conference on Quantum Optics, Obergurgl (Austria), March 2014

Summerschool: Quantum matter, Granada (Spain), Sept. 2014

Symposium on Size Selected Clusters, Davos (Switzerland), March 2013

FoQus SFB-Meeting, Innsbruck (Austria), Feb. 2011

Erwin Schrödinger Symposium, Erwin Schrödinger Institute for Mathematical Physics, Vienna (Austria), Jan. 2011

Nanophotonics meets Quantum Optics, DPG-School Bad Honnef (Germany), Sept. 2010

Summerschools:

QoQuS summerschool, Vienna, Sept. 2015

Quantum matter, Granada (Spain), Sept. 2014

QoQuS summerschool, Vienna, Sept. 2013

QoQuS summerschool, Vienna, Sept. 2012

QoQuS summerschool, Vienna, Sept. 2011

QoQuS summerschool, Vienna, Sept. 2010

Teaching

3/2014 – 6/2016	Tutor for beginners lab course, University of Vienna
9/2013 – 2/2014	Tutor for *lecture Experimental Physics III: Atom Physics and nuclear physics,* University of Vienna
2/ 2012	Tutor for advanced lab course *Quantenoptik Praktikum*, University of Vienna

Photographs of the OTIMA setup

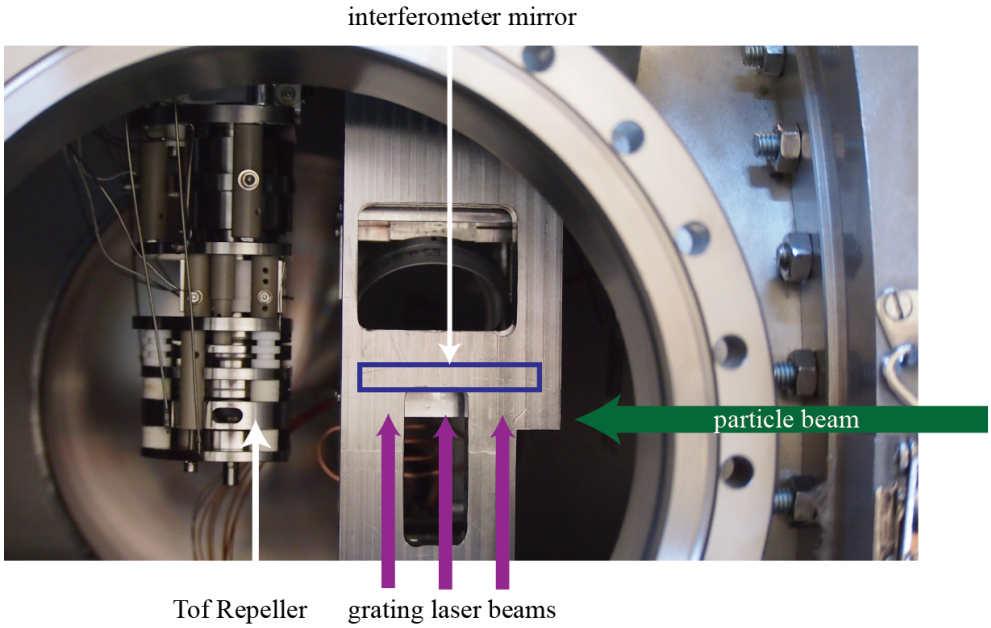

Figure 5.4: View into the main chamber, showing the ion-source region of the mass spectrometer (Tof Repeller) and the mounting assembly of the interferometer mirror.

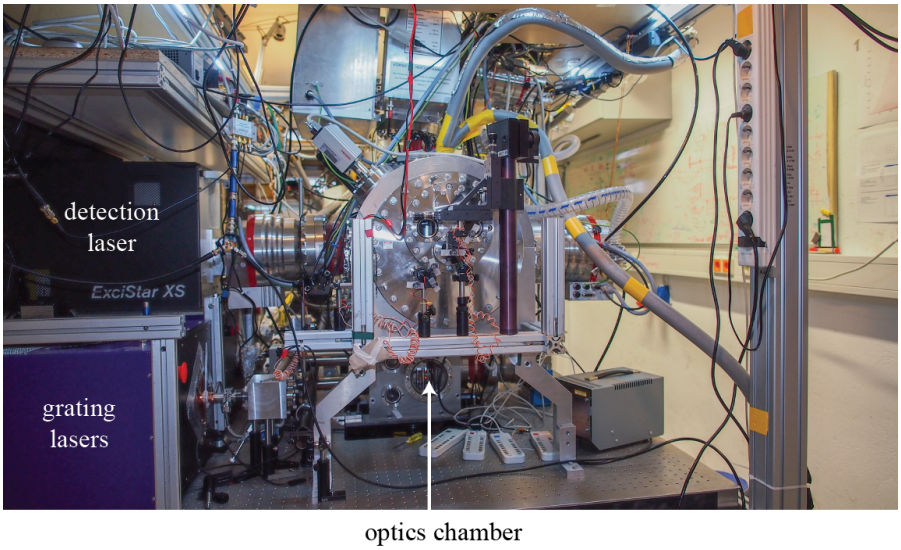

Figure 5.5: Front view of the interferometer setup.

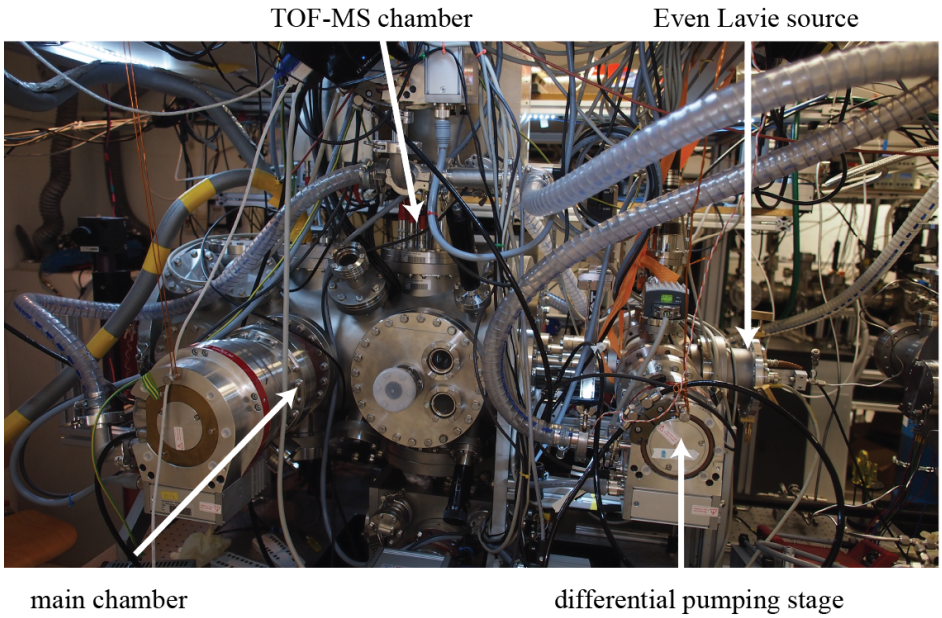

Figure 5.6: A picture of the OTIMA setup with the Even Lavie source attached.

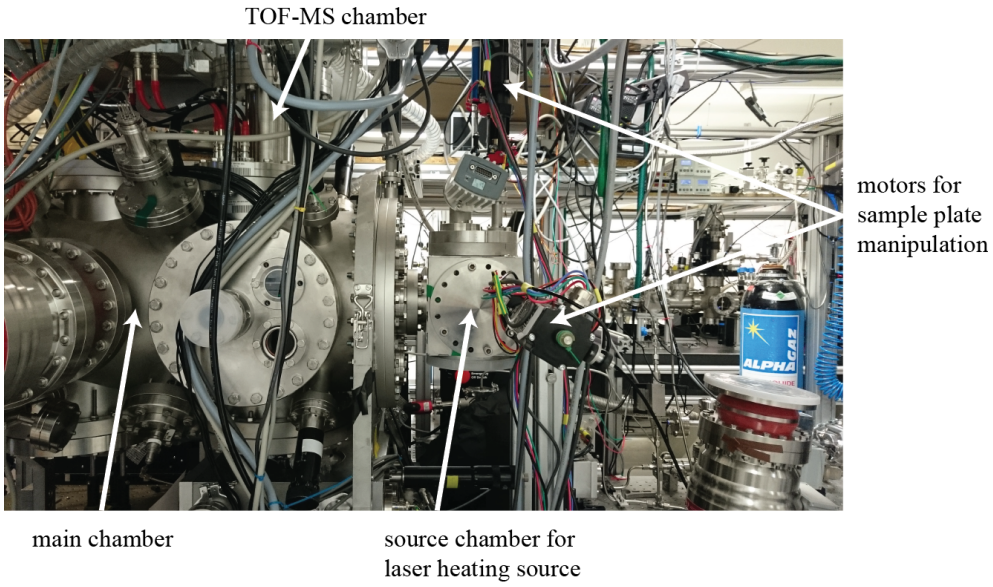

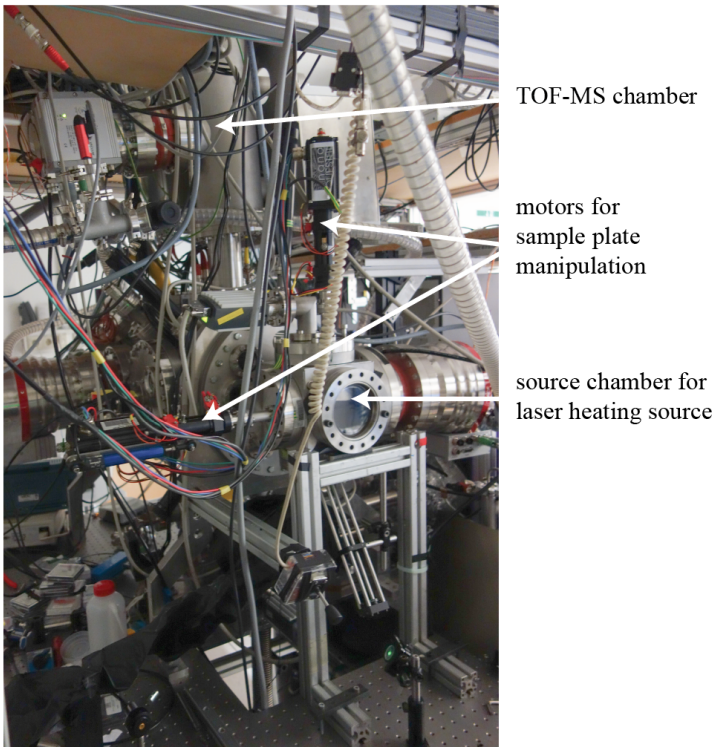

Figure 5.7: The OTIMA setup with the laser heating source attached.

Bibliography

[1] S. Nimmrichter, P. Haslinger, K. Hornberger, and M. Arndt, "Concept of an ionizing time-domain matter-wave interferometer," *New Journal of Physics*, vol. 13, no. 7, p. 75002, 2011.

[2] S. Nimmrichter, K. Hornberger, P. Haslinger, and M. Arndt, "Testing spontaneous localization theories with matter-wave interferometry," *Physical Review A*, vol. 83, p. 43621, apr 2011.

[3] P. Haslinger, N. Dörre, P. Geyer, J. Rodewald, S. Nimmrichter, and M. Arndt, "A universal matter-wave interferometer with optical ionization gratings in the time domain," *Nature Physics*, vol. 9, pp. 144–148, feb 2013.

[4] N. Dörre, J. Rodewald, P. Geyer, B. von Issendorff, P. Haslinger, and M. Arndt, "Photofragmentation Beam Splitters for Matter-Wave Interferometry," *Physical Review Letters*, vol. 113, p. 233001, dec 2014.

[5] N. Dörre, P. Haslinger, J. Rodewald, P. Geyer, and M. Arndt, "Refined model for Talbot-Lau matter-wave optics with pulsed photodepletion gratings," *Journal of the Optical Society of America B*, vol. 32, p. 114, dec 2015.

[6] J. Rodewald, P. Haslinger, N. Dörre, B. A. Stickler, A. Shayeghi, K. Hornberger, and M. Arndt, "New avenues for matter-wave-enhanced spectroscopy," *Applied Physics B*, vol. 123, p. 3, jan 2017.

[7] M. Planck, "On an Improvement of Wien's Equation for the Spectrum," *Verh. Deut. Phys. Ges.*, vol. 2, pp. 202–204, 1900.

[8] A. Einstein, "Über einen die Erzeugung und Verwandlung des Lichtes betreffenden heuristischen Gesichtspunkt," *Annalen der Physik*, vol. 322, no. 6, pp. 132–148, 1905.

[9] L. de Broglie, "Waves of Matter," *Nature*, vol. 112, no. 2815, p. 540, 1923.

[10] E. Schrödinger, "Quantisierung als Eigenwertproblem," *Annalen der Physik*, vol. 385, no. 13, pp. 437–490, 1926.

[11] M. Born and A. Einstein, "Albert Einstein, Max Born. Briefwechsel 1916 - 1955," *München (Nymphenburger)*, p. 210, 1955.

[12] E. Schrödinger, "Die gegenwärtige Situation in der Quantenmechanik," *Naturwissenschaften*, vol. 6, no. 49, pp. 823–828, 1935.

[13] B. P. Abbott, "Observation of Gravitational Waves from a Binary Black Hole Merger,"

[14] E. Joos and H. D. Zeh, "The emergence of classical properties through interaction with the environment," *Zeitschrift für Physik B Condensed Matter*, vol. 59, pp. 223–243, jun 1985.

[15] I. Pikovski, M. Zych, F. Costa, and Č. Brukner, "Universal decoherence due to gravitational time dilation," *Nature Physics*, vol. 11, pp. 668–672, jun 2015.

[16] L. Hackermüller, K. Hornberger, B. Brezger, A. Zeilinger, and M. Arndt, "Decoherence of matter waves by thermal emission of radiation.," *Nature*, vol. 427, no. 6976, pp. 711–714, 2004.

[17] E. Joos, "Elements of Environmental Decoherence," in *Decoherence: Theoretical, Experimental, and Conceptual Problems*, pp. 1–17, Berlin, Heidelberg: Springer Berlin Heidelberg, 2000.

[18] H. Everett, ""Relative State" Formulation of Quantum Mechanics," *Reviews of Modern Physics*, vol. 29, pp. 454–462, jul 1957.

[19] G. Ghirardi, A. Rimini, and T. Weber, "Unified dynamics for microscopic and macroscopic systems.," *Physical review D*, vol. 34, no. 2, pp. 470–491, 1986.

[20] G. C. Ghirardi, P. Pearle, and A. Rimini, "Markov processes in Hilbert space and continuous spontaneous localization of systems of identical particles," *Physical Review A*, vol. 42, no. 1, pp. 78–89, 1990.

[21] L. Diósi, "Models for universal reduction of macroscopic quantum fluctuations," *Physical Review A*, vol. 40, pp. 1165–1174, aug 1989.

[22] R. Penrose, "On Gravity's role in Quantum State Reduction," *General Relativity and Gravitation*, vol. 28, pp. 581–600, may 1996.

[23] W. Marshall, C. Simon, R. Penrose, and D. Bouwmeester, "Towards Quantum Superpositions of a Mirror," *Physical Review Letters*, vol. 91, p. 130401, sep 2003.

[24] S. Eibenberger, S. Gerlich, M. Arndt, M. Mayor, and J. Tüxen, "Matter-wave interference of particles selected from a molecular library with masses exceeding 10,000 amu.," *Physical chemistry chemical physics : PCCP*, vol. 15, pp. 14696–700, sep 2013.

[25] A. Vinante, M. Bahrami, A. Bassi, O. Usenko, G. Wijts, and T. Oosterkamp, "Upper Bounds on Spontaneous Wave-Function Collapse Models Using Millikelvin-Cooled Nanocantilevers," *Physical Review Letters*, vol. 116, p. 090402, mar 2016.

[26] M. Bilardello, S. Donadi, A. Vinante, and A. Bassi, "Bounds on collapse models from cold-atom experiments," may 2016.

[27] C. Curceanu, B. C. Hiesmayr, and K. Piscicchia, "X-rays Help to Unfuzzy the Concept of Measurement," *Journal of Advanced Physics*, vol. 4, pp. 263–266, sep 2015.

[28] M. Carlesso, A. Bassi, P. Falferi, and A. Vinante, "Experimental bounds on collapse models from gravitational wave detectors," *Physical Review D*, vol. 94, p. 124036, dec 2016.

[29] M. Bahrami, M. Paternostro, A. Bassi, and H. Ulbricht, "Proposal for a Noninterferometric Test of Collapse Models in Optomechanical Systems," *Physical Review Letters*, vol. 112, p. 210404, may 2014.

[30] S. Nimmrichter, K. Hornberger, and K. Hammerer, "Optomechanical Sensing of Spontaneous Wave-Function Collapse," *Physical Review Letters*, vol. 113, p. 020405, jul 2014.

[31] L. Diósi, "Testing Spontaneous Wave-Function Collapse Models on Classical Mechanical Oscillators," *Physical Review Letters*, vol. 114, p. 050403, feb 2015.

[32] G. P. Thomson and A. Reid, "Diffraction of Cathode Rays by a Thin Film," *Nature*, vol. 119, pp. 890–890, jun 1927.

[33] C. Davisson and L. H. Germer, "The scattering of electrons by a single crystal of nickel," *Nature*, vol. 119, pp. 558–560, 1927.

[34] I. Estermann and O. Stern, "Beugung von Molekularstrahlen," *Zeitschrift für Physik*, vol. 61, no. 1-2, pp. 95–125, 1930.

[35] H. v. J. Halban and P. Preiswerk, "Preuve experimentale de la diffraction des neutrons," *C.R. Acad. Sci.*, vol. 203, pp. 73–75, 1936.

[36] D. P. Mitchell and P. N. Powers, "Bragg Reflection of Slow Neutrons," *Physical Review*, vol. 50, pp. 486–487, sep 1936.

[37] H. Rauch, W. Treimer, and U. Bonse, "Test of a single crystal neutron interferometer," *Physics Letters A*, vol. 47, no. 5, pp. 369–371, 1974.

[38] C. Bordé, "Atomic interferometry with internal state labelling," *Physics Letters A*, vol. 140, no. 1, pp. 10–12, 1989.

[39] F. Riehle, T. Kisters, A. Witte, J. Helmcke, and C. J. Bordé, "Optical Ramsey spectroscopy in a rotating frame: Sagnac effect in a matter-wave interferometer," *Physical Review Letters*, vol. 67, pp. 177–180, jul 1991.

[40] P. L. Gould, G. A. Ruff, and D. E. Pritchard, "Diffraction of atoms by light: The near-resonant Kapitza-Dirac effect," *Physical Review Letters*, vol. 56, pp. 827–830, feb 1986.

[41] D. W. Keith, M. L. Schattenburg, H. I. Smith, and D. E. Pritchard, "Diffraction of atoms by a transmission grating," *Physical review letters*, vol. 61, no. 14, pp. 1580–1583, 1988.

[42] D. W. Keith, C. R. Ekstrom, Q. A. Turchette, and D. E. Pritchard, "An interferometer for atoms," *Physical Review Letters*, vol. 66, no. 21, pp. 2693–2697, 1991.

[43] M. Kasevich and S. Chu, "Atomic interferometry using stimulated Raman transitions," *Physical Review Letters*, vol. 67, no. 2, pp. 181–184, 1991.

[44] E. M. Rasel and M. K. Oberthaler, "Atom wave interferometry with diffraction gratings of light," *Physical review letters*, vol. 75, no. 14, pp. 2633–2637, 1995.

[45] J. F. Clauser and S. Li, "Talbot-vonLau atom interferometry with cold slow potassium," *Physical Review A*, vol. 49, no. 4, pp. 2213–2217, 1994.

[46] S. Cahn, A. Kumarakrishnan, U. Shim, T. Sleator, P. Berman, and B. Dubetsky, "Time-Domain de Broglie Wave Interferometry," *Physical Review Letters*, vol. 79, pp. 784–787, aug 1997.

[47] A. Peters, K. Y. Chung, and S. Chu, "Measurement of gravitational acceleration by dropping atoms," *Nature*, pp. 849–852, 1999.

[48] D. Schlippert, J. Hartwig, H. Albers, L. Richardson, C. Schubert, A. Roura, W. Schleich, W. Ertmer, and E. Rasel, "Quantum Test of the Universality of Free Fall," *Physical Review Letters*, vol. 112, p. 203002, may 2014.

[49] P. Hamilton, M. Jaffe, P. Haslinger, Q. Simmons, H. Müller, and J. Khoury, "Atom-interferometry constraints on dark energy," *Science*, vol. 349, no. 6250, 2015.

[50] "http://www.dlr.de/dlr/desktopdefault.aspx/tabid-10081/151_read-20337/#/gallery/25194," 2017.

[51] G. Tino, L. Cacciapuoti, K. Bongs, C. Bordé, P. Bouyer, H. Dittus, W. Ertmer, A. Görlitz, M. Inguscio, A. Landragin, P. Lemonde, C. Lammerzahl, A. Peters, E. Rasel, J. Reichel, C. Salomon, S. Schiller, W. Schleich, K. Sengstock, U. Sterr, and M. Wilkens, "Atom interferometers and optical atomic clocks: New quantum sensors for fundamental physics experiments in space," *Nuclear Physics B - Proceedings Supplements*, vol. 166, pp. 159–165, 2007.

[52] G. M. Tino and M. A. Kasevich, eds., *Atom Interferometry, Volume 188 of Proceedings of the International School of Physics "Enrico Fermi"*. IOS Press, 2014.

[53] S. Nimmrichter and K. Hornberger, "Macroscopicity of Mechanical Quantum Superposition States," *Physical Review Letters*, vol. 110, p. 160403, apr 2013.

[54] M. Arndt, O. Nairz, J. Vos-Andreae, C. Keller, G. van der Zouw, and A. Zeilinger, "Wave-particle duality of C60 molecules.," *Nature*, vol. 401, no. 6754, pp. 680–682, 1999.

[55] C. Brand, M. Sclafani, C. Knobloch, Y. Lilach, T. Juffmann, J. Kotakoski, C. Mangler, A. Winter, A. Turchanin, J. Meyer, O. Cheshnovsky, and M. Arndt, "An atomically thin matter-wave beamsplitter," *Nature Nanotechnology*, vol. 10, pp. 845–848, aug 2015.

[56] B. Brezger, L. Hackermüller, S. Uttenthaler, J. Petschinka, M. Arndt, and A. Zeilinger, "Matter-Wave Interferometer for Large Molecules," *Physical Review Letters*, vol. 88, no. 10, p. 100404, 2002.

[57] S. Gerlich, L. Hackermüller, K. Hornberger, A. Stibor, H. Ulbricht, M. Gring, F. Goldfarb, T. Savas, M. Müri, M. Mayor, and M. Arndt, "A Kapitza-Dirac-Talbot-Lau interferometer for highly polarizable molecules," *Nature Physics*, vol. 3, pp. 711–715, aug 2007.

[58] C. Knobloch, B. A. Stickler, C. Brand, M. Sclafani, Y. Lilach, T. Juffmann, O. Cheshnovsky, K. Hornberger, and M. Arndt, "On the role of the electric dipole moment in the diffraction of biomolecules at nanomechanical gratings," *Fortschritte der Physik*, oct 2016.

[59] R. Brühl, P. Fouquet, R. E. Grisenti, J. P. Toennies, G. C. Hegerfeldt, T. Köhler, M. Stoll, and C. Walter, "The van der Waals potential between metastable atoms and solid surfaces: Novel diffraction experiments vs theory," *Europhysics Letters*, vol. 59, pp. 357–363, aug 2002.

[60] E. Reiger, L. Hackermüller, M. Berninger, and M. Arndt, "Exploration of gold nanoparticle beams for matter wave interferometry," *Optics Communications*, vol. 264, pp. 326–332, aug 2006.

[61] H. F. Talbot, "LXXVI. Facts relating to optical science. No. IV," *Philosophical Magazine Series 3*, vol. 9, no. 56, pp. 401–407, 1836.

[62] L. Rayleigh, "On copying diffraction-gratings, and on some phenomena connected therewith," *Philosophical Magazine Series 5*, vol. 11, pp. 196–205, mar 1881.

[63] F. Pfeiffer, T. Weitkamp, O. Bunk, and C. David, "Phase retrieval and differential phase-contrast imaging with low-brilliance X-ray sources," *Nature Physics*, vol. 2, pp. 258–261, apr 2006.

[64] J. Wen, Y. Zhang, and M. Xiao, "The Talbot effect: recent advances in classical optics, nonlinear optics, and quantum optics," *Advances in Optics and Photonics*, vol. 5, p. 83, mar 2013.

[65] E. Lau, "Beugungserscheinungen an Doppelrastern," *Annalen der Physik*, vol. 437, no. 7-8, pp. 417–423, 1948.

[66] K. Hornberger, S. Gerlich, P. Haslinger, S. Nimmrichter, and M. Arndt, "Colloquium: Quantum interference of clusters and molecules," *Reviews of Modern Physics*, vol. 84, no. 1, pp. 157–173, 2012.

[67] S. Nimmrichter, *Macroscopic Matter Wave Interferometry*. Springer Theses, Cham: Springer International Publishing, 2014.

[68] M. Arndt and K. Hornberger, "Testing the limits of quantum mechanical superpositions," *Nature Physics*, vol. 10, pp. 271–277, apr 2014.

[69] M. P. Valdivia, D. Stutman, and M. Finkenthal, "Talbot-Lau based Moiré deflectometry with non-coherent sources as potential High Energy Density plasma diagnostic," *Journal of Applied Physics*, vol. 114, p. 163302, oct 2013.

[70] A. Stibor, K. Hornberger, L. Hackermüller, A. Zeilinger, and M. Arndt, "Talbot-Lau interferometry with fullerenes: Sensitivity to inertial forces and vibrational dephasing," *Laser physics*, vol. 15, no. 1, pp. 10–17, 2005.

[71] L. B. Scaffardi and J. O. Tocho, "Size dependence of refractive index of gold nanoparticles," *Nanotechnology*, vol. 17, pp. 1309–1315, mar 2006.

[72] K. Hornberger, S. Uttenthaler, B. Brezger, L. Hackermüller, M. Arndt, and A. Zeilinger, "Collisional Decoherence Observed in Matter Wave Interferometry," *Physical Review Letters*, vol. 90, p. 160401, apr 2003.

[73] A. Bassi, K. Lochan, S. Satin, T. P. Singh, and H. Ulbricht, "Models of wave-function collapse, underlying theories, and experimental tests," *Reviews of Modern Physics*, vol. 85, pp. 471–527, apr 2013.

[74] B. Arora, M. S. Safronova, and C. W. Clark, "Tune-out wavelengths of alkali-metal atoms and their applications," *Physical Review A*, vol. 84, p. 043401, oct 2011.

[75] M. K. Oberthaler, S. Bernet, E. M. Rasel, J. Schmiedmayer, and A. Zeilinger, "Inertial sensing with classical atomic beams," *Physical Review A*, vol. 54, pp. 3165–3176, oct 1996.

[76] H. Haberland, M. Mall, M. Moseler, Y. Qiang, and T, "Filling of micron-sized contact holes with copper by energetic cluster impact," *Journal of Vacuum*, vol. 94112, no. 5, pp. 2925–2930, 1994.

[77] U. Even, J. Jortner, D. Noy, N. Lavie, and C. Cossart-Magos, "Cooling of large molecules below 1 K and He clusters formation," *The Journal of Chemical Physics*, vol. 112, no. 18, p. 8068, 2000.

[78] C. J. Sansonetti, J. Reader, and K. Vogler, "Precision measurement of wavelengths emitted by a molecular fluorine laser at 157 nm.," *Applied optics*, vol. 40, pp. 1974–1978, apr 2001.

[79] H. Pummer, H. Hohla, M. Diegelmann, and J. Reilly, "Discharge pumped F2 laser at 1580A," *Optics Communications*, vol. 28, no. 1, 1979.

[80] K. Boller, R.-P. Haelbich, H. Hogrefe, W. Jark, and C. Kunz, "Investigation of carbon contamination of mirror surfaces exposed to synchrotron radiation," *Nuclear Instruments and Methods in Physics Research*, vol. 208, pp. 273–279, apr 1983.

[81] R. W. C. Hansen, M. Bissen, D. Wallace, J. Wolske, and T. Miller, "Ultraviolet/ozone cleaning of carbon-contaminated optics," *Applied Optics*, vol. 32, p. 4114, aug 1993.

[82] W. C. Wiley and I. H. McLaren, "Time-of-Flight Mass Spectrometer with Improved Resolution," *Review of Scientific Instruments*, vol. 26, pp. 1150–1157, dec 1955.

[83] P. Asenbaum, S. Kuhn, S. Nimmrichter, U. Sezer, and M. Arndt, "Cavity cooling of free silicon nanoparticles in high vacuum.," *Nature communications*, vol. 4, p. 2743, 2013.

[84] P. Schmid, *Particle sources for molecular matter-wave interferometry with nanoparticles*. PhD thesis, University of Vienna, 2014.

[85] T. Juffmann, A. Milic, M. Müllneritsch, P. Asenbaum, A. Tsukernik, J. Tüxen, M. Mayor, O. Cheshnovsky, and M. Arndt, "Real-time single-molecule imaging of quantum interference.," *Nature nanotechnology*, vol. 7, no. 5, pp. 297–300, 2012.

[86] F. T. Marchese and H. H. Jaffé, "The calculation of ground and excited state molecular polarizabilities: A simple perturbation treatment," *Theoretica Chimica Acta*, vol. 45, no. 4, pp. 241–247, 1977.

[87] G. Malloci, G. Mulas, and C. Joblin, "Electronic absorption spectra of PAHs up to vacuum UV Towards a detailed model of interstellar PAH photophysics," *Astronomy and Astrophysics*, vol. 426, pp. 105–117, 2004.

[88] V. G. Zakrzewski, O. Dolgounitcheva, and J. V. Ortiz, "Ionization energies of anthracene, phenanthrene, and naphthacene," *The Journal of Chemical Physics*, vol. 105, pp. 8748–8753, nov 1996.

[89] J. W. Hager and S. C. Wallace, "Two-Laser Photoionization Supersonic Jet Mass Spectrometry of Aromatic Molecules," *Anal. Chem*, vol. 60, pp. 5–10, 1988.

[90] P. Haslinger, *A universal matter-wave interferometer with optical gratings*. PhD thesis, University of Vienna, 2013.

[91] W. de Heer, "The physics of simple metal clusters: Experimental aspects and simple models, Rev," *Reviews of Modern Physics*, vol. 65, no. 3, pp. 611–676, 1993.

[92] M. Marksteiner, P. Haslinger, M. Sclafani, H. Ulbricht, and M. Arndt, "UV and VUV ionization of organic molecules, clusters, and complexes.," *Journal of Physical Chemistry A*, vol. 113, pp. 9952–9957, sep 2009.

[93] P. Schmid, F. Stöhr, M. Arndt, J. Tüxen, and M. Mayor, "Single-Photon Ionization of Organic Molecules Beyond 10 kDa.," *Journal of the American Society for Mass Spectrometry*, vol. 24, no. 4, pp. 602–608, 2013.

[94] U. Sezer, P. Schmid, L. Felix, M. Mayor, and M. Arndt, "Stability of high-mass molecular libraries: the role of the oligoporphyrin core," *Journal of Mass Spectrometry*, vol. 50, pp. 235–239, jan 2015.

[95] K. Walter, *Coherence and Decoherence in High-mass Matter-wave Interferometry*. PhD thesis, Universität Duisburg-Essen, 2016.

[96] R. Bralsford, P. V. Harris, and W. C. Price, "The Effect of Fluorine on the Electronic Spectra and Ionization Potentials of Molecules," *Proceedings of the Royal Society A: Mathematical, Physical and Engineering Sciences*, vol. 258, pp. 459–469, nov 1960.

[97] H. Krause, B. Ernstberger, and H. Neusser, "Binding energies of small benzene clusters," *Chemical Physics Letters*, vol. 184, pp. 411–417, oct 1991.

[98] A. Kiermeier, B. Ernstberger, H. J. Neusser, and E. W. Schlag, "Multiphoton mass spectrometry of clusters: dissociation kinetics of the benzene cluster ions," *The Journal of Physical Chemistry*, vol. 92, pp. 3785–3789, jun 1988.

[99] P. Geyer, U. Sezer, J. Rodewald, L. Mairhofer, N. Dörre, P. Haslinger, S. Eibenberger, C. Brand, and M. Arndt, "Perspectives for quantum interference with biomolecules and biomolecular clusters," *Physica Scripta*, vol. 91, p. 063007, jun 2016.

[100] H. Haberland, M. Karrais, and M. Mall, "A new type of cluster and cluster ion source," *Zeitschrift für Physik D Atoms, Molecules and Clusters*, vol. 20, pp. 413–415, 1991.

[101] S. Iravani, H. Korbekandi, S. V. Mirmohammadi, and B. Zolfaghari, "Synthesis of silver nanoparticles: chemical, physical and biological methods.," *Research in pharmaceutical sciences*, vol. 9, no. 6, pp. 385–406, 2014.

[102] A. Dass, A. Stevenson, G. R. Dubay, J. B. Tracy, and R. W. Murray, "Nanoparticle MALDI-TOF Mass Spectrometry without Fragmentation: Au25(SCH2 CH2 Ph)18 and Mixed Monolayer Au25 (SCH2 CH2 Ph)18-x (L) x,"

[103] J. B. Tracy, M. C. Crowe, J. F. Parker, O. Hampe, C. Fields-Zinna, A. Dass, and R. W. Murray, "Electrospray Ionization Mass Spectrometry of Uniform and Mixed Monolayer Nanoparticles: Au25[S(CH2)2Ph]18 and Au25[S(CH2)2Ph]18-x(SR)x," *Journal of the American Chemical Society*, vol. 129, no. 51, 2008.

[104] P. J. Fagan, P. J. Krusic, C. N. McEwen, J. Lazar, D. H. Parker, N. Herron, and E. Wasserman, "Production of Perfluoroalkylated Nanospheres from Buckminsterfullerene," *Science*, vol. 262, no. 5132, 1993.

[105] Y. Chao, L. Šiller, S. Krishnamurthy, P. R. Coxon, U. Bangert, M. Gass, L. Kjeldgaard, S. N. Patole, L. H. Lie, N. O'Farrell, T. A. Alsop, A. Houlton, and B. R. Horrocks, "Evaporation and deposition of alkyl-capped silicon nanocrystals in ultrahigh vacuum," *Nature Nanotechnology*, vol. 2, pp. 486–489, aug 2007.

[106] J. Tüxen, S. Eibenberger, S. Gerlich, M. Arndt, and M. Mayor, "Highly Fluorous Porphyrins as Model Compounds for Molecule Interferometry," *European Journal of Organic Chemistry*, vol. 2011, no. 25, pp. 4823–4833, 2011.

[107] N. L. Stock, D. A. Ellis, L. Deleebeeck, D. C. G. Muir, and S. A. Mabury, "Vapor pressures of the fluorinated telomer alcohols–limitations of estimation methods.," *Environmental science & technology*, vol. 38, pp. 1693–9, mar 2004.

[108] P. J. Krusic, A. A. Marchione, F. Davidson, M. A. Kaiser, C.-P. C. Kao, R. E. Richardson, M. Botelho, R. L. Waterland, and R. C. Buck, "Vapor Pressure and Intramolecular Hydrogen Bonding in Fluorotelomer Alcohols," *The Journal of Physical Chemistry A*, vol. 109, pp. 6232–6241, jul 2005.

[109] S. Gerlich, S. Eibenberger, M. Tomandl, S. Nimmrichter, K. Hornberger, P. J. Fagan, J. Tüxen, M. Mayor, and M. Arndt, "Quantum interference of large organic molecules.," *Nature communications*, vol. 2, p. 263, 2011.

[110] L. Felix, U. Sezer, M. Arndt, and M. Mayor, "Synthesis of Highly Fluoroalkyl-Functionalized Oligoporphyrin Systems," *European Journal of Organic Chemistry*, vol. 2014, pp. 6884–6895, nov 2014.

[111] A. Gallego-Gonzales, U. Sezer, M. Arndt, and M. Mayor, "Thermal beams of tailored neutral silver nanocrystals with atomic mass assignment beyond 20 kDa," *To be published*, 2017.

[112] D. Egorov, T. Lahaye, W. Schöllkopf, B. Friedrich, and J. M. Doyle, "Buffer-gas cooling of atomic and molecular beams," *Physical Review A*, vol. 66, p. 043401, oct 2002.

[113] W. Demtröder, *Laserspektroskopie 1 Grundlagen*. Springer-Verlag Berlin Heidelberg, 2011.

[114] P. F. Coheur, M. Carleer, and R. Colin, "The absorption cross sections of and in the visible - UV region," *Journal of Physics B: Atomic, Molecular and Optical Physics*, vol. 29, pp. 4987–4995, nov 1996.

[115] E. Riedle, R. Moder, and H. Neusser, "Pulsed Doppler-free two-photon spectroscopy of polyatomic molecules," *Optics Communications*, vol. 43, pp. 388–394, nov 1982.

[116] R. E. Smalley, L. Wharton, D. H. Levy, C. Fig, O. Spectroscopy, and W. Supersonic, "Molecular optical spectroscopy with supersonic beams and jets," *Accounts of Chemical Research*, vol. 10, no. 4, pp. 139–145, 1977.

[117] L. Zandee and R. B. Bernstein, "Resonance-enhanced multiphoton ionization and fragmentation of molecular beams: NO, I2, benzene, and butadiene," *The Journal of Chemical Physics*, vol. 71, no. 3, p. 1359, 1979.

[118] D. H. Levy, "Laser Spectroscopy of Cold Gas-Phase Molecules," *Annual Review of Physical Chemistry*, vol. 31, pp. 197–225, oct 1980.

[119] P. Gruene, D. M. Rayner, B. Redlich, A. F. G. van der Meer, J. T. Lyon, G. Meijer, and A. Fielicke, "Structures of neutral Au7, Au19, and Au20 clusters in the gas phase.," *Science*, vol. 321, pp. 674–676, aug 2008.

[120] A. Shayeghi, R. L. Johnston, D. M. Rayner, R. Schäfer, and A. Fielicke, "The Nature of Bonding between Argon and Mixed Gold-Silver Trimers," *Angewandte Chemie International Edition*, vol. 54, pp. 10675–10680, sep 2015.

[121] S. Eibenberger, X. Cheng, J. Cotter, and M. Arndt, "Absolute Absorption Cross Sections from Photon Recoil in a Matter-Wave Interferometer," *Physical Review Letters*, vol. 112, p. 250402, jun 2014.

[122] S. Nimmrichter and K. Hornberger, "Theory of near-field matter-wave interference beyond the eikonal approximation," *Physical Review A*, vol. 78, p. 23612, aug 2008.

[123] A. Stefanov, M. Berninger, and M. Arndt, "A novel design for electric field deflectometry on extended molecular beams," *Measurement Science and Technology*, vol. 19, p. 055801, may 2008.

[124] M. Berninger, A. Stefanov, S. Deachapunya, and M. Arndt, "Polarizability measurements of a molecule via a near-field matter-wave interferometer," *Physical Review A*, vol. 76, no. 1, p. 13607, 2007.

[125] L. Mairhofer, *Deflectometry in a Kapitza-Dirac-Talbot-Lau interferometer for matter waves*. Master thesis, University of Vienna, 2013.

[126] S. Nimmrichter, K. Hornberger, H. Ulbricht, and M. Arndt, "Absolute absorption spectroscopy based on molecule interferometry," *Physical Review A*, vol. 78, no. 6, p. 63607, 2008.

[127] A. M. Rijs and J. Oomens, eds., *Gas-Phase IR Spectroscopy and Structure of Biological Molecules*, vol. 364 of *Topics in Current Chemistry*. Cham: Springer International Publishing, 2015.

[128] K. Hornberger, J. Sipe, and M. Arndt, "Theory of decoherence in a matter wave Talbot-Lau interferometer," *Physical Review A*, vol. 70, p. 53608, nov 2004.

[129] R. E. Smalley, D. H. Levy, and L. Wharton, "The fluorescence excitation spectrum of the HeI2 van der Waals complex," *The Journal of Chemical Physics*, vol. 64, no. 8, p. 3266, 1976.

[130] J. Mitroy, M. S. Safronova, and C. W. Clark, "Theory and applications of atomic and ionic polarizabilities," *Journal of Physics B: Atomic, Molecular and Optical Physics*, vol. 43, no. 20, p. 202001, 2010.

[131] A. D. Ludlow, M. M. Boyd, J. Ye, E. Peik, and P. O. Schmidt, "Optical atomic clocks," 2015.

[132] J. A. Sherman, T. W. Koerber, A. Markhotok, W. Nagourney, and E. N. Fortson, "Precision Measurement of Light Shifts in a Single Trapped Ba + Ion," *Physical Review Letters*, vol. 94, p. 243001, jun 2005.

[133] W. F. Holmgren, R. Trubko, I. Hromada, and A. D. Cronin, "Measurement of a Wavelength of Light for Which the Energy Shift for an Atom Vanishes," *Cs*.

[134] C. E. Otis and P. M. Johnson, "The ac stark effect in molecular multiphoton ionization spectroscopy," *Chemical Physics Letters*, vol. 83, no. 1, 1981.

[135] B. Girard, G. O. Sitz, R. N. Zare, N. Billy, and J. VigueÌĄ, "Polarization dependence of the ac Stark effect in multiphoton transitions of diatomic molecules," *The Journal of Chemical Physics*, vol. 97, no. 1, p. 26, 1992.

[136] M. A. Kadar-Kallen and K. D. Bonin, "Light-force technique for measuring polarizabilities," *Physical Review Letters*, vol. 68, pp. 2015–2018, mar 1992.

[137] A. Ballard, K. Bonin, and J. Louderback, "Absolute measurement of the optical polarizability of C60," *The Journal of Chemical Physics*, vol. 113, no. 14, p. 5732, 2000.

[138] A. Thöny and M. J. Rossi, "Gas-phase UV spectroscopy of anthracene, xanthone, pyrene, 1-bromopyrene and 1,2,4-trichlorobenzene at elevated temperatures," *Journal of Photochemistry and Photobiology A: Chemistry*, vol. 104, no. 1, pp. 25–33, 1997.